NANOSTRUCTURE CHARACTERIZATION, FABRICATION AND DEVICES OF 2D MoS_2 AND MoS_2/WS_2 HETROSTRUCTURES

by

SOURAV GARG

PATRICK KUNG, COMMITTEE CHAIR
SEONGSIN MARGARET KIM, CO-CHAIR
ARUNUVA GUPTA
SHANLIN PAN
SERGEY MIROV

A DISSERTATION

Submitted in partial fulfillment of the requirements
for the degree of Doctor of Philosophy
in the Department of Electrical and Computer Engineering
in the Graduate School of
The University of Alabama

TUSCALOOSA, ALABAMA

2021

Copyright Sourav Garg 2021
ALL RIGHTS RESERVED

ABSTRACT

Sparked by the 2D graphene, advanced 2D transition metal dichalcogenides have captured enough attention due to their extraordinary properties and are promising enough for future high speed flexible electronic and optoelectronic devices. Among all the transition metal dichalcogenides, molybdenum disulphide (MoS_2) and tungsten disulphide (WS_2) are explored most extensively since the last few years because of their complementary nature to metallic graphene. These thin 2D materials are semiconducting in nature, and moreover, bandgap also changes from indirect to direct as these materials are thinned down from bulk to monolayer form.

In this study, a stabilized and large area growth of MoS_2 monolayers has been established on oxide and semiconducting substrates such as (0001) sapphire, (100) p-type SiO2/Si, GaN and Ga_2O_3 using low pressure chemical vapor deposition. The quality and crystalline nature of grown MoS_2 is deeply investigated optically by micro-photoluminescence and micro-Raman spectroscopy. Topography and morphology are characterized by scanning electron and atomic force microscopy. The applications of as grown MoS_2 monolayers have been studied by the fabrication of large area photodetector. Also, the gas sensing ability of MoS_2 has been explored by using CO_2 gas, and the minimum detection limit found is 200ppm.

In-addition one step growth of ternary alloys $Mo_{1-x}W_xS_2$ has been achieved by LPCVD. Different compositions of W in MoS_2 have been investigated by micro-photoluminescence and micro-Raman spectroscopy. In-plane heterojunctions of atomic-thick (2D) semiconductors (MoS_2/WS_2) are novel structures that can potentially pave the way for efficient ultrathin and flexible optoelectronics, such as light sources and photovoltaics. Such heterostructures are very

rare and not much is known about their characteristics. They can only be achieved through a synthetic growth process such as chemical vapor deposition (CVD). This is unlike vertical heterostructures, for which the materials can be mechanically stacked one layer on top of the other.

Here, we report a one-step CVD growth of monolayer thick MoS_2/WS_2 in-plane heterostructures. We have characterized their morphological and optical properties using micro-Raman and photoluminescence spectroscopy. Kelvin probe force microscope was used to extract the contact potential difference profile across the MoS_2/WS_2 heterojunction boundary. The junction region of these heterostructures are observed to be a ternary alloy $Mo_{1-x}W_xS_2$. Moreover, through the tip enhanced Raman spectroscopy (TERS), the minimum junction width is extracted out to be pixel limited 25nm. Also, some novel Raman modes are detected through TERS in MoS_2, and WS_2 monolayers, which were not elaborated before.

DEDICATION

This dissertation is strongly dedicated to my beloved parents, elder brother and sister-in-law whose friendship and support made this work possible.

LIST OF ABBREVIATIONS AND SYMBOLS

2D	Two-dimensional
AFM	Atomic force microscope
a, b, c	Lattice parameter
CO_2	Carbon dioxide
CPD	Contact potential difference
d	Lattice spacing
D*	Specific detectivity
e	Electron charge
E	Energy
f	Frequency
FWHM	Full width half maxima
GaN	Gallium Nitride
Ga2O3	Gallium oxide
IR	Infrared
LHS	Lateral heterostructures
LPCVD	Low pressure chemical vapor deposition
MoS_2	Molybdenum disulphide
OM	Optical microscope
PL	Photoluminescence
PMMA	Polymethyl methacrylate

PSD	Power spectral density
R_p	Photo-responsivity
SEM	Scanning Electron Microscopy
SKPFM	Scanning kelvin prove force microscopy
SiO_2	Silicon dioxide
T	Temperature
TERS	Tip enhanced Raman spectroscopy
TMD	Transition metal dichalcogenides
VHS	Vertical heterostructures
WS_2	Tungsten disulphide
XPS	X-ray photoelectron spectroscopy
ω	Angular frequency
∇	Gradient operator

ACKNOWLEDGEMENTS

At the very outset, I praise and thank Almighty God for endowing me with the strength to accomplish this work. I would like to show my special regard and sense of gratitude to my advisor Dr. Patrick Kung and co-advisor Dr. Seongsin Margaret Kim, for providing me with excellent guidance and unbelievable support during the execution of my work. Their outstanding knowledge, constant encouragement, and the unconditional freedom prevailed in the lab not only inspired me but also remained as a driving force behind the study.

I would also like to take this opportunity to show my sincere regard and thanks to my Ph.D. committee members Dr. Arunuva Gupta, Dr. Shanlin Pan from the University of Alabama and Dr. Sergey Mirov from the University of Alabama Birmingham for their invaluable time, support, and comments on my research.

I wholeheartedly thank Dr. Joseph Waters, Dr. Soner Balci and Dr. Mohammad Hokmabadi for their guidance and support during the project work without which it would be difficult to carry out this work successfully.

I also express my sincere thanks to my lab-mates Elizabath Philip and Mohammad Zeki Güngördü, for their help and high degree of cooperation. I thank the CAF staff (Rich Martens, Johnny Goodwin, Sanghamitra Deb and Rob Holler) for their constant help to access the CAF facilities throughout my project.

I also would like to convey my thanks to Andrey Krayev from Horiba Scientific, Audrey Sulkanen and Dr. Gang-Yu Liu from the Department of Chemistry, University of California

Davis for the contribution in the valuable TERS analysis. In addition, I also thanks to Sandra Cortijo-Campos and Dr. Alicia de Andres at Instituto de Ciencia de Materiales de Madrid (CSIC) for their contribution in the vertical heterostructures imaging.

Words will not suffice to express my sincere thanks to all of my friends who were always there to help me.

Last but not least, I express my best regards and thanks to my parents and brother who have always sacrificed their own wishes and happiness to uplift my career.

CONTENTS

ABSTRACT ii

DEDICATION iv

LIST OF ABBREVIATIONS AND SYMBOLS v

ACKNOWLEDGEMENTS vii

LIST OF TABLES xiv

LIST OF FIGURES xv

CHAPTER 1. INTRODUCTION 1

1.1 Background 1

CHAPTER 2. CHARACTERIZATION TECHNIQUES 8

2.1 Scanning Electron Microscope 8

2.2 Micro - Raman Spectroscopy 10

2.3 Atomic Force Microscope 11

2.4 X-Ray Photoelectron Spectroscopy 13

2.5 Scanning Kelvin Probe Force Microscope 15

2.6 Tip Enhanced Raman Spectroscopy 18

CHAPTER 3. MOS_2 MONOLAYERS GROWTH ON SAPPHIRE 19

3.1 Experimental 19

3.2 Results and Discussion of as Grown MoS_2 Flakes 21

3.2.1 Scanning Electron Microscopy 21

3.2.2 Micro-Raman and Optical Characterization 21

3.2.3 Uniformity Check of MoS_2 monolayer triangle 23

3.2.4 The Excitation Power Dependence of PL Spectra 24

3.2.5 XPS Study of as Grown Pristine MoS_2 monolayers on Sapphire Substrates 25

3.2.6 Thickness Study of MoS_2 Flakes by Atomic Force Microscope 26

3.2.7 Temperature Dependent PL of Monolayer MoS_2 on Sapphire Substrate 27

3.2.8 Valley Selective Polarized PL of Monolayer MoS_2 28

CHAPTER 4. SPECIFIC AREA GROWTH OF MOS_2 MONOLAYERS 30

4.1 Circular Template Formation by Microfabrication Followed by the CVD Growth of Monolayers 30

4.1.1 Substrate Patterning by Microfabrication Techniques 30

4.1.2 Synthesis of MoS_2 monolayers on Specific Areas 31

4.2 Results and Discussion 32

4.2.1 SEM Characterization of MoS_2 monolayers Grown at Specific Areas 32

4.2.2 Structural and Luminescence Study of Grown MoS_2 Monolayers 33

CHAPTER 5. MOS_2 MONOLAYERS GROWN ON SIO_2/SI SUBSTRATES 35

5.1 Experiment 35

5.2 Results and Discussion 35

5.2.1 Morphological Characterization of MoS_2 by Scanning Electron and Optical Microscope 35

5.2.2 Micro-Raman and micro-PL Characterization 36

5.2.3 In-sights of Raman Peaks of Various MoS_2 layers thicknesses 37

5.2.4 Importance of Thin Oxide in Electrical Devices 39

5.2.5 $MoS_2/SiO_2/Si$ with Various SiO_2 Thicknesses 40

5.2.6 The Excitation Power Dependence of PL Spectra 42

5.2.7 XPS Characterization of MoS_2 Monolayers 43

CHAPTER 6. MOS_2 MONOLAYERS GROWN ON GALLIUM NITRIDE SUBSTRATES 45

6.1 Introduction 45

6.2 Experimental 45

6.3 Results and Discussion 46

6.3.1 Topological Characterization by Scanning Electron Microscope 46

6.3.2 Topological Characterization by Atomic Force Microscopy 47

6.3.3 Comparison of MoS_2 growth on GaN with Other Substrates 49

6.3.4 XPS Analysis of as Grown MoS_2 on GaN Substrate 50

CHAPTER 7. MOS_2 MONOLAYERS GROWN ON GA_2O_3 SUBSTRATES 52

7.1 Introduction 52

7.2 Experimental 52

7.3 Results and Discussion 53

7.3.1 Topography Study of MoS_2/Ga_2O_3/Sapphire Sample 53

7.3.2 Comparison of Raman Spectra of MoS_2/Ga_2O_3 with Other Substrates 54

7.3.3 Comparison of PL Spectra of MoS_2/Ga_2O_3 with Other Substrates 56

CHAPTER 8. APPLICATIONS OF CVD GROWN MOS_2 MONOLAYERS 60

8.1 Introduction 60

8.2 Fabrication of Interdigitated Device 60

8.3 Photodetector 63

8.3.1 Current-Voltage (I-V) Characteristics of Photodetector 63

8.3.2 Photo-Responsivity vs. Wavelength of Photodetector 64

8.3.3 Photo-Responsivity and Gain vs. Incident Light Intensity 66

8.4 Carbon Dioxide Gas sensor 68

8.4.1 Experimental Set-up.... 69

8.4.2 Results and Discussion 70

CHAPTER 9. NOISE 73

9.1 Introduction....73

9.1.1 Shot Noise.... 73

9.1.2 Thermal Noise or Johnson Noise.... 74

9.1.3 Flicker Noise or 1/f Noise or Pink Noise.... 74

9.2 Experimental....76

9.3 Results and Discussion 77

CHAPTER 10. 2D $MO_{1-X}W_XS_2$ TERNARY COMPOUNDS ON SAPPHIRE SUBSTRATES....79

10.1 Introduction....79

10.2 Experimental....79

10.3 Results and Discussion 80

10.3.1 Topography Study by Optical Microscope 80

10.3.2 Micro-Raman Characterization of as Grown Ternary Compounds 80

10.3.3 Micro-PL Characterization of as Grown Ternary Compounds.... 81

CHAPTER 11. HETEROSTRUCTURES....83

11.1 Introduction....83

11.2 Experimental Growth of Lateral Heterostructures....85

11.3 Results and Discussion 86

11.3.1 Topography Study by Scanning Electron Microscope and Confocal Microscope.... 86

11.3.2 Optical Characterization of core, shell and junction regions of MoS_2/WS_2 Heterostructure 87

11.3.3 Surface Morphological and Kelvin Probe Force Microscope Characterization of MoS_2/WS_2 Heterostructure on Sapphire and on Gold Substrates 89

11.3.4 Tip Enhanced Raman Spectroscopy (TERS) Characterization of MoS_2/WS_2 Heterostructure on Gold Substrate 96

11.4 Experiment to Stack Vertical Heterostructures 105

11.5 Results and Discussion 107

11.5.1 Optical Characterization of stacked regions of vertical $MoS_2/Mo_xW_{1-x}S_2$ Heterostructure 107

CHAPTER 12. SUMMARY AND CONCLUSION 111

12.1 Section I Summary 111

12.2 Section I Conclusion 112

12.3 Section II Summary 114

12.4 Section II Conclusion 115

REFERENCES 117

LIST OF TABLES

Table 1: Physical properties of growth materials and used substrates.....6

Table 2: Growth temperature vs. MoS_2 domain size 20

Table 3: Comparison chart of finding the properties of MoS_2 monolayer on different substrates 59

Table 4: Extracted values of Ist order Raman modes in WS_2 from the above figure. 102

Table 5: All possible combinations of 2^{nd} order phonon Raman modes by combining single phonon modes from the above table.....102

Table 6: TERS peaks of shell WS_2 region and an alloyed interface region at 638nm and 785nm excitation wavelengths.....103

Table 7: PL positions and the respective TERS spectra of various alloyed samples 104

LIST OF FIGURES

Figure 1-1.Catagory of different types of 2D materials....2

Figure 1-2: layered structure of 2D transition metal dichalcogenides....2

Figure 1-3.a Side view of bulk MoS_2 (van der Walls bonded MoS_2 units), b top view of both bulk MoS_2 and monolayer MoS_2, c side view of monolayer MoS_2....3

Figure 1-4.Band structures of (a) bulk MoS_2, (b) quadrilayer....4

Figure 1-5. Band structures of bulk WS_2, and monolayer WS_2[4] 5

Figure 1-6.Schematic diagram of the study of CVD grown MoS_2 monolayers 5

Figure 2-1: Mechanisms of emission of various electron signals from the sample in SEM 8

Figure 2-2: JEOL 7000F SEM, front and side view and labelled all the detectors 9

Figure 2-3: Typical AFM configuration 12

Figure 2-4: XPS physics and spectra of copper....14

Figure 2-5: Kratos Axis Ultra DLD XPS at AARC UA....15

Figure 2-6:Energy levels of sample and the metallic tip: (a) sample and tip are not in contact and separated by distance d, (b) sample and tip are in contact and generates V_{CPD}, (c) applied external bias V_{DC} to compensate V_{CPD} 17

Figure 2-7: (a) TERS gold tip, (b) illustration of TERS mechanism....18

Figure 3-1:CVD setup....20

Figure 3-2: SEM analysis of MoS_2 flake size grown at different growth temperatures....21

Figure 3-3: Raman Spectra of MoS_2 grown at different temperatures. 22

Figure 3-4: PL spectra of MoS_2 grown at different temperatures....23

Figure 3-5:Uniformity study of as grown MoS_2 flake on sapphire substrate. 24

Figure 3-6. Excitation power dependence PL spectra of MoS2 monolayer, inset is the log-log plot of PL intensity vs incident laser power 25

Figure 3-7. XPS spectra present the Mo and S peaks 26

Figure 3-8.AFM characterization of CVD MoS_2 flakes 26

Figure 3-9.PL spectra at room and low (7k) temperature 27

Figure 3-10.Valley selectivity by the polarized incident light 28

Figure 3-11.Detection of σ+ and σ- emission after illumination by σ+ excitation 29

Figure 4-1. Schematic diagram process for Patterning by microfabrication 31

Figure 4-2. Different sized circular patterns on sapphire substrates 31

Figure 4-3.Schematic diagram of MoS_2 growth on specific areas 32

Figure 4-4.SEM images of grown MoS2 flakes on specific locations 33

Figure 4-5. Raman and PL spectra at 80μm patterned and inset is OM image 34

Figure 4-6. Raman and PL spectra at 50μm patterned and inset is OM image 34

Figure 5-1.SEM images of MoS_2 monolayer flakes and thin film region (scale bar is 200μm) 36

Figure 5-2.Optical images present the monolayer and bilayer MoS_2 regions 36

Figure 5-3. Raman and PL spectra of 1L, 2L, 3L and bulk MoS2 37

Figure 5-4.Raman FWHM vs MoS_2 layers 38

Figure 5-5. MoS_2 characteristic Raman peak positions and their difference vs MoS_2 layers 39

Figure 5-6.Schematic of device on SiO_2/Si substrate 40

Figure 5-7. Raman peaks FWHM of 1L MoS_2 grown on differently thick SiO_2 41

Figure 5-8. PL FWHM of 1L MoS_2 grown on differently thick SiO_2 42

Figure 5-9.Excitation power dependence PL spectra of MoS_2 monolayer, inset is the log-log plot of PL intensity vs incident laser power 43

Figure 5-10.XPS analysis of Mo and S binding energies of CVD grown MoS_2 44

Figure 6-1.SEM images of CVD MoS_2 grown on GaN/sapphire substrate.....46

Figure 6-2.orientation of grown MoS_2 flakes on sapphire and GaN/sapphire substrates.....47

Figure 6-3.SEM images of CVD MoS_2 grown on pure GaN substrate 47

Figure 6-4.AFM topography of bare GaN/sapphire substrate 48

Figure 6-5.AFM analysis of CVD MOS_2 on GaN/sapphire substrate in height and phase imaging 48

Figure 6-6.AFM topography of bare GaN substrate.....49

Figure 6-7. AFM of CVD MoS_2 on GaN substrate in height and phase imaging 49

Figure 6-8.Raman and PL characterization of MoS_2 monolayer on GaN 50

Figure 6-9.XPS comparison of MoS_2 on GaN substrate.....51

Figure 7-1.Optical and atomic force microscope images of MoS2 monolayers on sapphire, annealed Ga2O3 and un-annealed Ga2O3 substrates 54

Figure 7-2.Raman analysis.....56

Figure 7-3.Photoluminescence spectra 58

Figure 7-4.PL FWHM of trion, exciton dependence on substrate, and dependence of trion/exciton on the dielectric constant.....58

Figure 8-1. Schematic diagram of detailed experiment to fabricate interdigitated pattern 61

Figure 8-2. Steps to transfer MoS_2 monolayers by PMMA.....62

Figure 8-3.Two terminal MoS_2 interdigitated device 62

Figure 8-4.Probe station to measure I-V characteristics of device 63

Figure 8-5.Schamatic illustration of the photodetector.....63

Figure 8-6.Current-voltage characteristics of (a) monolayer MoS_2, in dark conditions and when illuminated under λ=450 and 530nm light. 64

Figure 8-7. Spectral photo-responsivity of the photodetector 65

Figure 8-8. Absorbance spectra on MoS_2 monolayer 66

Figure 8-9. Spectral responsivity and Gain dependence on incident power density 68

Figure 8-10. Schematic illustration of electron transfer from CO2 to MoS_2 monolayer.....69

Figure 8-11. MoS_2 monolayer gas sensor setup.....70

Figure 8-12.Sensor response to different concentrations of CO_2 gas 71

Figure 8-13. Sensor response to different exposure time of CO_2 gas.....71

Figure 8-14.Sensitivity vs CO_2 concentration 72

Figure 9-1: PSD with frequency for single trap state 75

Figure 9-2: 1/f dependence of PSD due to many trap states[122].....76

Figure 9-3. Spectrum Analyzer.....76

Figure 9-4: Schematic diagram of measurement setup of noise 77

Figure 9-5: NSD with the frequency.....77

Figure 9-6: Specific detectivity values at different wavelengths.....78

Figure 10-1. Optical images of as synthesized $Mo_{1-x}W_xS_2$ monolayered triangles.....80

Figure 10-2. Micro-Raman spectra at different compositions of $Mo_{1-x}W_xS_2$ monolayers 81

Figure 10-3. Micro-PL spectra at different compositions of $Mo_{1-x}W_xS_2$ monolayers.....82

Figure 11-1: Type II band alignment diagram of MoS2/WS2 heterostructure.....84

Figure 11-2: Illustration of CVD to grow MoS_2/WS_2 HS 85

Figure 11-3: Illustration of variation of vapor pressure to deposit the LHS.....86

Figure 11-4: SEM images of MoS_2/WS_2 heterostructures.....87

Figure 11-5. Confocal microscope image of heterostructure with an inset image with dimensions 87

Figure 11-6. Optical microscope images and the Raman and PL characterization of heterostructures.....89

Figure 11-7. Topography image and corresponding step height analysis of a lateral heterostructure MoS_2/WS_2 crystal. 90

Figure 11-8. Scanning kelvin probe force microscopy imaging and contact potential difference across the MoS_2/WS_2 regions. 90

Figure 11-9. Optical image of selected MoS_2/WS_2 crystal on sapphire substrate for the analysis by SKPFM.....91

Figure 11-10. Topography and CPD imaging of another MoS_2/WS_2 monolayer crystal.....92

Figure 11-11: PL spectra and PL mapping images collected at (a) 638nm, (b) 532nm excitation wavelengths.....93

Figure 11-12: Illustration of transfer of MoS_2/WS_2 heterostructures from the sapphire substrate using a thin gold film.....94

Figure 11-13. Optical image of same heterostructure crystal to be analyzed on before transfer (sapphire substrate) and after transferred on gold substrate 95

Figure 11-14. (a) topography image and same heterostructure crystal on gold substrate with corresponding height profile (c), (b) SKPFM image of same crystal and the corresponding potential profile in (d), (e) again the topography image of as grown crystal before transfer just for the close comparison. 96

Figure 11-15: (a) CPD image of same heterostructure crystal on gold substrate, (b) Zoom in image of same crystal and (c) inset is the TERS image with a 638nm excitation, (d) collected TERS spectra at MoS_2, WS_2 and the junction, (e) Zoom in TERS spectra from 100 to 700cm^{-1}. 98

Figure 11-16: (a) TERS spectra collected at MoS_2, WS_2 and junction at non-resonant 785nm wavelength and the corresponding TERS image, (b) Zoom in TERS spectra from 300 to 600cm^{-1} 99

Figure 11-17: Comparison of TERS spectra at 638nm and 785nm excitation wavelengths.....100

Figure 11-18: Phonon dispersion relation for WS_2 monolayer.....101

Figure 11-19: (a) Confocal PL spectra of different alloy samples at 532nm excitation, (b) TERS spectra of same positions at 785nm excitation and the variation of A”$_2$ peak position is noted.....104

Figure 11-20: Topography and CPD images of various alloys.....105

Figure 11-21: PDMS stamping process to transfer 2D materials 106

Figure 11-22. Optical microscope images of stacked $MoS_2/Mo_xW_{1-x}S_2$ heterostructure.....107

Figure 11-23: Left, Raman spectra and right PL spectra at the colored points on an optical images at 532nm excitation wavelength.....108

Figure 11-24: PL spectra collected colored points of VHS and PL mapping image at 636nm emission wavelength.....110

Figure 11-25: Optical image of VHS with the corresponding Raman spectra at the colored points shown in an optical image and also the Raman mapping image at MoS_2 peaks 385cm^{-1}, 407cm^{-1} also at WS_2 peak 419cm^{-1}.....110

CHAPTER 1.
INTRODUCTION

1.1 Background

The revolutionary applications of graphene intrigue to explore the other atomically thin 2D materials with extraordinary properties. These include borophene (2D boron)[1,2], germanene[3,4,5], phosphoerene[6,7], silicone (2D silicon)[8,9], MXenes (2D carbides/nitrides)[10,11] and 2D transition metal dichalcogenides (2D TMDs)[12,13,14,15,16,17]. Based on the chemical composition, sub-nanometer thick 2D materials are categorized as insulating, semiconducting and metallic. In all of these 2D materials, 2D TMDs sparked huge interest because of almost as thin, flexible and transparent as graphene. Transition metal dichalcogenides TMDs (MX_2) are a class of materials that exist in bulk as vertically stacked monolayers with weak van der wall interactions between them. In the chemical formula MX_2, M is a transition metal (Mo, W, Ti, Nb and so on) and X is a chalcogen (S, Se and Te). These TMDs are studied extensively because of some TMDs (MoS_2, WS_2, $MoSe_2$, WSe_2) exhibit the semiconducting behavior with transition of indirect to direct bandgap as TMD changes from bulk to monolayer form[18],[19]. This unique behavior endows them with novel and exotic properties in an optical and quantum field such as valley Hall effect and spin-valley physics, which can lead to their potential applications as an effective field effect transistors (FETs) with an appropriately high on/off ratio, photosensors, photovoltaics and in the transparent and flexible electronic devices[20,21,22,23,24,25,26,27].

<table>
<tr><td>Graphene family</td><td>Graphene</td><td colspan="2">hBN
'white graphene'</td><td>BCN</td><td>Fluorographene</td><td>Graphene oxide</td></tr>
<tr><td rowspan="2">2D chalcogenIdes</td><td colspan="2" rowspan="2">MoS_2, WS_2, $MoSe_2$, WSe_2</td><td colspan="2" rowspan="2">Semiconducting dichalcogenides:
$MoTe_2$, WTe_2,
ZrS_2, $ZrSe_2$ and so on</td><td colspan="2">Metallic dichalcogenides:
$NbSe_2$, NbS_2, TaS_2, TiS_2, $NiSe_2$ and so on</td></tr>
<tr><td colspan="2">Layered semiconductors:
GaSe, GaTe, InSe, Bi_2Se_3 and so on</td></tr>
<tr><td rowspan="2">2D oxides</td><td>Micas,
BSCCO</td><td colspan="2">MoO_3, WO_3</td><td colspan="2" rowspan="2">Perovskite-type:
$LaNb_2O_7$, $(Ca,Sr)_2Nb_3O_{10}$,
$Bi_4Ti_3O_{12}$, $Ca_2Ta_2TiO_{10}$ and so on</td><td>Hydroxides:
$Ni(OH)_2$, $Eu(OH)_2$ and so on</td></tr>
<tr><td>Layered
Cu oxides</td><td colspan="2">TiO_2, MnO_2, V_2O_5,
TaO_3, RuO_2 and so on</td><td>Others</td></tr>
</table>

Figure 1-1.Catagory of different types of 2D materials[28]

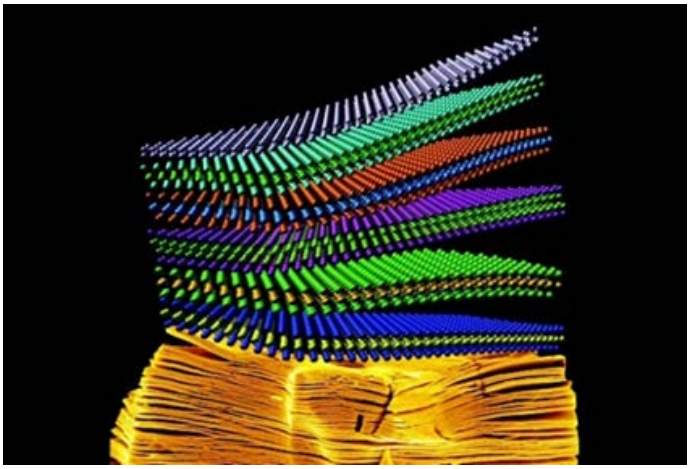

Figure 1-2: layered structure of 2D transition metal dichalcogenides

The MoS_2 crystals occur naturally in the form of two structures, 2H-MoS_2 and 3R-MoS_2, both structures have the trigonal prismatic coordination[29,30,31]. The unit cell of 2H-MoS_2 consists of two layers which are stacked in the hexagonal (H) symmetry as shown in Figure 1-3, while unit cell of 3R-MoS_2 structure consists of three layers in the rhombohedral (R) symmetry. In both structures of MoS_2, 2H-MoS_2 is the more dominant and more stable form of MoS_2. The bulk MoS_2 is made up of Vander Walls bonded single S-Mo-S layers. The layered MoS_2 material, interlayer bonding is very weak as compared to intralayer bonding. Each single stable S-Mo-S layer is referred as a monolayer 1H-MoS_2.

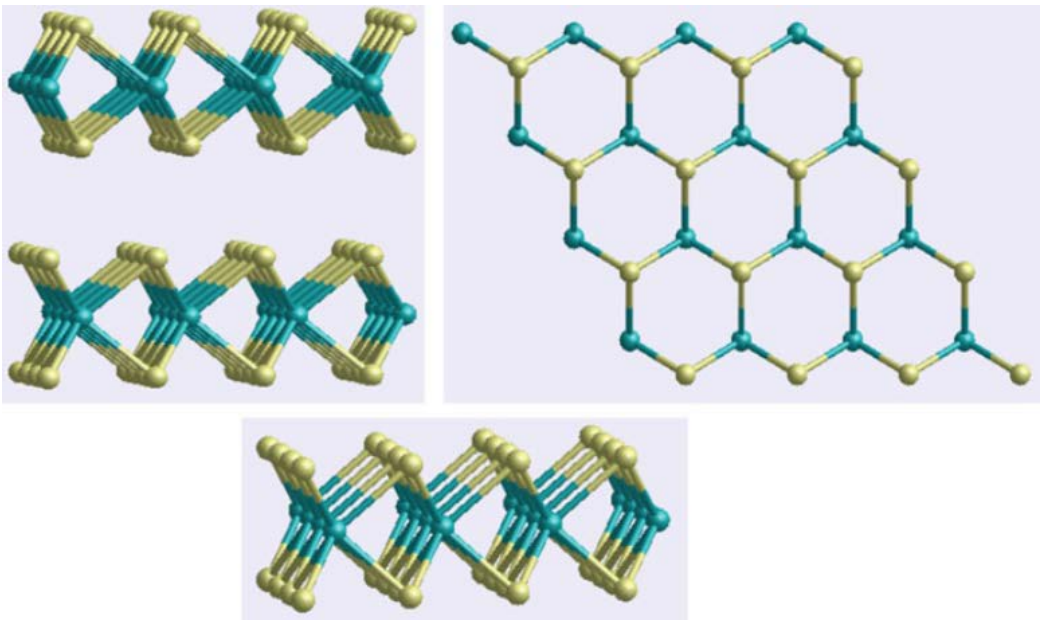

Figure 1-3.a Side view of bulk MoS_2 (van der Walls bonded MoS_2 units), b top view of both bulk MoS_2 and monolayer MoS_2, c side view of monolayer MoS_2

Among all the TMDs, semiconducting MoS_2 has been explored most extensively because of its complementary nature to graphene and a transition from indirect bandgap in bulk 1.29eV to direct bandgap 1.85eV in monolayer form[18]. MoS_2 monolayer based FET was realized with an ultralow power dissipation and high on/off ratio 10^8, ultrasensitive photodetectors. Highly efficient LEDs were investigated based on WSe_2 based p-n junctions. Also, the anisotropic behavior in black phosphorous and TMDs (ReS_2, $ReSe_2$) has been noted lately, which can be beneficial to control the device performance based on the crystal orientation[32,33]. Recent study shows monolayer MoS_2 possess a huge potential to replace state-of-art silicon based transistors, which is struggling to keep up (with an ever shrinking device technology at nanoscale level. Recently a batch fabrication of 8,100 FETs based on MoS_2 on a 4inch SiO_2/Si wafer has been reported[34]. MoS_2 monolayer has been used for an application for anti-exocytosis-enhanced synergistic cancer therapy[35].

Figure 1-4 shows the change of indirect bandgap to direct bandgap semiconductor as MoS_2 layer thickness decreases from bulk to monolayer[36]. This transition in bandgap is explained as the conduction band states at K points are formed by d-orbitals at Mo atoms. At K, the occupied band has d_{xy}-$d_{x^2-y^2}$ character and unoccupied band is dominated by d_{z^2}character. These states have a minimal interlayer coupling effect because Mo atoms are located in the middle of S-Mo-S unit cell. However, the electronic states near the Γ points are combinations of d-orbitals from Mo atoms and antibonding p_z orbitals from S atoms and have strongly been affected by the interlayer coupling. The energies of these states primarily depend upon the layer thickness. Therefore, as the MoS_2 layer number decreases, the layer-layer interaction also decreases and lowers the energy of antibonding orbitals at Γ point[37]. Thus, the direct excitonic bandgap near K point remain unchanged, but the transition in the indirect bandgap at Γ point changes to much larger value. This unusual behavior of MoS_2 monolayer paves a way for potential applications in sensing, optoelectronic and photonic devices.

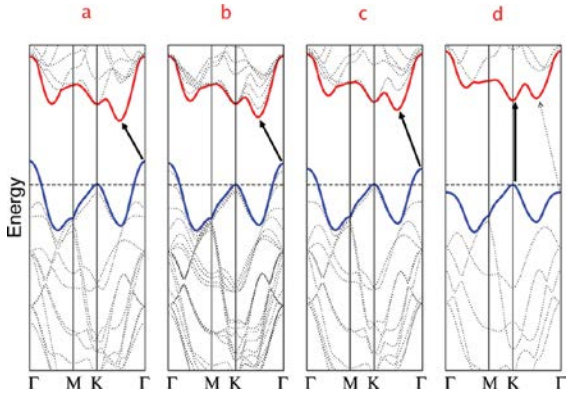

Figure 1-4.Band structures of (a) bulk MoS_2, (b) quadrilayer MoS_2, (c) bilayer MoS_2, and (d) monolayer MoS_2[36]

Like MoS_2, WS_2 exist as an indirect bandgap of 1.3eV in bulk form, but changes to direct bandgap of 2.01eV in monolayer form[38].

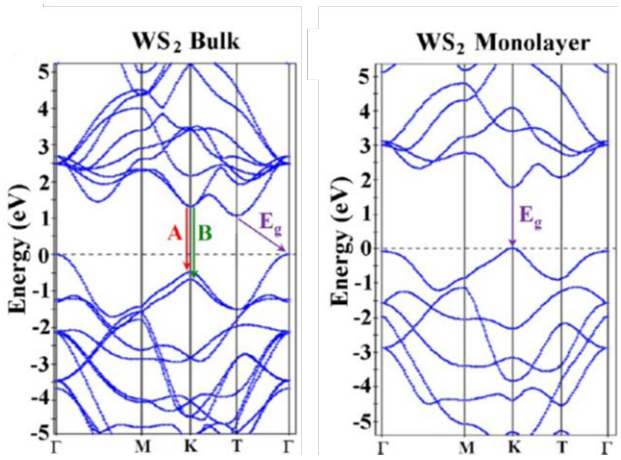

Figure 1-5. Band structures of bulk WS_2, and monolayer WS_2[38]

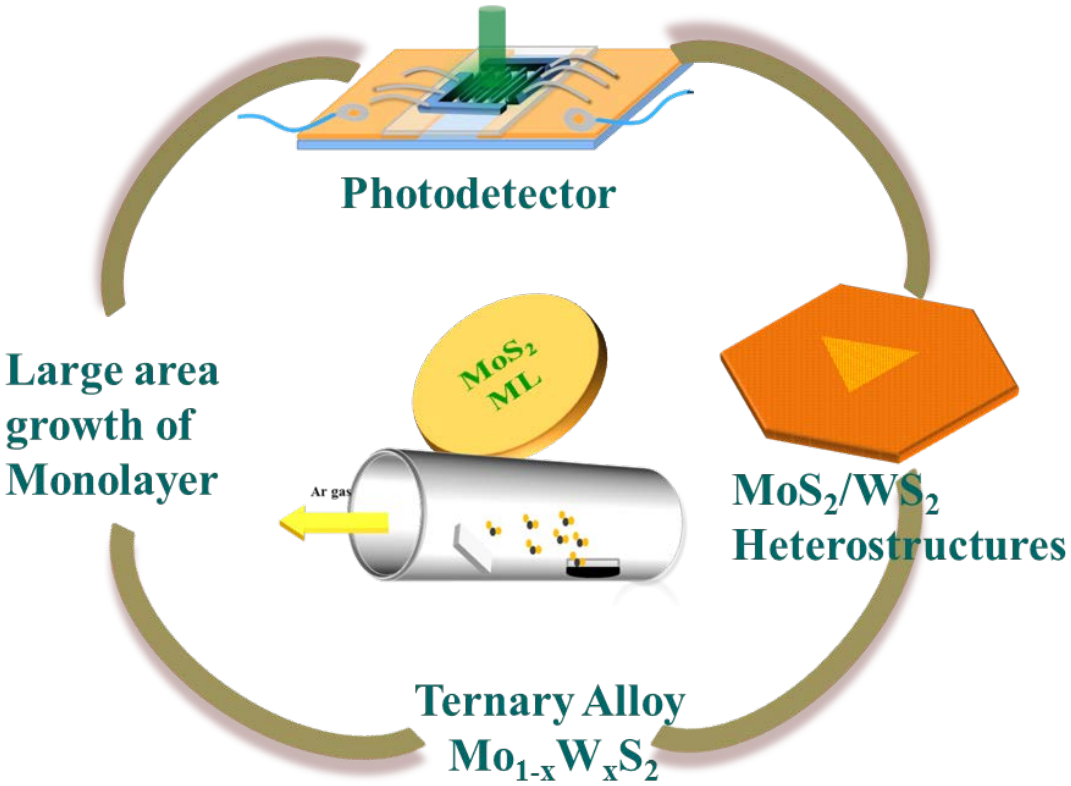

Figure 1-6.Schematic diagram of the study of CVD grown MoS_2 monolayers

In this dissertation, the study on MoS_2 monolayers has been sectioned into four parts as shown in the schematic in Figure 1-6. The first part involves the large area monolayer MoS_2 growth using conventional low pressure chemical vapor deposition (LPCVD) on many different insulating and semiconducting substrates such as (0001) sapphire, (100) SiO_2/Si, GaN and Ga_2O_3 substrates and

also the systematic study to explore the optical and crystalline nature of as grown monolayer flakes from CHAPTER 3 to CHAPTER 7. The significant impact of the dielectric constant of the substrate on the MoS2 PL peak position has been studied thoroughly. The complete set of properties of MoS_2, WS_2 and all different substrates used for the growth is mention in Table 1.

Table 1.Physical properties of growth materials and used substrates

Physical Properties						
	MoS_2	**WS_2**	**Sapphire**	**Silicon**	**GaN**	**β-Ga_2O_3**
Crystal Structure	$P6_3/mmc$ (hexagonal)	$P6_3/mmc$ (hexagonal)	$\bar{3}m$ (hexagonal)	m3m (Cubic)	$P6_3mc$ (Wurtzite)	C_{2h}^3 (C2/m) (monoclinic)
Melting Point (°C)	1185	1250	2040	1414	2500	1900
Lattice Constant (Å)	a = 3.15 c = 12.29	a = 3.16 c = 12.32	a = 4.76 c = 12.99	a = 5.43	a = 3.187 c = 5.16	a = 12.23 c = 5.8
Thermal exp. Coefficient (K^{-1})	a = 1.9 x 10^{-6} c = 8 x 10^{-6}	14.8 x 10^{-6}	a = 8 x 10^{-6} c = 5.0 x 10^{-6}	2.5 x 10^{-6}	a = 5.59 x 10^{-6} c = 3.17 x 10^{-6}	a = 3.7 x 10^{-6} c = 6.34 x 10^{-6}
Thermal Conductivity (W/mK)	131	142	23	142	160	10-30
Band Gap (Bulk) (Monolayer)	1.2-1.3eV (Indirect) 1.8-1.9eV (Direct)	1-1.3eV (Indirect) 1.95-2.01eV (Direct)	Insulator (10eV)	1.12 eV	3.4 eV	4.8eV

In CHAPTER 8, the large area two terminal electrical device has been fabricated on as-grown MoS_2 monolayer film using microfabrication techniques. The device electrical response to light

has been demonstrated through I-V characteristics. In addition, the photoresponse capability of the device has been explored by studying photo-responsivity and gain of the photodetector device. Moreover, the same device gas sensing ability was investigated using CO_2 gas and the minimum detection limit of the device was found to be 200ppm. Existence of noise at low frequencies is very crucial factor to decide the true sensitivity of the device. Thus, in CHAPTER 9, we have talked about different types of noises and find the most important 1/f noise. This 1/f noise was used to find the specific detectivity of the photodetector. CHAPTER 10 is dedicated to the ternary compounds in which different concentrations of W was doped in MoS_2 monolayers. The doping effects the bandgap of the material and results in bandgap can be tuned between pure MoS_2 (1.85eV) to pure WS_2 (2.01eV). Finally, in CHAPTER 11, we are discussed the lateral and vertical MoS_2/WS_2 heterostructures. Lateral heterostructures were grown by one step CVD synthesis method, however, vertical heterostructures were synthesized by manually stacking MoS_2 monolayers on top of WS_2 monolayers by PDMS stamping method. TERS coupled with SPM was used to explore the nano features hidden at the transition region of lateral heterostructures. Transition region was explored to be ternary alloy and the minimum width of the region was detected to be pixel limited 25nm between MoS_2 and WS_2 regions.

CHAPTER 2.
CHARACTERIZATION TECHNIQUES

2.1 Scanning Electron Microscope

Scanning electron microscope (SEM) scanned the sample surface using an electron beam in raster scan pattern and produces sample image and its composition. When an incident electron beam interacts with an atoms in the sample, various signals are emitted which includes secondary electrons (SE), back-scattered electrons (BSE) and characteristic x-rays depending upon the type of interaction as shown in Figure 2-1.

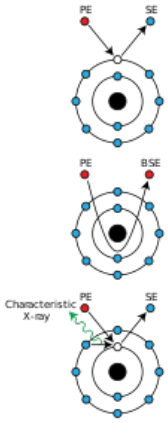

Figure 2-1: Mechanisms of emission of various electron signals from the sample in SEM

The most common mode in SEM is the secondary electron mode, in which in-elastically secondary electrons are emitted from the top atoms of the sample surface when excited by the incident electron beam. Later these secondary electrons are detected by secondary electron detector called Everhart-Thornley detector. Secondary electrons carry very low energy around

50eV and thus, only can be emitted from the top of the sample surface. The collection of secondary electron makes it feasible to study the topography images of the sample. Back scattered electrons are the elastic scattering of the incident beam from the sample. Since BSE emerges from the deeper portion of the sample and also the intensity of BSE is dependent upon the atomic number of the specimen, so, it is used to study the chemical composition of the sample, but not the identity of different elements present. However, the elemental analysis has been done by detecting characteristic x-rays which emits when an electron beam removes an electrons from the inner shell of the atoms and are detected by energy dispersive x-ray spectroscopy (EDS) or wavelength dispersive x-ray spectroscopy (WDS).

Figure 2-2: JEOL 7000F SEM, front and side view and labelled all the detectors

The basic SEM setup consists of electron gun which could be either thermionic or field emission gun (FEG), condenser lens and the scanning coils. In the typical mechanism, an electron beam emitted from the electron gun is focused or controlled the spot size by the condenser lens or an

electromagnetic lens. Scanning or a pair of deflector plates are used to deflect the electron beam in the X and Y axis to raster scan over the sample surface. A JEOL 7000F SEM, equipped with a FEG of Schottky type, SED, BSD, EDS and WDS was used in our analysis. The electron beam energy can be adjusted between 0-30KeV with a maximum resolution of 1nm at 15KV. The picture of front and side views of JEOL 7000F is shown in Figure 2-2.

2.2 Micro - Raman Spectroscopy

Raman spectroscopy is an optical scattering technique which is widely used to study the identity of the tested materials. In this characterization, a set laser wavelength is impinged on the material and after reflection from the sample surface, a shift in the position of incident wavelength occurs due to the interaction with the samples molecular vibrational or rotational energy levels. The shift in the higher wavelength which is called a stokes shift is most usually captured by the detector. Raman is a non-destructive technique and not much sample preparation technique is required. In addition, Raman peaks for individual molecules are distinct, thus, the sample composition can be detected using Raman spectroscopy. Now-a-days, Raman spectroscopy has become an indispensable tool to characterize the material under investigation as the Raman spectral lines are extremely sensitivity to the material quality, crystalline nature. The FWHM of Raman lines have been used to check the crystalline quality of the material. Lower FWHM corresponds to higher crystalline nature of the material.

Raman spectroscopy measured Raman spectra in terms of wavenumbers (cm^{-1}), which is relative to the excitation wavelength. If the Raman inelastic scattering signal is located at λ_{Raman}(nm) then the shift in Raman signal relative to the excitation wavelength is given by,

$$\text{Raman shift } (cm^{-1}) = 10^7 \left(\frac{1}{\lambda_{excitation\ laser\ [nm]}} - \frac{1}{\lambda_{Raman\ [nm]}}\right) \quad (1)$$

In our Raman spectrometer, excitation laser wavelength is 532nm imping on the sample with 200mW optical power. The scattered signal after passes through the same objective reaches to the monochromator after filtered by 532nm notch filter. And finally, from the SP-2500, the Raman signal was detected by Pixis 100 camera.

2.3 Atomic Force Microscope

Atomic force microscopy is a high-resolution imagining technique where it demonstrates a resolution as tiny as a fraction of a nanometer or in the order of an angstrom. The AFM set up consists of silicon or silicon nitride cantilever with a sharp tip of the order of 20-30nm. When the tip comes closer to the sample surface, adhesive forces sets up between the sample and the tip, which attracts tip towards sample. However, when the tip touches the sample surface, repulsive forces sets up, which repel the tip away from the sample surface. The deflection of the laser light hit on the cantilever tip depends upon this attraction and repulsion of the tip which creates an image on the screen. Usually an AFM is operated in a tapping mode to protect the sample surface from the tip scratches and to keep the tip clear of any accumulation of dust on the sample surface.

In this mode, a cantilever tip oscillates at a particular frequency called the resonance frequency and the amplitude of the oscillation is set between few nanometers to 200nm. The frequency of the oscillation is fixed, and an amplitude also stays constant until the cantilever tip has no interaction with the sample surface. As the tip comes closer to the sample surface, the types of interactions such as Vander Waal's interaction, dipole-dipole interaction, electrostatic interaction between the tip and the sample surface causes a change in the amplitude of the cantilever tip and results in the change in the deflection of the laser light striking on the head of

the tip. This change in the deflection makes a sample image by capturing a laser light on the photographic plate. In this tapping mode imaging, a phase contrast image between cantilever oscillation and driving signal can be plotted as well. This type of imaging is advantageous in which sample consists of different regions of uniform thickness but having different chemical compositions with a varying adhesive property and are not distinguishable in the topographic image.

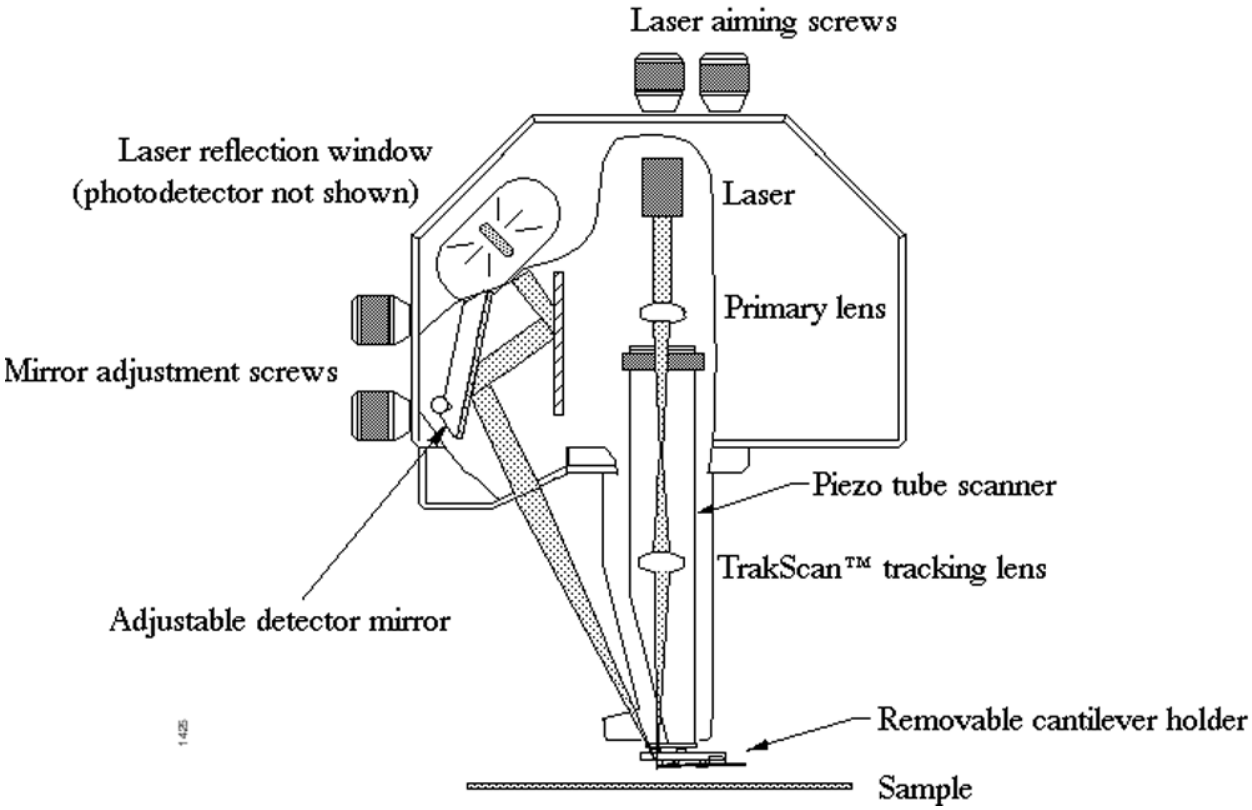

Figure 2-3: Typical AFM configuration

Figure 2-3 illustrates the typical AFM assembly of Digital Instruments 3100 AFM available at UA analytical research center. The imaging process was done by operating the AFM cantilever tip at the frequency range between 100KHz to 500KHz with a center at 333KHz. Scan rate was set at 1Hz. Regarding the lateral resolution of an image is depended upon the radius of curvature of the tip. Sharper the tip, better will be the lateral resolution. In addition to the radius of

curvature, samples/line option is also crucial factor to determine the lateral resolution. The samples/line features the number of data points collected in the image in X and Y scan direction. Individual data points are called pixels. Available options of samples/line in an AFM are 512, 256 and 128. The size of the individual data point (pixel) selects the lateral resolution as we are not able to resolve features of sizes smaller than the pixel size. For instance, scanned image of 50µm x 50µm size with the samples/line selected at 512, then the pixel size will be 50µm ÷512 = 98nm. So, we cannot resolve features smaller than 98nm size in a 50µm sized image. But if we want to resolve smaller features then we need to reduce the size of an image. As an example, select the image size 5µm with the samples/line 512. Then the lateral resolution will be 5µm ÷512 = 9.8nm.

2.4 X-Ray Photoelectron Spectroscopy

X-ray photoelectron spectroscopy (XPS) is a powerful surface analysis technique that can detect types of elements present in a material, their oxidation states, and the overall electronic structure. In an XPS technique, an intense beam of x-rays (Al Kα X-rays, E_{photon} = 1486.7 eV) from the source are irradiated upon the sample surface which further ejects large number of electrons from the core of the atoms as shown in Figure 2-4.

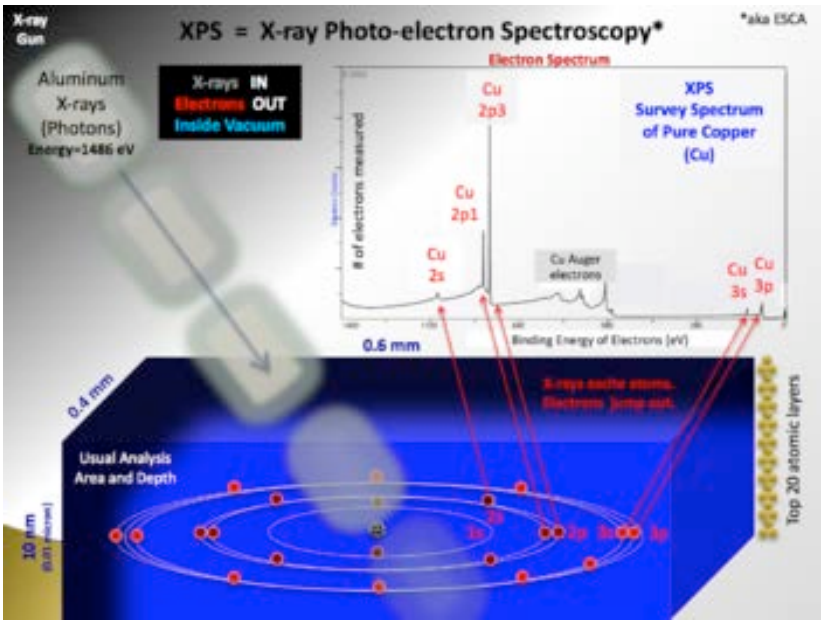

Figure 2-4: XPS physics and spectra of copper

The kinetic energy of the emitted electrons are measured by the instrument and the binding energy of the electrons is calculated using the relation,

$$E_{binding} = E_{photon} - (E_{kinetic} + \phi) \quad (2)$$

ϕ is the work function of the material and this equation follows the conservation of energy equation and is used to calculate the binding energy of the emitted electrons.

Figure 2-5: Kratos Axis Ultra DLD XPS at AARC UA

An XPS system named Kratos Axis Ultra DLD at UA analytical research center was used to collect an XPS data. This system is installed with a dual (Al/Mg) and a monochromatic Al X-ray source, and an electron analyzer. This instrument has a spatial resolution of < 3µm and has an ability to scan large area ~700 x 300µm. An argon ion sputter gun is also fitted in this instrument for the depth profiling analysis on the samples. The typical base pressure in the analysis chamber of an XPS is < 8 x 10^{-10}Torr.

2.5 Scanning Kelvin Probe Force Microscope

Scanning kelvin probe microscopy (SKPFM) is another variant of AFM in which the cantilever tip is oscillating by the applying small signal AC voltage between the cantilever tip and the surface of the sample unlike the mechanical vibration of tip at the resonance frequency in conventional AFM. In this technique, the contact potential difference (CPD) between the

metallic AFM tip and the sample surface is measured, and results in the work function or CPD mapping of the sample with high spatial resolution can be collected.

In SKPFM, CPD is measured between the conducting AFM tip and the sample's surface, therefore, the CPD is defined as[39],

$$V_{CPD} = \frac{\varphi_{tip} - \varphi_{sample}}{q} \quad (3)$$

Where φ_{tip} and φ_{sample} are the work functions of the tip and the sample, q is the electronic charge. Figure 2-6 illustrates the generation of V_{CPD} between the tip and sample in three steps. In step 1, (a) sample and the metallic tip are not in contact and are separated by distance d, therefore no electron tunneling takes from the tip to the sample or vice versa. In step 2, (b) the metallic tip and the sample are brought in close contact with each other, which cause the fermi levels alignment by flowing electrons between the tip and the sample until the equilibrium is reached. The alignment of fermi levels will generate V_{CPD} between the conduction bands of tip and the sample surface. In step 3, (c) an apparent V_{CPD} can be compensated if an external bias V_{DC} is applied opposite to V_{CPD} and brings the fermi levels of the tip and the sample back to their original positions. The amount of external DC biased voltage V_{DC} that eliminated the V_{CPD} is the work function value of the sample.

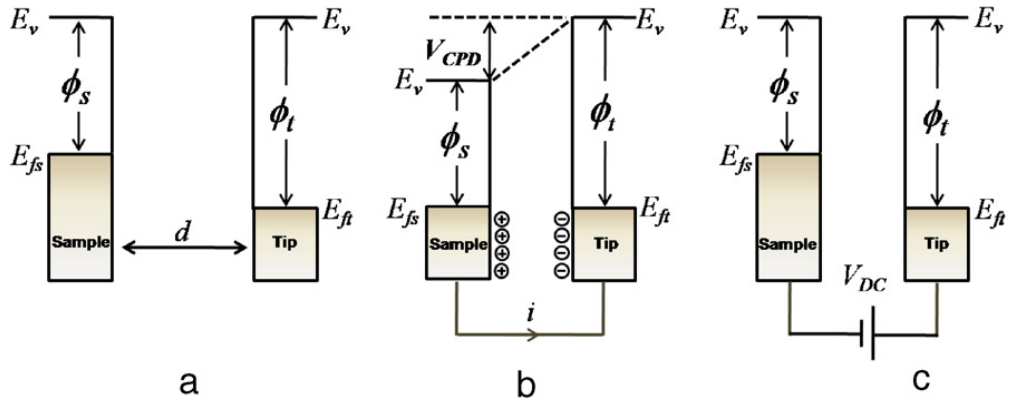

Figure 2-6: Energy levels of sample and the metallic tip: (a) sample and tip are not in contact and separated by distance d, (b) sample and tip are in contact and generates V_{CPD}, (c) applied external bias V_{DC} to compensate V_{CPD}

By applying both an AC and DC voltage to the cantilever tip, work function of the sample can be measured in SKPFM. V_{AC} oscillates the tip at the set frequency and generates an electrostatic force between tip and the sample and the V_{DC} is applied to eliminate the V_{CPD} between the tip and the sample and brings the cantilever tip to the minimum vibration. The resultant applied voltage between the tip and the sample is

$$\Delta V = (V_{DC} - V_{CPD}) + V_{AC} \,.\, \sin(\omega t) \qquad (4)$$

The resulting electrostatic force between the tip and the sample is written as

$$F = \frac{1}{2}\frac{dC}{dz}\Delta V^2 \qquad (5)$$

Where $\frac{dC}{dz}$ the capacitance gradient between the tip and the sample and ΔV is the potential difference between the V_{CPD} and an applied V_{DC} to bring the tip vibration to a minimum vibration. By inserting equation 4 into 5, we get

$$F = \frac{1}{2}\frac{dC}{dz}[(V_{DC} - V_{CPD}) + V_{AC} \,.\, \sin(\omega t)]^2 \qquad (6)$$

The above equation is divided into three parts F_{DC}, F_{ω} and $F_{2\omega}$. Here, FDC is used for the topographical signal, F_{ω} is used to measure the contact potential signal between the tip and the sample and $F_{2\omega}$ is used for the capacitance microscopy.

2.6 Tip Enhanced Raman Spectroscopy

Tip enhanced Raman spectroscopy is a technique where the local surface plasmons of sharp metal coated nano-tip are utilized to enhance and confine the EM field near the tip surface, which is further used to enhance the Raman scattering signal emanating from the nanoscale volume of the sample in use. This technique is very effective to generate Raman images with a very high spatially resolution of the order of 20-30nm by scanning the sample surface with a nano-tip.

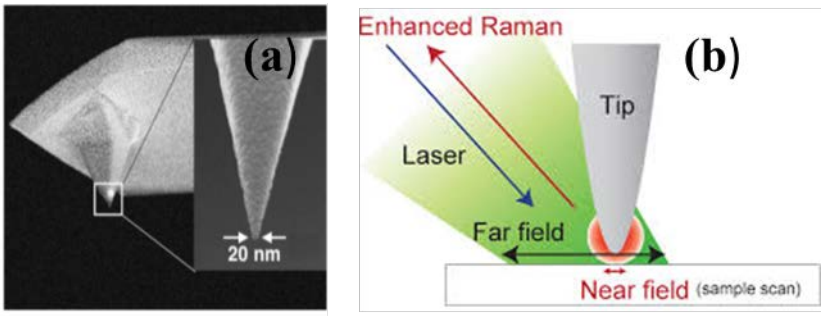

Figure 2-7: (a) TERS gold tip, (b) illustration of TERS mechanism

Out of the three SPM (scanning probe microscopy) based TERS, here I will discuss the STM (scanning tunning microscope) based TERS. In this system, a sample is inserted between a gold substrate and gold tip, therefore, reflection mode is utilized with a side illumination and a side collection of Raman signal. The proximity of gold tip to the substrate creates like a metallic nanogap due to surface plasmons resonance after excited by the incident visible light source and it further enhances the EM field (or near field) in the vicinity of the gold tip apex. Therefore, this near field enhances the Raman scattering signal coming from the sample by a factor of 10^3-10^6 and scan the sample with a high spatial resolution[40].

CHAPTER 3.
MOS_2 MONOLAYERS GROWTH ON SAPPHIRE

3.1 Experimental

Chemical vapor deposition is a very versatile and well-known technique because of its simple operation and high-quality growth of various nanomaterials and thin films from atomic size dimensions to sub-microns size. In the CVD growth, a precursor in a powder, liquid or gaseous state, has been vaporized at a very high temperature and carry the vapors downstream with either argon or nitrogen inert carrier gas followed by the deposition of vapors on the growth substrate at lower temperature.

Among many factors, the following parameters which greatly influence the growth of MoS_2 monolayers are [41, 42, 43, 44].

1. Type of the precursor used
2. Evaporation temperature of the precursor
3. Growth temperature on the substrate
4. Evaporation time
5. Pressure at which growth occurs

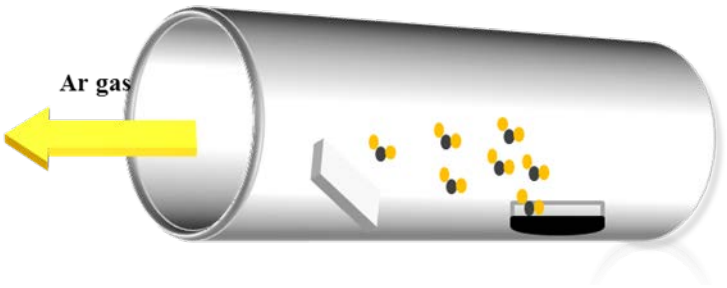

Figure 3-1.CVD setup

In the current growth mechanism, large area MoS_2 nanoflakes were grown at various growth temperatures (700°C, 750°C, 770°C, 800°C) in the low pressure chemical vapor deposition (LPCVD) fitted with a quartz tube in a 3 zone furnaces (LINDBERG/BLUE) and had studied the morphology and size of as deposited flakes.

Prior to the growth, (0001) Sapphire substrate was cleaned using acetone solution followed by IPA. The High purity MoS_2 powder precursor (Alfa Aesar) was placed in a quartz boat at the center of a quartz tube. The sapphire substrate was placed downstream at a distance of ~10cm from the position of precursor. The growth at various growth temperatures as mentioned in Table 2 was performed at a pressure of 10 mbar under 20 sccm Ar flow, with the furnace temperature ramped to set temperature with a heating rate of 20.8°C/min, and hold at that set furnace temperature for a duration of 20 min. Afterwards, the furnace was allowed to cool down naturally. The Table of growth temperature vs domain size is mentioned below:

Table 2: Growth temperature vs. MoS_2 domain size

Growth Temp.	700°C	750°C	770°C	800°C
Size (µm)	0.204	3-5	6-7	70-97

3.2 Results and Discussion of as Grown MoS_2 Flakes

3.2.1 Scanning Electron Microscopy

The morphology of the grown MoS_2 flakes has been studied by scanning electron microscope as shown in Figure 3-2. As the SEM images exhibit, the MoS_2 triangles domain size is deeply affected by the growth temperature. Notably, at the growth temperature ~700°C, the triangular MoS_2 flakes are of uniform edge length of ~200nm. Upon increasing the growth temperature to 750°C, the edge length of obtained MoS_2 flakes enlarged to 3-5 µm. Further increase the growth temperature to 770°C while keeping all other parameters remains constant, the edge length increased to 6-7µm. These obtained results show that with the rise of growth temperature, the edge length of MoS_2 flakes increased. This is due to the rise in temperature, which causes more precursor dissociate into Mo and S atoms, which further enhances the vapor pressure of Mo and S on the substrate. Thus, upon increasing the growth temperature to 800°C, the size drastically raised to ~70-96µm explicitly shown in Figure 3-2.

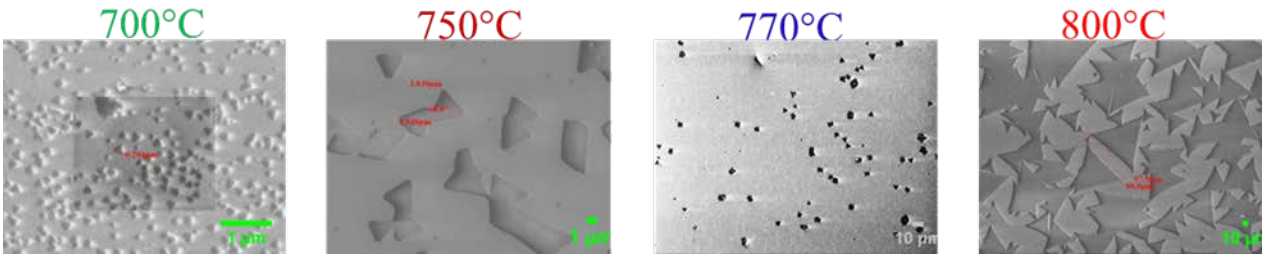

Figure 3-2. SEM analysis of MoS_2 flake size grown at different growth temperatures

3.2.2 Micro-Raman and Optical Characterization

Raman spectroscopy is a non-destructive tool and was used to make sure the obtained flakes on sapphire substrates are indeed MoS_2 monolayers. MoS_2 monolayers has two characteristic Raman modes of vibration named as E^1_{2g} mode due to in-plane vibration of Mo and S atoms and A_{1g} mode due to out-of-plane vibration of two sulfur atoms. On our CVD grown monolayers,

Raman modes occur at positions 385.5 cm^{-1} (E^1_{2g}) and at 405.7 cm^{-1} (A_{1g}) as shown in Figure 3-3. As can be seen, the peak positions display the same peaks at all samples grown at different temperatures except at 700°C (200 nm sized MoS_2 flakes were too small to generate any Raman peak) because the flakes were too small for the laser beam to focus on. The obtained peak frequency difference between two Raman modes is 20.2 cm^{-1} and is independent of growth temperature and this matches well with the CVD growth MoS_2 monolayers[43,44], which manifests the growth of monolayer form of MoS_2 crystals. In addition, to reveal the dependency of layered MoS_2 on thickness, the Raman vibrational modes of monolayer have been compared with the bulk MoS_2 from which gives the characteristics Raman peaks at 381.6cm^{-1} (E^1_{2g}) and 406.8 cm^{-1} (A_{1g}) with a peak separation ~25.2cm^{-1} as shown in Figure 3-3.

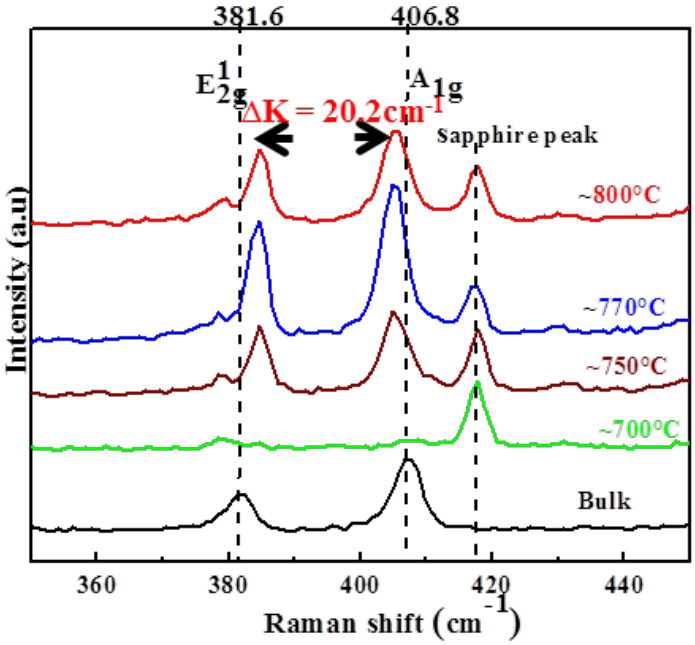

Figure 3-3. Raman Spectra of MoS_2 grown at different temperatures.

Moreover, luminescence study is another inevitable tool to investigate the optical nature of thin MoS_2 flakes. Figure 3-4 illustrates the typical PL spectra of as obtained MoS_2 flakes on all the samples grown at different temperatures. For the samples grown above 750°C, two PL peaks

were observed, one at 1.86-1.87 eV, which is called A-exciton peak, and another small intensity peak called B exciton peak at 2.01-2.02eV. These two A and B exciton peaks are direct bandgap optical transitions and their energy difference is caused by the spin-orbit splitting of the valance band. It has been also shown that monolayer PL peak is very strong and sharp as compared with the bulk counterpart which also represents the direct bandgap nature of MoS_2 monolayers[45,46]. The extracted value of full width of half maxima (fwhm) of that MoS_2 flakes grown on sapphire substrate was ~58meV, which exhibits the highly crystalline nature of as grown MoS_2 monolayers[47,48].

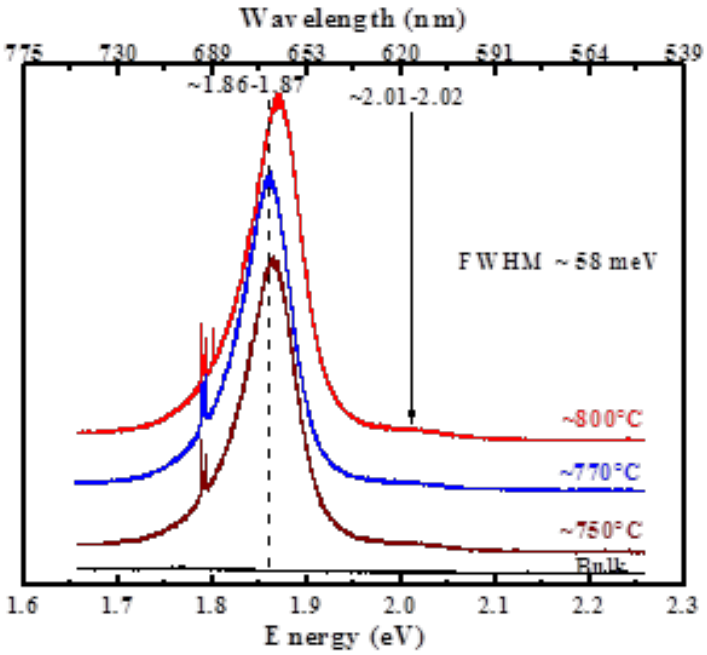

Figure 3-4. PL spectra of MoS_2 grown at different temperatures.

3.2.3 Uniformity Check of MoS_2 monolayer triangle

To obtain the uniformity of the MoS_2 triangular region, micro-Raman and luminescence spectra was taken within the marginal MoS_2 islands as shown in Figure 3-5. At the excitation wavelength of 532nm, micro-Raman spectra at all the edges and the corners of MoS_2 monolayer flake as shown in optical microscope images gives the both signature Raman modes of vibration

E^1_{2g} and A_{1g}. It can be seen that the intensity of both modes and the spacing is consistently ~20.2cm^{-1}, which shows MoS_2 triangular is homogeneously grown monolayer. In addition, the uniformity of grown triangle is evident from the PL spectra taken at the same positions. The position of the PL peak is located at 1.842eV (673.6nm) for all the regions which exhibit the uniformity of the triangle. The possibility of inhomogeneous strain in the grown flake is ruled out because Raman peaks are strain sensitive[49,50,51] and are consistent over the entire MoS_2 monolayer flake.

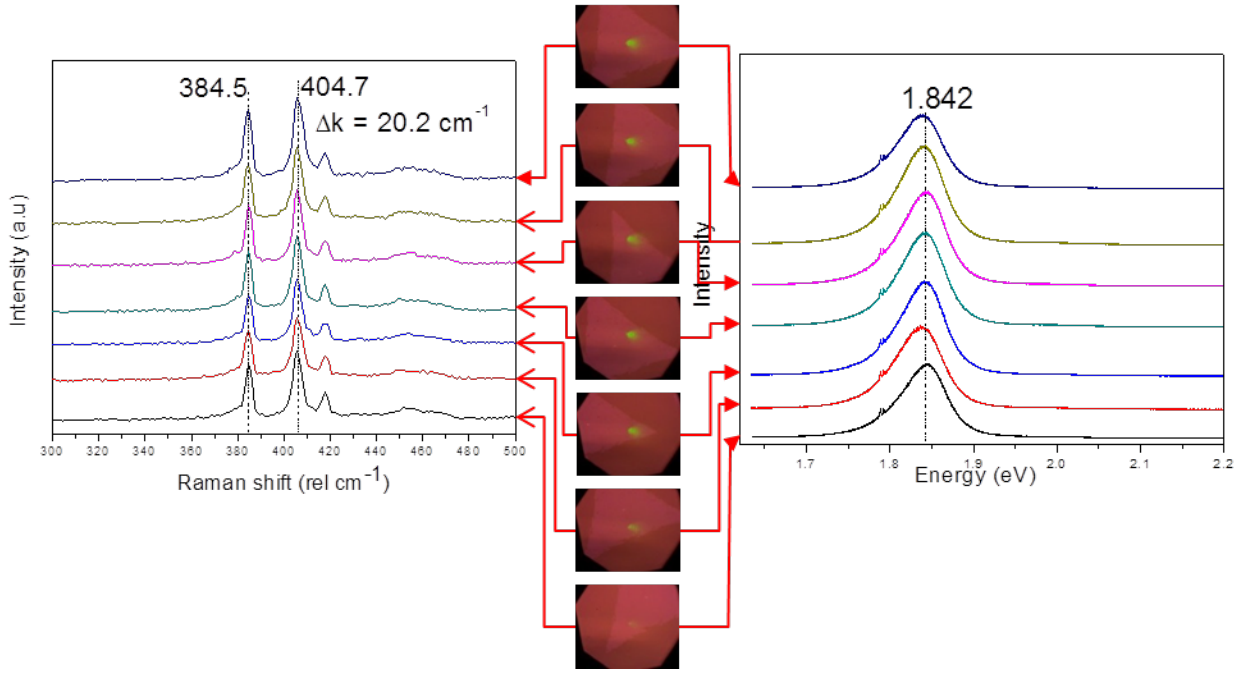

Figure 3-5.Uniformity study of as grown MoS_2 flake on sapphire substrate.

3.2.4 The Excitation Power Dependence of PL Spectra

To access the nature of radiative recombination mechanism, the study of excitation power dependence of PL spectra is usually a good indicator. Predominantly, the PL emission intensity, IPL, exhibits a dependence on the incident laser power, as IPLαP_{opt}^{α}. In this equation, the power coefficient α represents the radiative recombination mechanism, in which the value of α ~ 1-2 implies free and bound exciton recombination and α < 1 implies impurity or defect related

recombination. Figure 3-6 presents the PL spectrum dependence on the incident laser power of wavelength 532nm at room temperature. In the spectrum, a strong A exciton emission peak at 670nm and weak B exciton peak at 623nm were observed. The inset of Figure 3-6 shows the log-log plot of luminescence emission intensity with the incident laser power. The extracted value of exponent α is ~0.71, which indicates the recombination is excitonic with some contribution of defect or impurity related recombination.

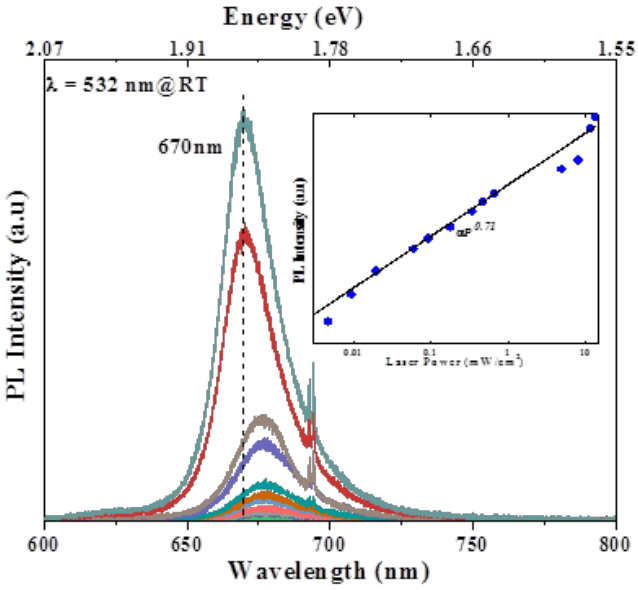

Figure 3-6. Excitation power dependence PL spectra of MoS2 monolayer, inset is the log-log plot of PL intensity vs incident laser power

3.2.5 XPS Study of as Grown Pristine MoS_2 monolayers on Sapphire Substrates

To explore the chemical composition of the pristine monolayer MoS_2 and to measure the binding energies of Mo and S, MoS_2 monolayer was probed using XPS technique. The Mo 3d core energy spectrum is presented in Figure 3-7. The positions show two peaks with a doublet at 229.875eV (Mo $3d_{5/2}$) and 233.15eV (Mo $3d_{3/2}$), respectively with a spin-orbit splitting Δ ~3.28eV and is attributed to Mo^{+4} formal oxidation state of MoS_2, whereas a minor peak is

realized at 236.72eV corresponding to MoO_x state because its Mo $3d_{3/2}$ peak occurs at ~236eV. The relatively weak signal of MoO_x peak suggests a small MoO_x content. The S^{2-} peaks, corresponding to S $2p_{3/2}$ and S $2p_{1/2}$ are observed at 162.72eV and 163.85eV. All the achieved peaks are consistent with the reported values for monolayer MoS_2 crystal[52, 53, 54]

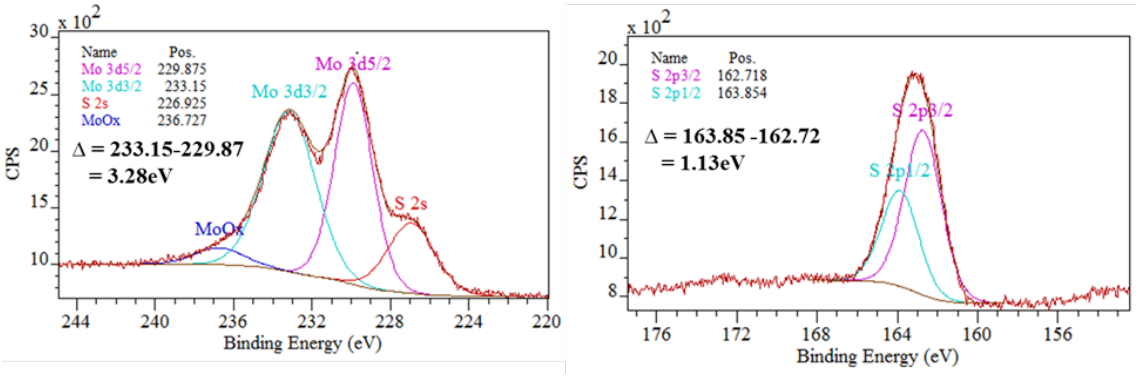

Figure 3-7. XPS spectra present the Mo and S peaks

3.2.6 Thickness Study of MoS_2 Flakes by Atomic Force Microscope

AFM characterization was performed to explore the topography and the grown MoS_2 flake thickness, and the measured thickness of MoS_2 flake is ~0.725nm as shown in Figure 3-8, which is close to three atoms thick. It proves the growth of single monolayer MoS_2 flakes. The ideal monolayer height calculated through x-ray diffractometer is ~0.615nm[55,56] and our achieved layer thickness is close to the typical value of the state-of-art values between 0.6-0.8nm[57, 58].

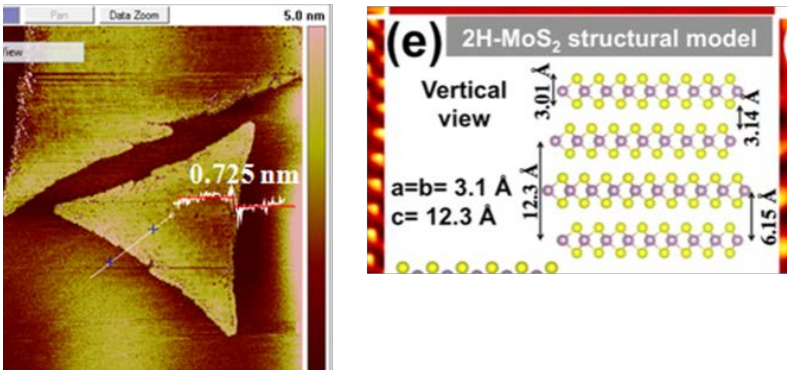

Figure 3-8.AFM characterization of CVD MoS_2 flakes

3.2.7 Temperature Dependent PL of Monolayer MoS_2 on Sapphire Substrate

Here, the focus is on the PL measurements taken at low and high temperature. These types of measurements reveal the significant impact of different temperatures on optical bandgap, which includes the positions of excitons in MoS_2 monolayers.

In this study, a PL spectrum is taken at room temperature with 532nm laser beam excitation. A monolayer MoS_2 shows free energy exciton (A-exciton) peak at 673nm (1.844eV) with an inhomogeneous broadening. However, the A-exciton PL peak at cryogenic temperature 7k and with 620nm excitation exhibit blue shift and centered at 660nm (1.88eV). This blue shift in A-exciton peak is due to the existence of strain at the interface from the different thermal expansion coefficients of sapphire and MoS_2 monolayer and as calculated blue shift is ~36meV, which is very consistent with the reported values[59,60,61]. In-addition, a broad peak (D) at 720nm (1.72eV) has been noted, which is due to bound excitons[62,63]

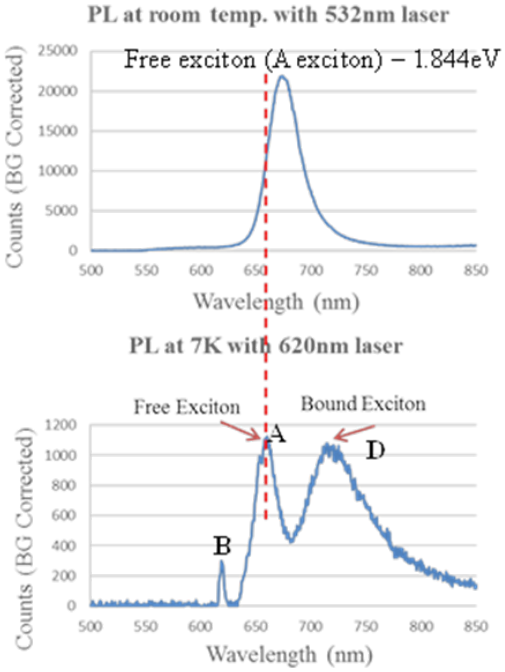

Figure 3-9.PL spectra at room and low (7k) temperature

3.2.8 Valley Selective Polarized PL of Monolayer MoS_2

Recently, these MoS_2 monolayers are realized as good candidates for the valley selective electronics. In monolayer form, due to inversion symmetry breaking the emission from the corners of the hexagonal Brillion zones K and K' of MoS_2 is degenerate energy levels but with different polarization states. This is due to the different Berry curvature and spin magnetic moments of the electrons associated with different valleys, which provide the possibility of manipulating and employ the valley degree of freedom[59,64,65]. The realization of valley selective polarization has been done by excitation of MoS_2 monolayers by circularly polarized light.

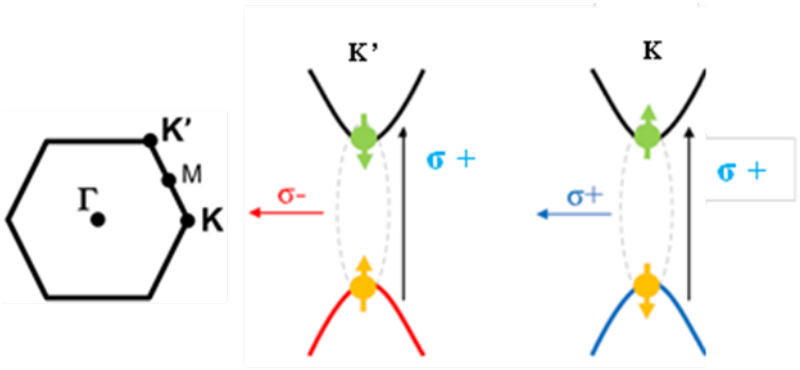

Figure 3-10.Valley selectivity by the polarized incident light

In our measurement to investigate the potential Valley selective polarization of MoS_2 monolayers on sapphire substrate, the sample at cryogenic temperature (7k) was excited with 620nm laser beam with right circulated polarization (σ+). In Figure 3-11, the spectra show the circularly polarized PL emission peak, in which K and K' are selectively excited by σ+ laser beam. It has been seen that the blue curve represents the emission peak (A exciton) from the K valley is also highly circulated right polarized (σ+) light with the same helicity as the incident light and the orange curve represents the left circularly polarized emission (σ-) light from K' valley.

To quantify our measurements, the degree of PL polarization is defined as $P = (I_+ - I_-)/(I_+ + I_-)$, Where I_+ and I_- are the helicity-resolved PL intensities from K and K' valleys. We observe P = (1100-600)/(1100+600) = 30% for the A exciton. A bound exciton state luminescence (D) was realized at 720nm, which does not exhibit polarization. The non-polarization of D peak confirms that A-exciton PL polarization is in a significant amount[66,67] and arises from valley selective excitons.

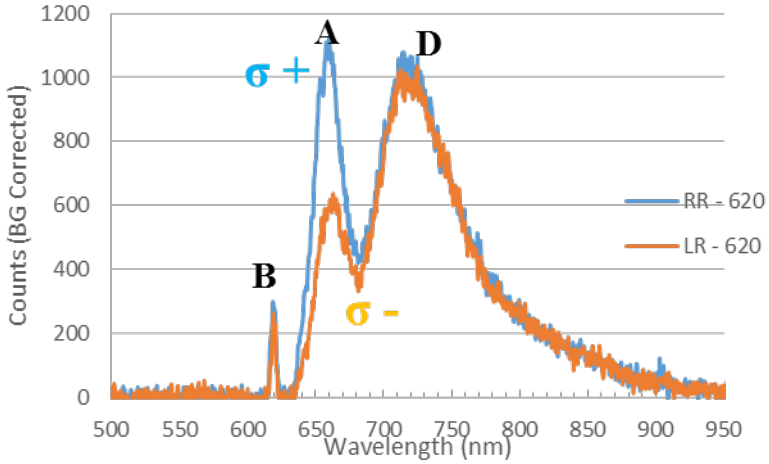

Figure 3-11.Detection of σ+ and σ- emission after illumination by σ+ excitation

CHAPTER 4.
SPECIFIC AREA GROWTH OF MOS_2 MONOLAYERS

4.1 Circular Template Formation by Microfabrication Followed by the CVD Growth of Monolayers

Specific area growth of semiconductor materials has been a goal for many industries. Despite the scalable and crystalline growth of many TMD materials, area specific growth of TMD materials is always a challenge. This is perhaps due to the lack of proper integration of TMD materials with the nanofabrication techniques that often brings contamination from photoresist and eventually results in degraded materials surface or defect introduction during fabrication. Here we have attempted to demonstrate a robust method for the specific area growth of MoS_2 monolayers using the conventional photolithography techniques. Using a 5nm thick SiO_2 layer deposited on sapphire substrate perforated on specific locations, we can localize the MoS_2 monolayers growth only to those specific areas.

4.1.1 Substrate Patterning by Microfabrication Techniques

The schematic diagram of patterning process is shown in Figure 4-1. Prior to the patterning, the standard sapphire substrate was cleaned by rinsing with acetone and isopropanol, followed by the DI water while the substrate was on spin coater. Using the e-beam deposition tool, 5nm SiO_2 was deposited on the cleaned sapphire substrate. Following the spin-casting of photoresist (S1808) onto a sapphire substrate, it was soft baked at 115°C for 60 sec. After mounting the photoresist coated

substrate on a photolithography machine, it was selectively exposed to UV beam for 3.8 sec through a designed mask with circular patterns, followed by chemically developing in a solution (MF319) to remove UV-exposed photoresist regions and to expose bare SiO_2 regions on sapphire substrate. Later, exposed bare SiO_2 regions were etched away by using buffer-oxide-etch (BOE) solution, following the removal of un-exposed photoresist and thoroughly rinsing with an acetone and isopropanol solution. The final processed sample with patterned holes is shown in Figure 4-2.

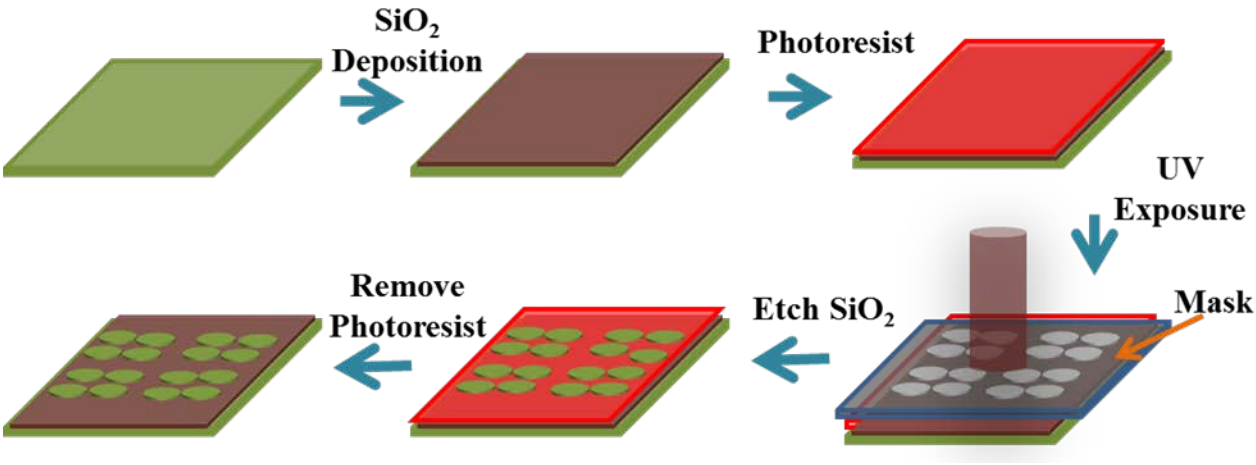

Figure 4-1. Schematic diagram process for Patterning by microfabrication

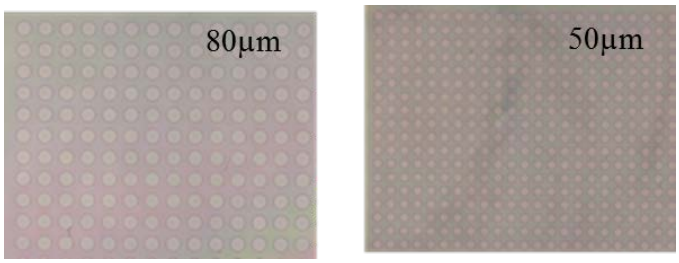

Figure 4-2. Different sized circular patterns on sapphire substrates

4.1.2 Synthesis of MoS_2 monolayers on Specific Areas

The growth mechanism for MoS_2 monolayers is identical as explained in CHAPTER 3. The chemical thermal vapor deposition of MoS_2 was carried out in a quartz tube fitted in 3 zone

furnace (LINDBERG/BLUE). In this growth, MoS_2 nanoflakes were grown at temperature (800°C).

Prior to the growth, substrate was cleaned using IPA solution. The High purity MoS_2 powder precursor (Alfa Aesar) was placed in a quartz boat at the center of a quartz tube. The substrate was placed downstream at a distance of ~10cm from the position of precursor. The growth was performed at a pressure of 10mbar under 20sccm Ar flow, with the furnace temperature ramped to 970°C with a heating rate of 20.8°C/min, and hold at 970°C furnace temperature for a duration of 20 min. Afterwards, the furnace was allowed to cool down naturally. The schematic diagram of specific area growth of MoS_2 on substrate is shown in Figure 4-3.

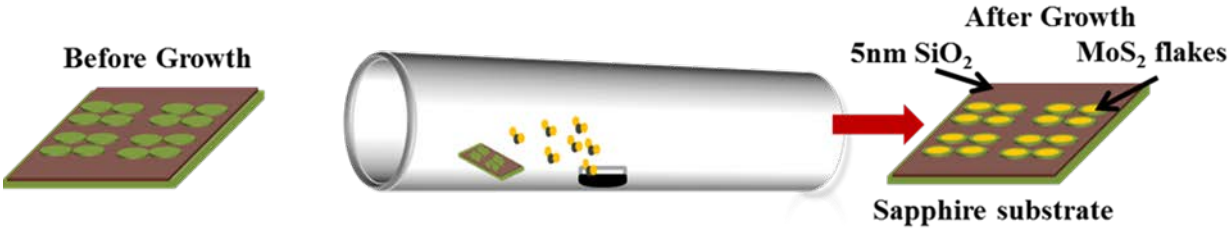

Figure 4-3.Schematic diagram of MoS_2 growth on specific areas

4.2 Results and Discussion

4.2.1 SEM Characterization of MoS_2 monolayers Grown at Specific Areas

Sapphire substrate was chosen for the study of location specific growth because of the potential to grow large area of MoS_2 with a high quality of monolayer form. A low magnification SEM image presented in Figure 4-4 shows the full patterned sapphire substrate after the CVD growth. In high magnification images in Figure 4-4, both 80µm and 50µm sized circular patterns are shown. As shown SEM images indicates a uniform growth of monolayer MoS_2 on both circular patterns with some nucleation spots. It has been noticed that the density of nucleation spots and multilayer growth of MoS_2 is more on 50µm sized circular patterns then the 80µm. This may be

because the growth conditions were not optimized for 50µm sized circular pattern or may be due to high vapor pressure of Mo and S atoms over a small sized 50µm patterns, and results in the growth of some multilayer MoS_2.

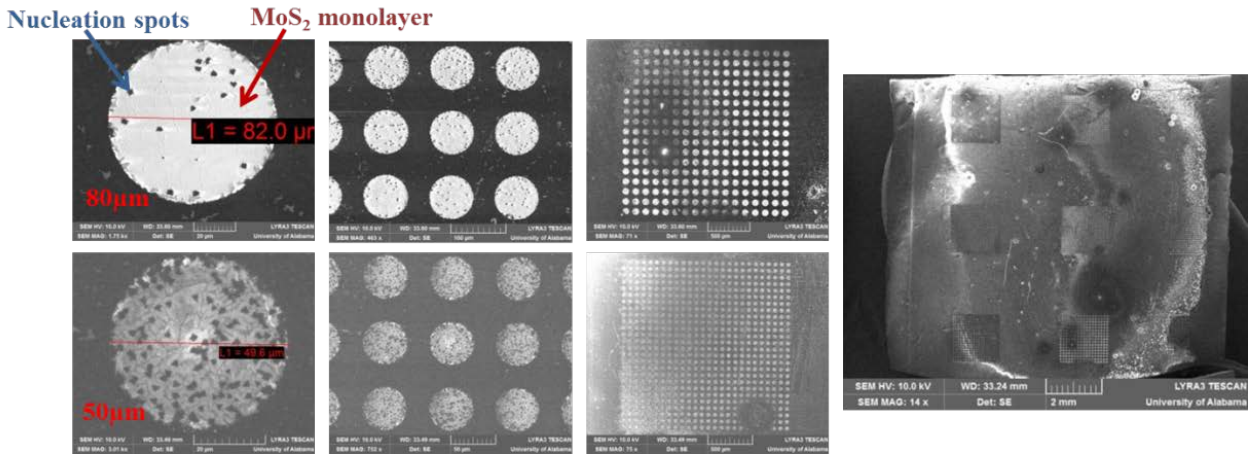

Figure 4-4.SEM images of grown MoS2 flakes on specific locations

4.2.2 Structural and Luminescence Study of Grown MoS_2 Monolayers

To provide the evidence of growth of monolayers at specific areas, Raman and photoluminescence characterization was performed on circular patterns of size 80µm and 50µm. In the inset of Figure 4-5 and Figure 4-6, optical image has been shown of the as grown monolayers. MoS_2 Raman modes of vibrations in both the circular patterns are at 384cm^{-1} and 405.7cm^{-1} exhibit the growth of monolayers. In addition, PL characterization in inset of Figure 4-5 and Figure 4-6 also provide the evidence of growth of MoS_2 monolayers. However, growth of some multilayer flakes on top of monolayer has been observed in the optical images of MoS_2 growth at 50µm, which may be due to not optimized growth conditions for 50µm circular pattern.

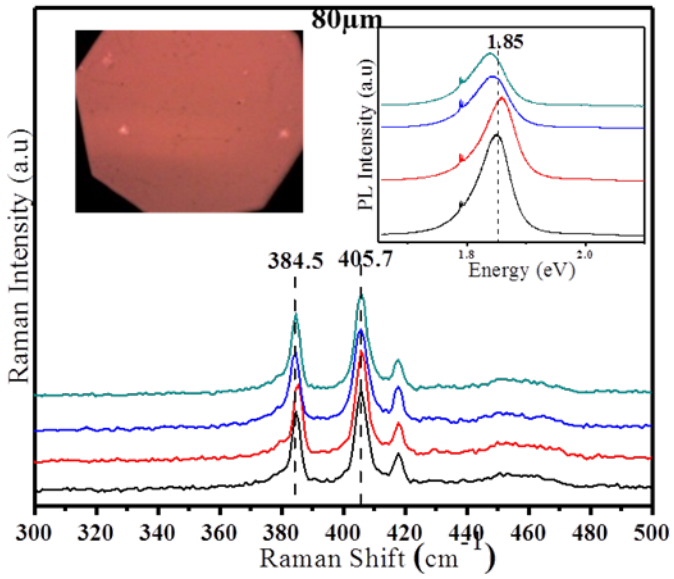

Figure 4-5. Raman and PL spectra at 80µm patterned and inset is OM image

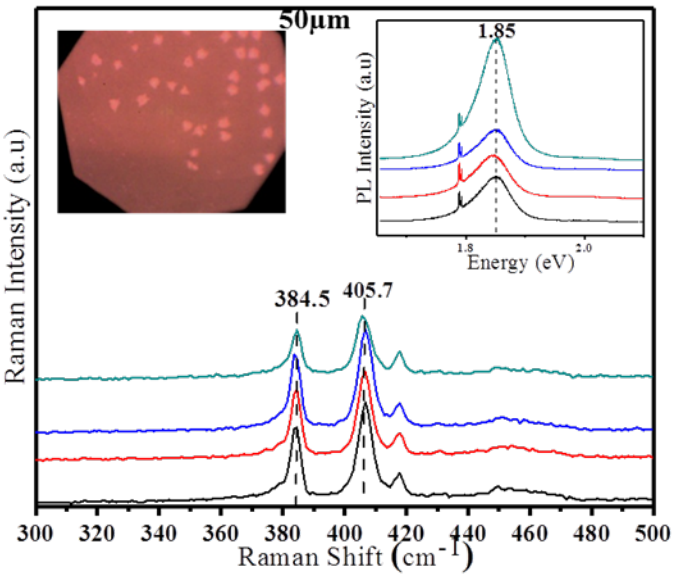

Figure 4-6. Raman and PL spectra at 50µm patterned and inset is OM image

CHAPTER 5.
MOS_2 MONOLAYERS GROWN ON SIO_2/SI SUBSTRATES

5.1 Experiment

Prior to the CVD growth of MoS_2, p-type silicon (100) substrates were oxidized under O_2/Ar atmosphere at 1000°C and at 1atm pressure for 60 minutes. The thickness of SiO_2 layer after the oxidation was 40nm measured by Rudolph Auto-EL III ellipsometer in a clean room at the University of Alabama (UA).

The growth conditions and method of MoS_2 monolayers are the same as explained in CHAPTER 3. However, in this growth method, SiO_2/Si substrate was used and was cleaned using acetone solution followed by IPA. The High purity MoS_2 powder precursor (Alfa Aesar) was placed in a quartz boat at the center of a quartz tube. The growth occurred at a pressure of 10 mbar under 20 sccm Ar flow, with the furnace temperature ramped to 970 °C with a heating rate of 20.8°C/min, and hold at 970°C furnace temperature for a duration of 20 min. Afterwards, the furnace was allowed to cool down naturally.

5.2 Results and Discussion

5.2.1 Morphological Characterization of MoS_2 by Scanning Electron and Optical Microscope

SEM images in Figure 5-1 represent the CVD grown MoS_2 flakes on SiO_2/Si substrate at 800°C growth temperature. It exhibits a growth of continuous large area MoS_2 monolayer of few mm^2

with a characteristic triangular flakes sized ~30-60µm at the periphery of the substrate. During the analysis, the average grain size of 2000µm^2 was achieved. In a magnified SEM image, a grain boundary can be seen (dashed as a white line) where monolayers start to coalesce and ultimately form a large continuous layer.

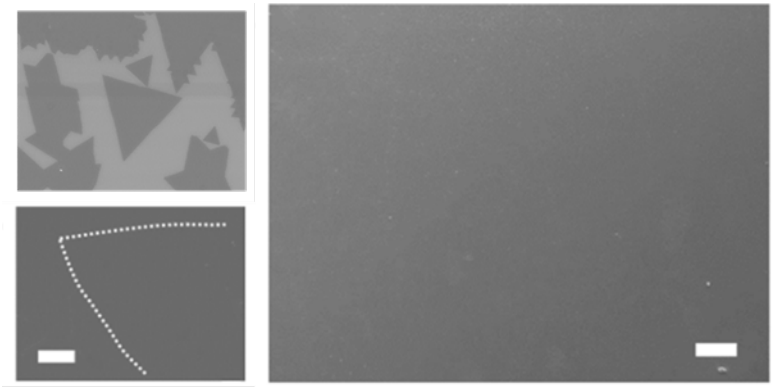

Figure 5-1.SEM images of MoS_2 monolayer flakes and thin film region (scale bar is 200µm)

The growth of bilayer/multilayer flakes with a monolayer MoS_2 is quite inevitable and to clearly distinguish between them, perhaps SEM is not the best technique due to the unclear contrast between monolayer and bilayer. Thus, an optical microscope was used and the images in Figure 5-2 distinctly manifest the monolayer MoS_2 triangular flakes with some bilayer regions.

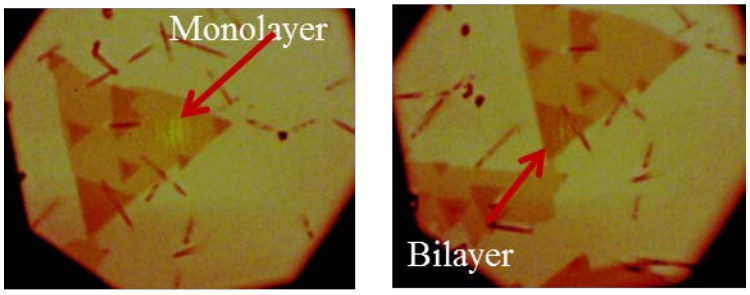

Figure 5-2.Optical images present the monolayer and bilayer MoS_2 regions

5.2.2 Micro-Raman and micro-PL Characterization

To confirm the monolayer and multilayer nature of as grown MoS_2 flakes, micro-Raman spectroscopy was implemented. As the positions of two Raman modes of vibration E^1_{2g} and A_{1g}

are characteristics of the number of MoS_2 layers[68, 69]. The Raman spectra taken over the large thin film monolayer region (marked 1L) in Figure 5-3 gives a characteristics peaks separation ~20.2cm^{-1}, bilayer region (2L) gives ~23.2cm^{-1}, trilayer (3L) ~24.2cm^{-1} and also the Raman spectra over the many layers (bulk) gives peaks separation ~25.1cm^{-1}. These achieved peak separations are very consistent with the reported values so far and confirm the growth of large area monolayer with a few bi and multilayer regions.

In the PL spectra in Figure 5-3, A-exciton (1.83eV) and B-exciton (1.99eV) two emission peaks are shown. The A-excitonic PL emission peak for monolayer (1L) is very intense at 1.83eV (680nm), which manifests the direct bandgap nature of monolayer MoS_2. However, PL peak intensity of bi and multilayer MoS_2 flakes is extremely low, which is due to its indirect bandgap nature[70, 71, 72]. Also, energy difference between the two A and B exciton peaks calculated of ~ 160 meV, which is due to valence band splitting due to spin orbit coupling.

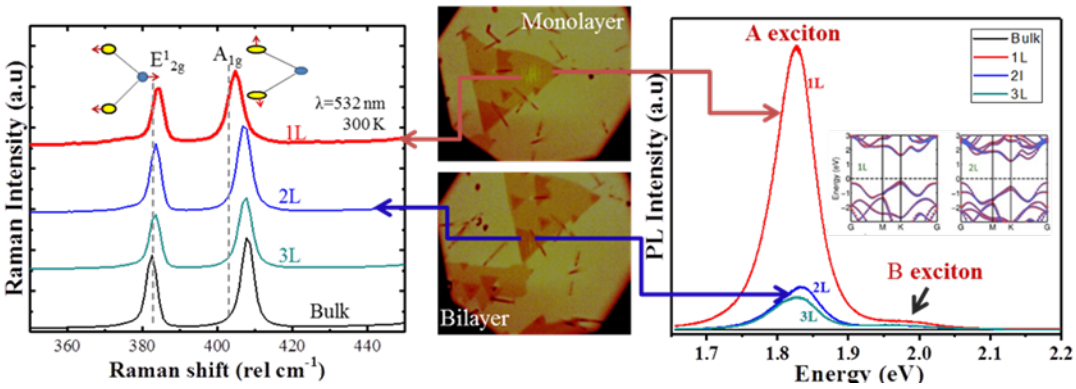

Figure 5-3. Raman and PL spectra of 1L, 2L, 3L and bulk MoS2

5.2.3 In-sights of Raman Peaks of Various MoS_2 layers thicknesses

The full width half maximum (FWHM) values of both the Raman modes of vibrations (E^1_{2g} and A_{1g}) of MoS_2 at different thicknesses are presented in Figure 5-4. It has been noted that E^1_{2g} almost remains constant and is independent of MoS_2 thickness, while A_{1g} peak FWHM increases as the MoS_2 layer thickness decreases from bulk to 2 layers. The change in A_{1g} line width may

be due to the presence of varying force constants, which leads to structural changes between inner and outer layers and varying column interactions between S atoms of neighboring layers.

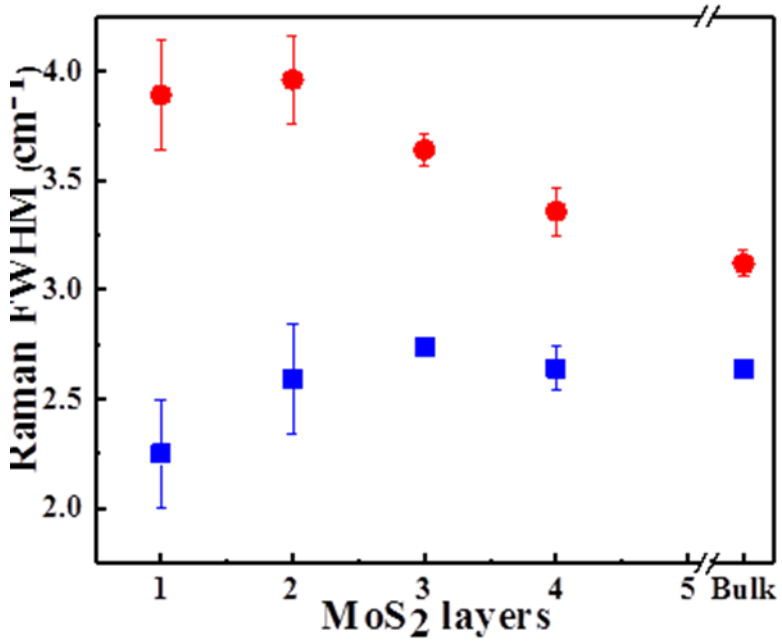

Figure 5-4.Raman FWHM vs MoS_2 layers

In Figure 5-5, MoS_2 Raman modes peak positions (E^1_{2g} and A_{1g}) for different MoS_2 layers are plotted. The behavior of Raman peaks as a function of MoS_2 layer thickness intrigues several interesting features as difference in Raman peak positions has been monotonically increasing with an increase in MoS_2 layers. Also, most strikingly, it has been noted that E^1_{2g} vibration softens, while A_{1g} vibration stiffens when MoS_2 film thickness increases. It is explained according to the reported description[73] that stiffing of A_{1g} is due to the addition of each layer to form bulk MoS_2 increase the interlayer vdw forces that results in increase in effective restoring force acting on individual atoms, while the E^1_{2g} behavior is attributable to long range coulombic interlayer vdW interactions. Thus, the difference in Raman peaks is particularly an effective thickness indicator for MoS_2 thickness.

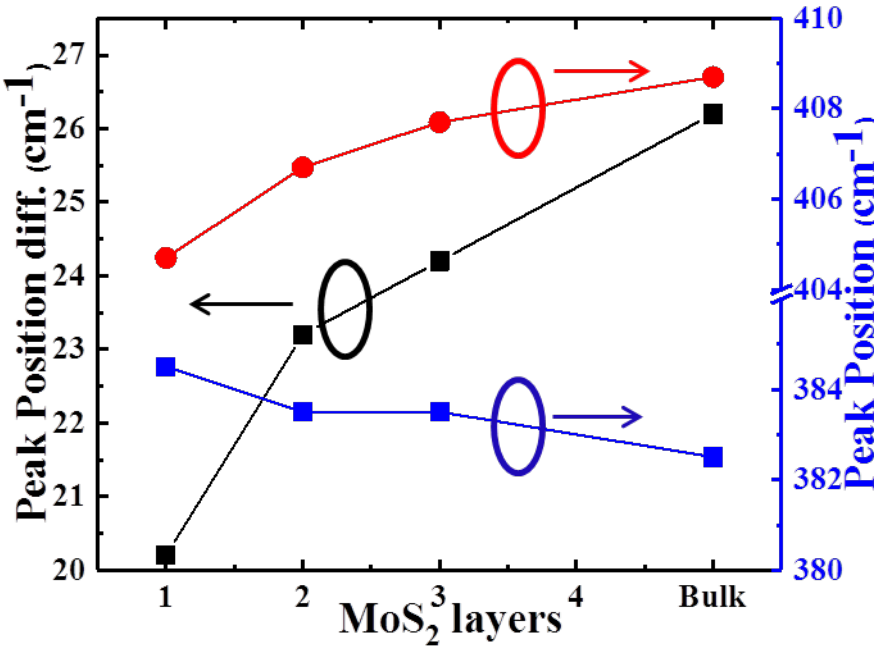

Figure 5-5. MoS_2 characteristic Raman peak positions and their difference vs MoS_2 layers

5.2.4 Importance of Thin Oxide in Electrical Devices

Since the beginning of MOSFET devices, SiO_2 has been the favorable gate insulator. Among the numerous factors, gate oxide thickness plays a vital role in determining the performance of the device. To enhance the device speed and high On/Off ratio, it is viable to use thinner gate oxide. However, gate oxide should be of substantial thickness to reduce the off current. Since the circuit speed and high On/Off ratio considerably relies on threshold voltage V_T, it is preferable to use lower threshold voltage, which depends upon the gate oxide thickness. A widely used expression of V_T and gate oxide capacitance is given as[74,75]

$$V_T = V_{FB} + 2|\varphi_p| + \frac{1}{C_{ox}}\sqrt{2\epsilon_s q N_A(2|\varphi_p| - V_{BS})} \quad (1)$$

V_{FB} is the flat band voltage, φ_p is the fermi potential, ϵ_s is the dielectric constant of silicon, N_A is the silicon doping and C_{ox} is the oxide capacitance which categorically depends on oxide thickness as, $C_{ox} = \frac{\epsilon A}{t_{ox}}$

Hence scaling down the oxide thickness consequently causes a rise in oxide capacitance and results in less threshold voltage needed for the performance of device as equation 1. Thus, the thinner oxide, raises the C_{ox} and a larger C_{ox} further enhances the I_{ds} as the below mentioned expression[76]

$$I_{ds} = \mu_s C_{ox} \frac{w_{eff}}{L_{eff}} (V_{gs} - V_T - \frac{V_{ds}}{2}) V_{ds} \quad (2)$$

Thus, thinner oxide is necessary to enhance the On/Off ratio and to maximize the circuit speed. This study exhibits that the growths of MoS_2 monolayers on thin oxide substrate plays a considerable role in high performance devices.

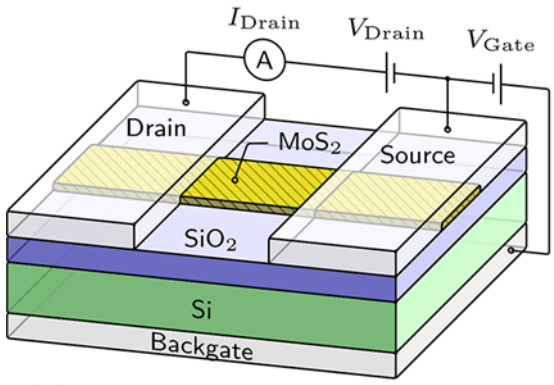

Figure 5-6.Schematic of device on SiO_2/Si substrate

5.2.5 MoS_2/SiO_2/Si with Various SiO_2 Thicknesses

To assess the crystalline quality, Raman peaks line width of MoS_2 monolayers grown on the various thicknesses of SiO_2 were studied and plotted in Figure 5-7. It has been noted that the line width for E^1_{2g} and A_{1g} was essentially independent of the oxide thickness and stays in the range of 2–2.5cm^{-1} and 3.5cm^{-1}, respectively. For comparison, the state-of-the-art FWHM of the E^1_{2g} and A_{1g} Raman peaks of CVD grown MoS_2 monolayer lays in the ranges of 3.5 – 4.2cm^{-1} and of 5–7cm^{-1} respectively[77]. Furthermore, the reported lowest FWHM of exfoliated MoS_2 monolayers from geological materials exhibits a FWHM of 2.1cm^{-1} for E^1_{2g} peak. Thus, the low

value of Raman FWHM as compared to the reported FWHM obtained may indicate that our CVD grown MoS_2 monolayers is potentially better in crystalline quality. Such good crystalline quality along with large-scale continuous monolayer MoS_2 may be attributed to a high growth temperature over ~800°C with a temperature of 970°C for the powder precursor, since the higher temperature enhances surface diffusion of ad-atoms and lateral crystal growth, and therefore, smooth coalescence into a continuous film.

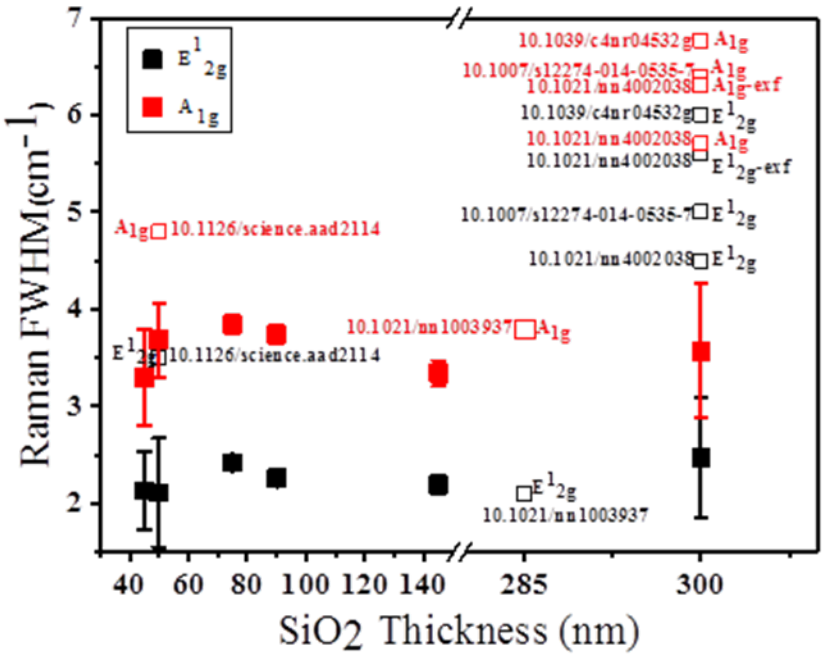

Figure 5-7. Raman peaks FWHM of 1L MoS_2 grown on differently thick SiO_2

To further explore the optical properties and crystalline quality of monolayer MoS_2 on various SiO_2 thicknesses, PL FWHM has been plotted in Figure 5-8. The achieved FWHM on different SiO_2 thickness was found to range from 60 to 80meV, which is closest to the best reported state-of-the-art values of CVD monolayer MoS_2 ~50-70meV[78,79], and 50meV is for the freely suspended MoS_2 monolayer[79], and is much narrower than the exfoliated MoS_2 monolayers ~100-150meV[79,80]. The achieved PL FWHM results indicate that our CVD grown monolayer MoS_2

samples are either of highly crystalline quality or with a clearer electrostatic environment than the exfoliated monolayers.

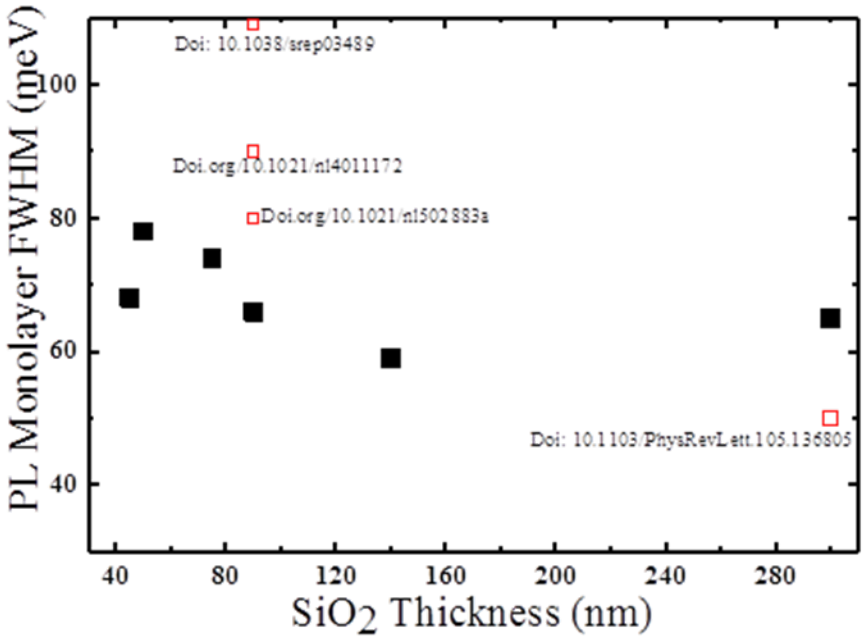

Figure 5-8. PL FWHM of 1L MoS_2 grown on differently thick SiO_2

5.2.6 The Excitation Power Dependence of PL Spectra

To assess the nature of radiative recombination mechanism, the study of excitation power dependence of PL spectra is usually a good indicator. Predominantly, the PL emission intensity, I_{PL}, exhibits a dependence on the incident laser power, as $I_{PL} \alpha P_{opt}^{\alpha}$ [81, 82]. In this equation, the power coefficient α represents the radiative recombination mechanism, in which the value of α ~ 1-2 implies free and bound exciton recombination and α < 1 implies impurity or defect related recombination. Figure 5-9 presents the PL spectrum dependence on the incident laser power of wavelength 532nm at room temperature. In the spectrum, a strong emission at 1.84eV is the A exciton peak and a weak emission at 1.99eV is the B exciton peak. The inset of Figure 5-9 shows the log-log plot of luminescence emission intensity with the incident laser power. The extracted

value of exponent α is ~0.79, which indicates the recombination is excitonic with some contribution of defect or impurity related recombination.

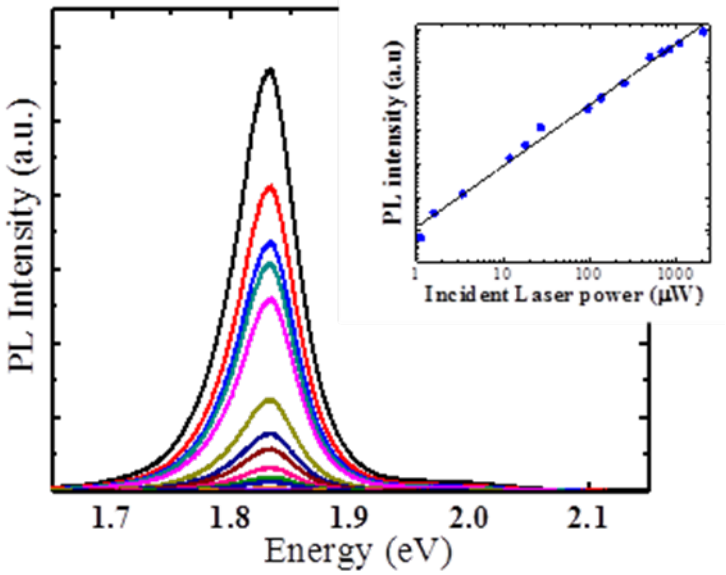

Figure 5-9. Excitation power dependence PL spectra of MoS_2 monolayer, inset is the log-log plot of PL intensity vs incident laser power

5.2.7 XPS Characterization of MoS_2 Monolayers

The chemical details of grown MoS_2 monolayers have been deduced by XPS technique by analyzing the Mo 3d and S 2p core level emission peaks. In Figure 5-10, we noticed the characteristic doublet associated with Mo^{4+}, at 229.96eV ($3d_{5/2}$) and 233.1eV ($3d_{3/2}$). The calculated energy difference between two Mo 3d peaks is ~3.12eV and it exists due to spin orbit coupling. The S 2s peak at a binding energy of 227.088 eV corresponding to MoS_2 is also observed. The reported XPS peaks of MoO_x $3d_{3/2}$ is ~236.024eV[83,84] and here the presence of an intense oxide peak is because the sample was exposed to an atmosphere for a while, so probably water vapors contaminate our pure MoS_2 monolayer. Another doublet of peaks on the right of Figure 5-10 is assigned to S^{2-} and occurs at 162.6eV ($2p_{3/2}$) and 163.8eV ($2p_{1/2}$), with a spin orbit splitting ~1.09eV.

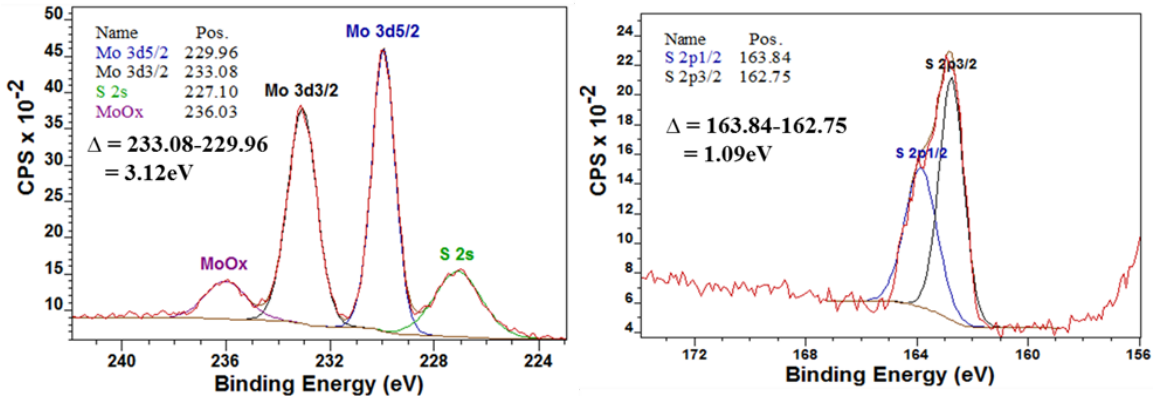

Figure 5-10.XPS analysis of Mo and S binding energies of CVD grown MoS_2

CHAPTER 6.
MOS_2 MONOLAYERS GROWN ON GALLIUM NITRIDE SUBSTRATES

6.1 Introduction

Two-dimensional semiconducting MoS_2 monolayer has been grown by CVD method but on oxide or insulating substrates. This results in lacking of crystal alignment because of not lattice matched structures. In-addition, MoS_2 monolayers growth on insulating substrates is limited to simple device fabrication structures and to realize the semiconductor-semiconductor based heterostructures, they need to be transferred on other substrates. As a result, numerous research groups made serious efforts to grow 2D materials on gallium nitride (GaN) substrate[85, 86, 87]. Lately, CVD grown MoS_2/GaN photodetector has been reported with a high responsivity and high detectivity[88]. Thus, to explore the other substrates, here we have grown MoS_2 on semiconducting GaN substrate.

Epitaxial alignment between MoS_2 and GaN is predicted to exist as both MoS_2 and GaN are related to a hexagonal crystal system with an in-plane lattice mismatching is as calculated:

$$\text{Lattice mismatch} = (3.187-3.15)/3.187 \sim 1\%$$

Close proximity of the thermal expansion coefficient of MoS_2 and GaN allow the epitaxial alignment after the growth occurs.

6.2 Experimental

To study the growth of MoS_2 monolayers, two different types of GaN substrates were used. One is GaN layer deposited on sapphire substrate by MOCVD technique and another substrate used

was pure GaN. The growth conditions and method of MoS_2 monolayers have been exactly the same as explained in CHAPTER 3. In this growth method, GaN substrates were cleaned using acetone solution followed by IPA. The High purity MoS_2 powder precursor (Alfa Aesar) was placed in a quartz boat at the center of a quartz tube. The growth occur at a pressure of 10 mbar under 20 sccm Ar flow, with the furnace temperature ramped to 970 °C with a heating rate of 20.8°C/min, and hold at 970°C furnace temperature for a duration of 20 min. Afterwards, the furnace was allowed to cool down naturally.

6.3 Results and Discussion

6.3.1 Topological Characterization by Scanning Electron Microscope

Here, the CVD growth of MoS_2 on GaN/sapphire substrate is investigated. A stack of GaN layer was deposited on c-plane sapphire (0001) substrate using MOCVD technique. The MoS_2 flakes were subsequently grown on semiconducting GaN/sapphire substrate followed by the characterization by scanning electron microscope (SEM) in Figure 6-1. The typical MoS_2 triangular domain size achieved is between 500nm-1µm with the growth of some coalesced MoS_2 monolayer region shown in Figure 6-1(c).

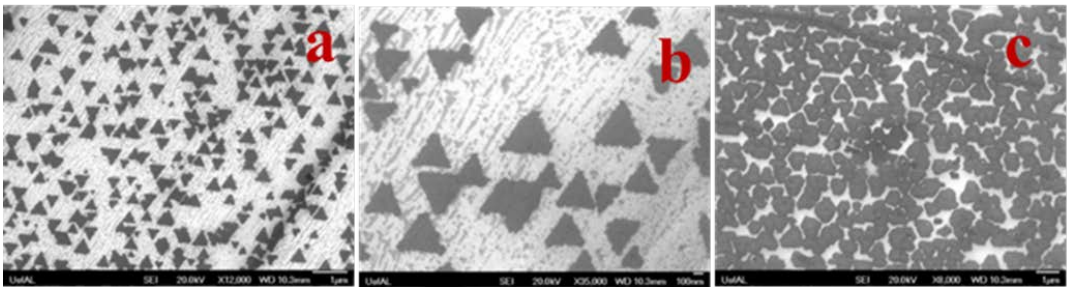

Figure 6-1.SEM images of CVD MoS_2 grown on GaN/sapphire substrate

The interesting results have been seen regarding the comparison of orientation of as grown MoS_2 triangular flakes on GaN/sapphire and bare sapphire substrates. The striking feature is that the CVD growth of MoS_2 on GaN/sapphire heterostructures are well aligned with GaN in a

hexagonal pattern as shown in Figure 6-2, however, MoS_2 triangles are not well aligned with sapphire substrate due to different lattice constants.

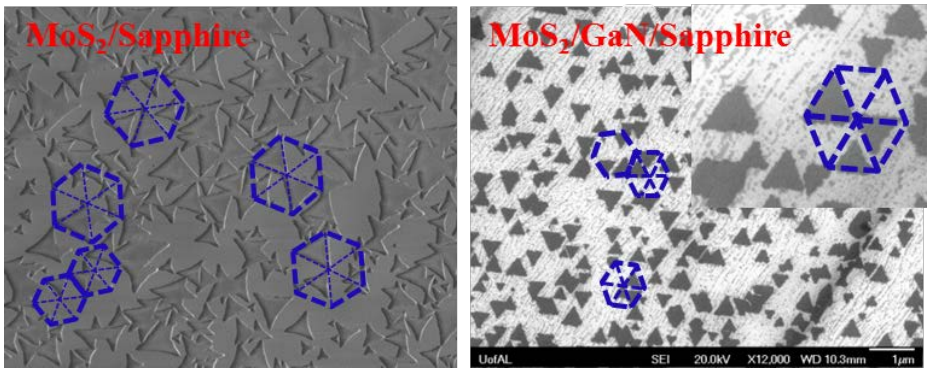

Figure 6-2.orientation of grown MoS_2 flakes on sapphire and GaN/sapphire substrates

In the growth process, pure GaN substrate was used in the CVD growth of MoS_2 flakes. Figure 6-3 shows the SEM images of MoS_2 monolayer triangles on pure GaN substrate. Typical tringles of size ~ 300nm - 1µm with some coalesced area can be seen.

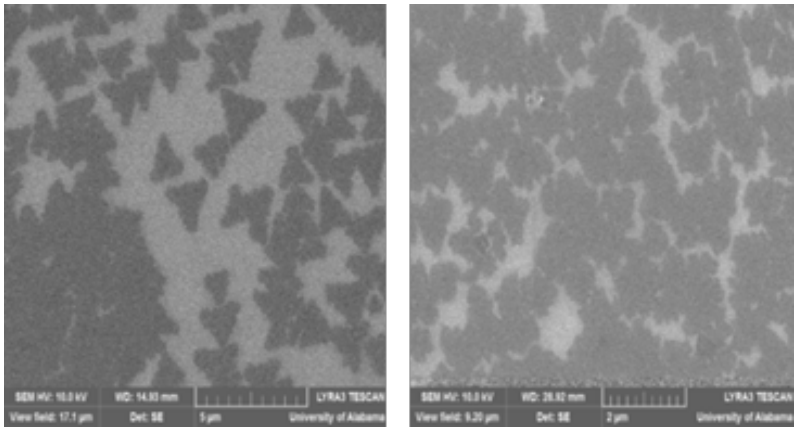

Figure 6-3.SEM images of CVD MoS_2 grown on pure GaN substrate

6.3.2 Topological Characterization by Atomic Force Microscopy

The realization of topographical measurements of MoS_2 on GaN is greatly influenced by the topography of GaN substrate. Figure 6-4 shows the AFM topography of bare GaN/sapphire substrate, which exhibits that unlike sapphire and SiO_2/Si substrates, bare GaN on sapphire substrate is not uniform and smooth. In fact, it consists of a series of terrace steps ~14nm height.

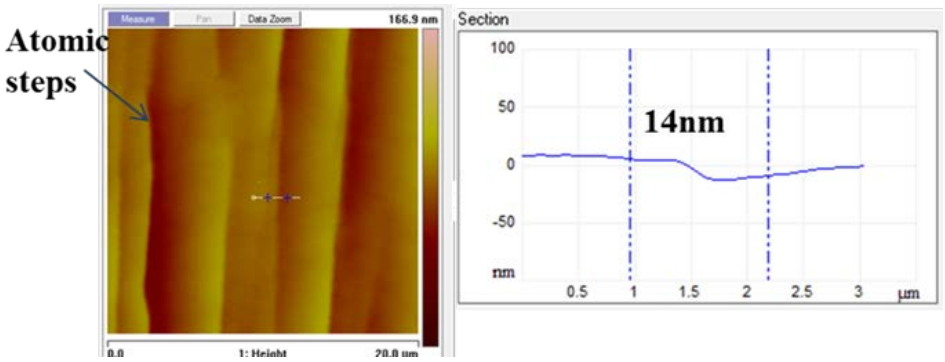

Figure 6-4.AFM topography of bare GaN/sapphire substrate

After the CVD growth of MoS_2 on terrace shaped GaN/sapphire substrate, the AFM topography is shown in Figure 6-5. It can be seen that the atomic layer thick MoS_2 monolayers on terrace shaped GaN/sapphire substrate are barely visible in height imaging, however in phase imaging, triangular flakes are visible. Visibility of MoS_2 triangles in phase imaging is due to the difference in adhesive forces, friction, viscoelasticity and variation in composition of GaN and MoS_2, which gives contrast in the tapping mode.

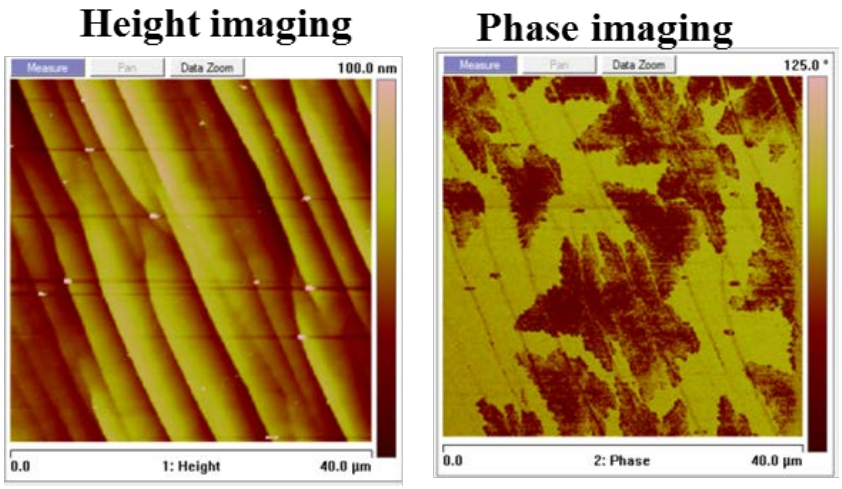

Figure 6-5.AFM analysis of CVD MOS_2 on GaN/sapphire substrate in height and phase imaging

In another study of CVD grown MoS_2 on GaN, pure GaN substrate was used. It has been seen that unlike GaN/sapphire substrate, bare GaN substrate is without any terrace steps as shown in Figure 6-6.

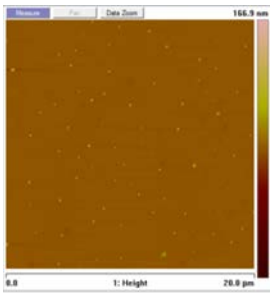

Figure 6-6.AFM topography of bare GaN substrate

However, non-existence of steps on GaN substrate did not make any difference in the CVD growth of MoS_2. As visible in Figure 6-7, the step height of MoS_2 monolayer is also indistinguishable in height imaging. However, in phase imaging, triangular flakes are clearly visible. Unable to capture the step height of MoS_2 monolayer on flat GaN substrate raises a question if MoS_2 is embedded inside GaN during growth, but no clear explanation has been found yet.

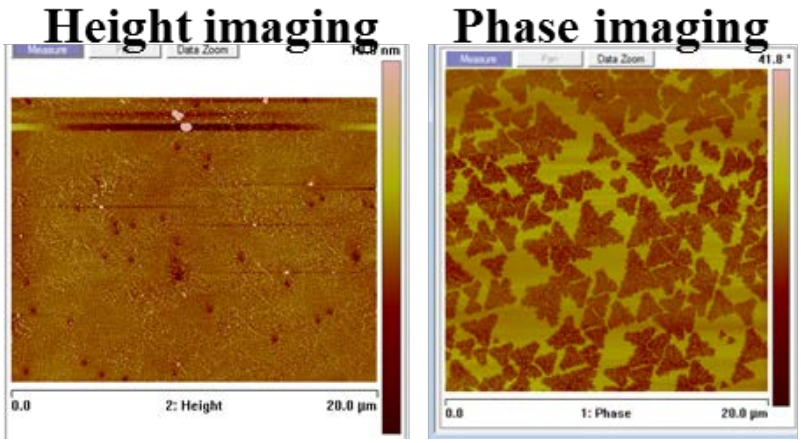

Figure 6-7. AFM of CVD MoS_2 on GaN substrate in height and phase imaging

6.3.3 Comparison of MoS_2 growth on GaN with Other Substrates

The comparison of grown MoS_2 on GaN with other substrates has been explored by optical characterizations. Raman modes of vibrations E^1_{2g} and A_{1g} were analyzed and are shown in Figure 6-8. It has been noted that the Raman characteristic peaks difference Δk of CVD grown MoS_2 on GaN/sapphire and GaN substrate is ~ 20-21cm^{-1} as compared to 21.5 cm^{-1} of MoS_2 on

Si/SiO_2 substrate. This small decrease in Δk may be due to less strain in as grown MoS_2 on GaN substrates, this interpretation is supported by the decrease in Δk of transferred MoS_2 monolayers on GaN/sapphire substrate (18.8 cm^{-1}), which is close to strain free exfoliated MoS_2 monolayer[73].

In another optical characterization, PL peaks of MoS_2/GaN monolayers have been compared with the MoS_2 on Si/SiO_2 substrate. As shown on the right of Figure 6-8, PL peaks called A and B exciton peaks of CVD grown MoS_2 on GaN/sapphire and GaN substrate is 675nm (1.837eV) and 617.5nm (2.01eV), which is the same as PL peak of MoS_2 on Si/SiO_2 substrate. This confirms that the growth of MoS_2 on GaN is of monolayer nature.

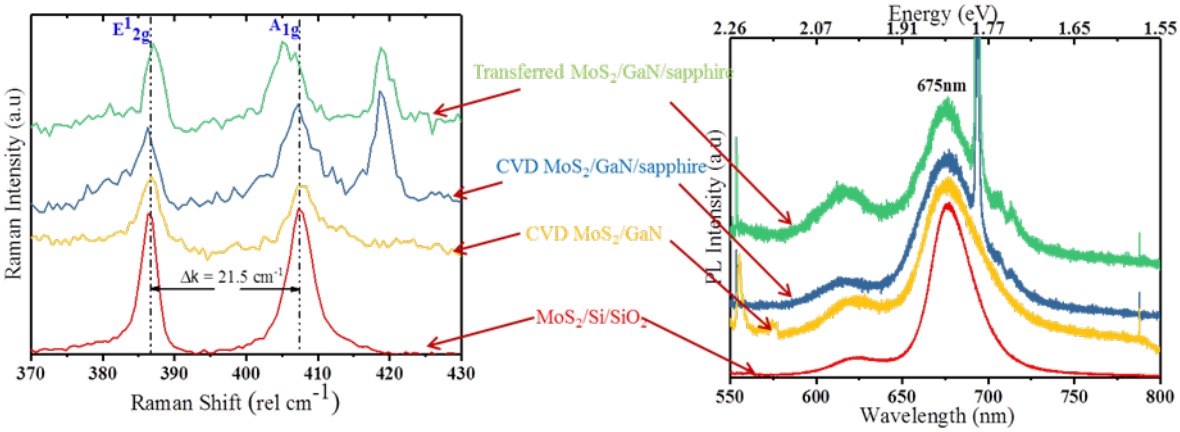

Figure 6-8.Raman and PL characterization of MoS_2 monolayer on GaN

6.3.4 XPS Analysis of as Grown MoS_2 on GaN Substrate

The chemical details of grown MoS_2 monolayers were deduced by XPS technique by analyzing the Mo 3d and S 2p core level emission peaks. The spectra on the left in Figure 6-9 has the characteristic doublet associated with Mo^{4+}, at 228.94 eV ($3d_{5/2}$) and 232.23 eV ($3d_{3/2}$) accompanied by the S 2s signal at 226eV consisting also only of one species. The calculated energy difference between two Mo 3d peaks is ~3.29eV and it exists due to spin orbit coupling. MoO_x $3d_{3/2}$ peak has been observed at 235.42eV, which is due to the aging effect on MoS_2/GaN sample which was exposed to atmosphere for a while. Similarly, spectra on the right presents the

Sulphur 2p doublet peaks consists of a species with a BE of S $2p_{3/2}$ at 160.43eV and S $2p_{1/2}$ at 162.31eV. Also Ga 3s (GaN) core level BE is also observed at 159.96eV peak has been noted which comes from GaN substrate.

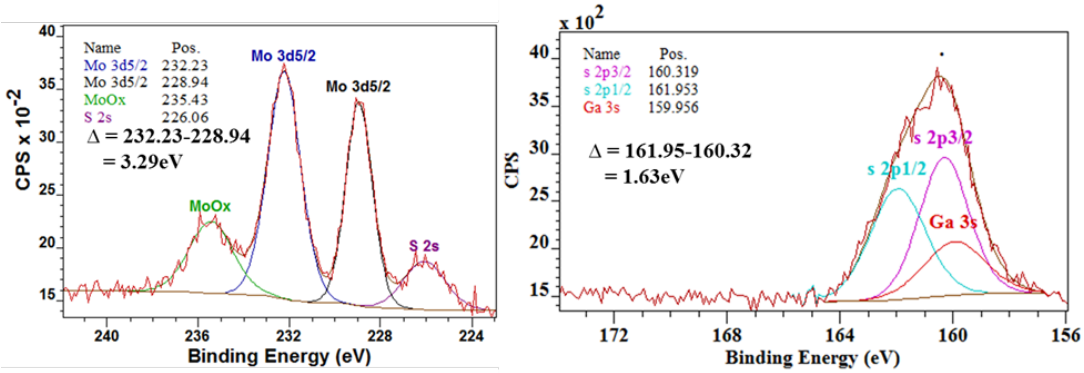

Figure 6-9.XPS comparison of MoS_2 on GaN substrate

CHAPTER 7.
MOS_2 MONOLAYERS GROWN ON GA_2O_3 SUBSTRATES

7.1 Introduction

The growth substrate and the respective dielectric constant used for MoS_2 growth are extremely important as it can introduce two possible effects in MoS_2: the lattice mismatch with MoS_2 can cause strain[89] and charge carrier transfer to MoS_2, which depends upon the scattering of excitons at the MoS_2/substrate interface[90]. After many attempts by different research groups, 2D MoS_2 monolayers on many different substrates primarily on flexible polyimide substrate[91], glassy carbon[92], Mica[93], and semiconducting GaN have been achieved successfully. However, the as grown semiconducting 2D MoS_2 monolayers on novel oxide materials (Ga_2O_3) intrigue the great interest for the advantage of both the high dielectric constant substrate and the semiconducting ultrathin MoS_2 in terms of hybrid insulator-semiconductor heterostructure electronic devices. The key component for the efficient hybrid devices is the high efficiency power conversion ability for energy saving in the future. Among the other semiconducting templates to grow 2D MoS_2 monolayers, Ga_2O_3 is an emerging promising candidate for future power conversion material, because of its excellent properties and appropriateness for mass production.

7.2 Experimental

The MoS_2 monolayers growth had been carried out by CVD process in a three zone furnace. In a typical run, prior to the growth, the growth substrates 50mm thick Ga_2O_3 on sapphire (annealed

and un-annealed) were cleaned using acetone solution followed by IPA. The chemical thermal vapor deposition of MoS_2 was carried in a 1" quartz tube fitted in 3 zone furnace (LINDBERG/BLUE). The high purity MoS_2 powder precursor (Alfa Aesar) was placed in a quartz boat at the center of a quartz tube. The sapphire substrates were placed downstream at a distance of ~10 cm from the position of precursor. Before the growth, the whole quartz tube was purged with the Ar gas repeatedly to remove the oxygen contamination. The growth was performed at a low pressure of 10 mbar under 20 sccm Ar flow, with the MoS_2 powder vaporization temperature ramped to 970 °C with a heating rate of 20.8°C/min, and hold at 970°C for a duration of 20 min. Afterwards, the furnace was allowed to cool down naturally.

7.3 Results and Discussion

7.3.1 Topography Study of MoS_2/Ga_2O_3/Sapphire Sample

The topography and thickness of as grown MoS_2 flakes on different substrates (c-plane sapphire, annealed and un-annealed Ga_2O_3) were analyzed by optical microscope and atomic force microscope. As the optical images presents the MoS_2 triangular flakes of size ~30-60µm and large thin film area on sapphire, however on annealed/un-annealed Ga_2O_3 substrate, the triangular flakes size were small ~10-20µm and did not have a large area of thin film MoS_2 comparatively to the MoS2 on bare sapphire substrate. AFM was conducted on all the substrates for the topography study and to determine the thickness of MoS_2, as shown in Figure 7-1, which yields the thickness of MoS_2 ~0.860nm on sapphire, 0.720nm on annealed Ga_2O_3/sapphire and 0.730nm on un-annealed Ga_2O_3/sapphire substrates, which is very close to the monolayer thick MoS_2[8,94,95]. The as measured surface roughness by AFM reveals that the MoS_2 monolayers mostly had similar rms roughness: 0.119 nm, 0.236 nm, and 0.189 nm on sapphire, annealed and un-annealed Ga_2O_3, respectively, which shows very smooth deposition of MoS_2 monolayers[96,97] on all the three substrates.

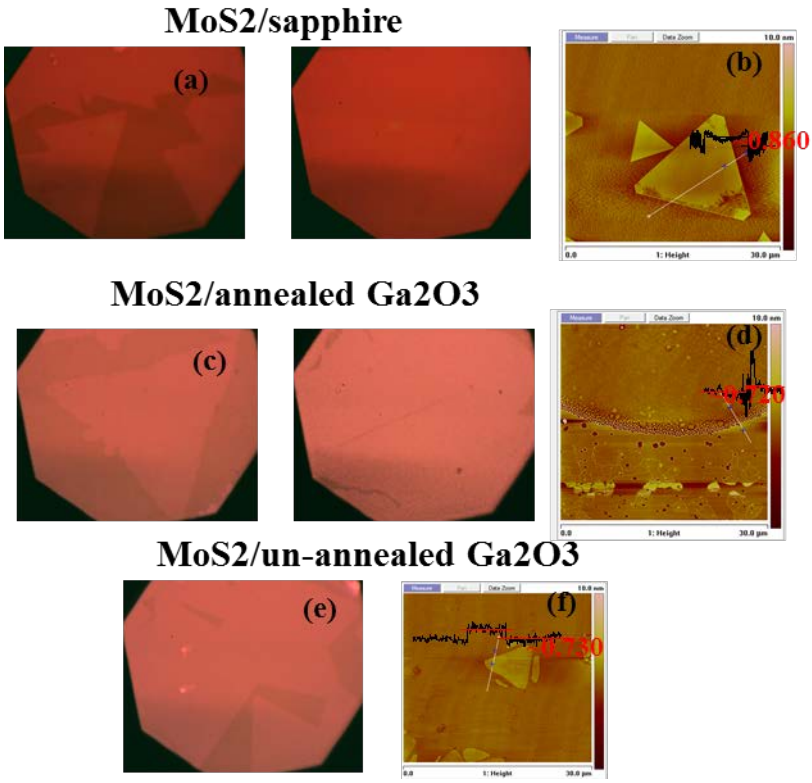

Figure 7-1.Optical and atomic force microscope images of MoS2 monolayers on sapphire, annealed Ga2O3 and un-annealed Ga2O3 substrates

7.3.2 Comparison of Raman Spectra of MoS_2/Ga_2O_3 with Other Substrates

Since the Raman analysis has become an imperative tool, it is used to distinguish between the monolayer and multilayer MoS_2. In this section, micro-Raman characterization on the as grown MoS_2 flakes was done and the comparison of the Raman spectra of MoS_2 monolayers is shown in Figure 7-2. The Raman modes of vibrations, in-plane E^1_{2g} and out-of-plane A_{1g} of monolayer MoS_2 on different substrates are easily noticeable. It has been observed that on transferred MoS_2 on ITO and GaN/sapphire substrates, Raman peaks separation $\Delta k \sim 18.7 cm^{-1}$. However, the E^1_{2g} Raman mode is blue shifted on annealed Ga_2O_3 ($\Delta k = 20 cm^{-1}$) as compared to sapphire and SiO_2/Si substrates ($\Delta k = 21 cm^{-1}$). The lower Raman FWHM of MoS_2 monolayer on Ga_2O_3 compared to other substrates corresponds to high crystallinity in nature. This shift in Raman peak

positions is attributed to the origin of strain in MoS_2 monolayers due to different lattice constant and thermal expansion coefficients of the substrates.

Strain in the grown thin film is given as, Strain = $\frac{a_{MoS2/substrate}(RT) - a_{MoS2}(RT)}{a_{MoS2}(RT)}$, where $a_{MoS2/substrate}$ is the lattice constant of the TMD grown on substrate and a_{MoS2} is the lattice constant of the unstrained TMD.

Assuming that the TMD monolayer is constrained to follow the thermal contraction of the sapphire substrate when the sample is cooled from the growth temperature, we can write

$$\frac{a_{MoS2/substrate}(RT)}{a_{MoS2}(1073)} = \frac{a_{substrate}(RT)}{a_{substrate}(1073)}$$

So

$$\text{Strain} = \frac{a_{substrate}(RT)}{a_{substrate}(1073)} \times \frac{a_{MoS2}(1073)}{a_{MoS2}(RT)} - 1$$

The values of lattice constant at growth temperature was calculated using the formula,

$$a\ (1073k) = a(300) + \alpha \times \Delta T$$

	% Strain	Type of Strain
MoS_2/Sapphire	-0.1%	Compressive
MoS_2/GaN	-0.07%	Compressive
MoS_2/Ga_2O_3	0.04%	Tensile

Thus, very low amount of tensile strain in MoS_2 on annealed Ga_2O_3 enhances the importance of annealed Ga_2O_3 for MoS_2 growth as well as the combined heterostructures could be useful for the high power electronics.

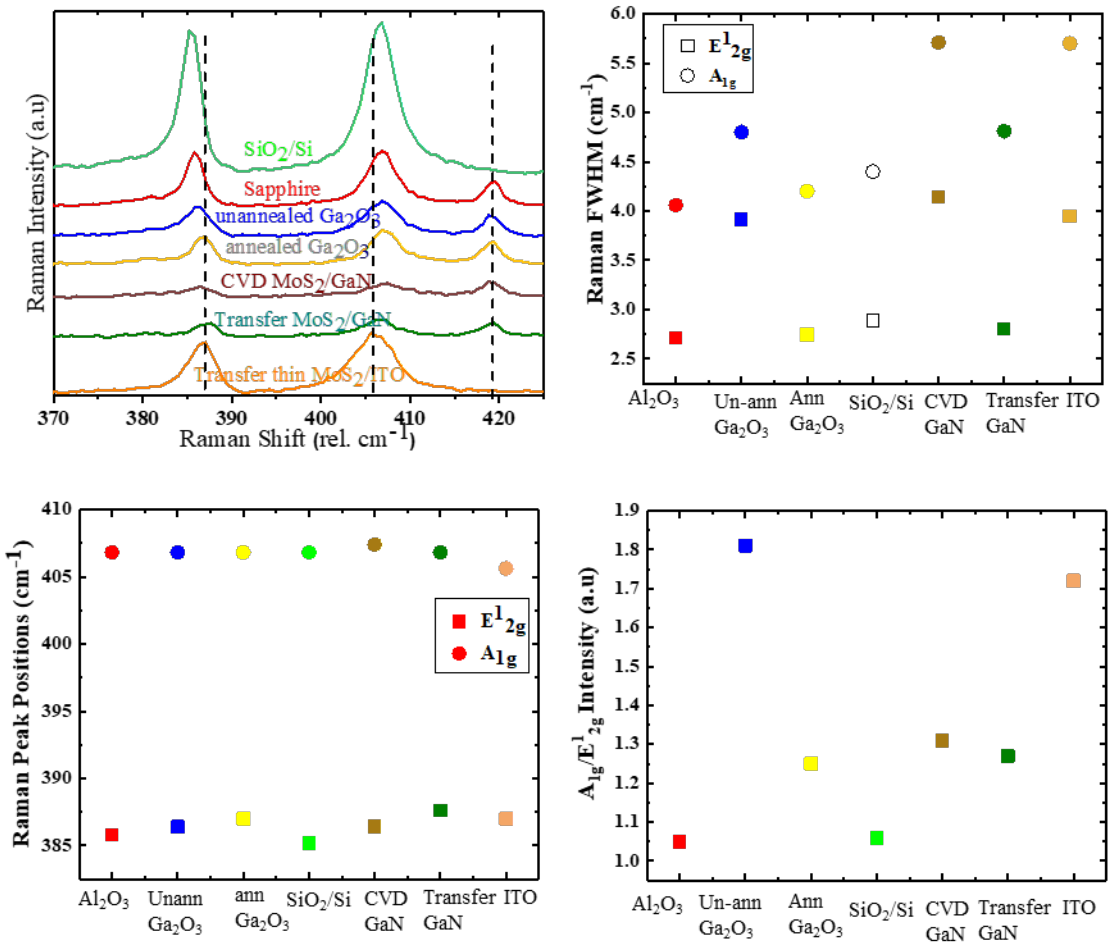

Figure 7-2.Raman analysis

7.3.3 Comparison of PL Spectra of MoS_2/Ga_2O_3 with Other Substrates

We further explored the optical characterization by measuring PL spectrum of the MoS_2 monolayers on all different substrates. In 2D materials, upon the incorporation of additional charge carriers, the neutral excitons (A°) will change into charge state, which are called trions (A^-). Due to the existence of A^-, the measured PL spectrum consists of two resonant peaks, a lower energy peak marked as A^- peak and higher energy peak called the neutral excitons A°, which is due to the very high binding energy of the neutral excitons. The kind of growth substrate thus has a significant impact on the formation of trions in MoS_2 by transferring the excess carriers in MoS_2. From Figure 7-3, we observed that the PL peak intensity enhances with

the dielectric constant of the oxide substrate. Also, the blue shift in PL peak that occurs is clearly noticeable on annealed Ga_2O_3 substrate (1.867eV) as compared to PL peak on sapphire (1.848eV), SiO_2/Si (1.837eV) and un-annealed Ga_2O_3, as shown in Figure 7-3. The fitted PL peak positions and fitted PL FWHM of A° and A^-, are shown as a function of dielectric constants of the substrates. It is noted that the trions and excitons PL (energy) peak positions blue shifted with the increase in dielectric constant of the oxide substrate. This shift can be explained by the concept of dielectric screening effect[16]. According to this effect, larger dielectric constant screens the coulomb potential of the trions and excitons, generated inside the MoS_2 monolayer and results in strong quantum confinement. Due to the large dielectric constant of annealed Ga_2O_3, which causes lesser scattering of excitons with charge impurities on the MoS_2/substrate interface and lesser the charge transfer to MoS_2 reduces the formation of trions and results in enhancement in the formation of excitons in MoS_2/annealed Ga_2O_3 substrate, contrary to the formation of trions in MoS_2/sapphire substrate. However, PL peak intensity on un-annealed Ga_2O_3 is lower in intensity, which might be due to the amorphous nature of the substrate. It was also noted that the FWHM of PL spectrum on annealed Ga_2O_3 substrate (45meV) is lowest as compared to SiO_2/Si, un-annealed Ga_2O_3 and sapphire substrates, and this FWHM value is very much close to the reported value of exfoliated MoS_2[98], which exhibits the high crystalline quality of MoS_2 flakes on annealed Ga_2O_3 substrate. Figure 7-4 exhibits the effect of oxide substrate's dielectric constant on the $\frac{I(A^-)}{I(A^0)}$ intensity ratio. As seen, with the increase of dielectric constant, the intensity ratio decreases from 1.8 to 1.2, and this is explained by the mass action model, which explains the intensity ratio as $\frac{I(A^-)}{I(A^0)} = K\,(k_{Dielectric})^{\delta} \exp\left(\frac{\varepsilon_{A^-}}{k_B T}\right)$, where K and δ are fitting parameters, ε_{A^-} is the binding energy of the trion, which is 17meV in our case. As can be seen by the dashed line, shows the fitting results and compared with the red experimental dots. The

fitting parameters extracted to be around K ~1.36 and δ ~ -0.287, and it represents the A° excitons radiative recombination rate, which changes rapidly with the dielectric constant as compared to A- recombination rate [16].

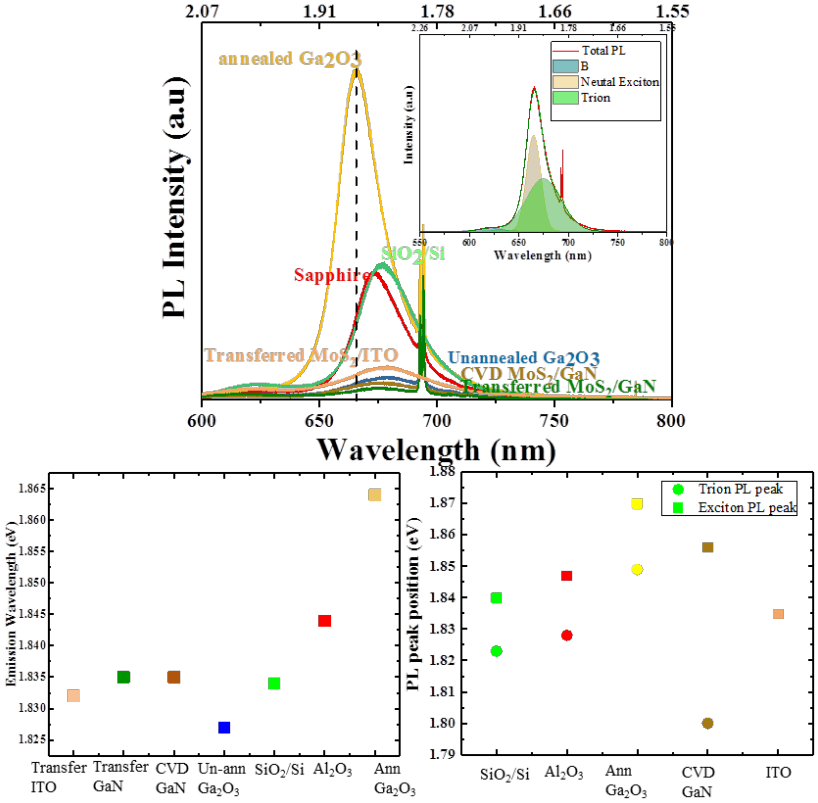

Figure 7-3.Photoluminescence spectra

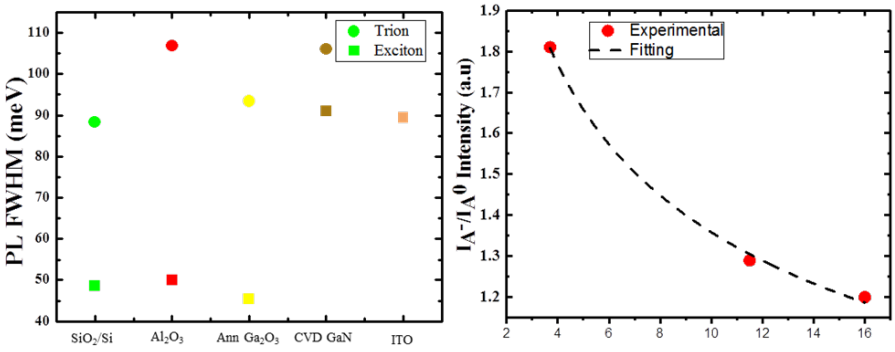

Figure 7-4.PL FWHM of trion, exciton dependence on substrate, and dependence of trion/exciton on the dielectric constant

The complete list of the properties of as-grown MoS_2 monolayers on different substrates has been exhibited in Table 3. In this table, It is clearly visible that transferred MoS_2 on any substrate has the least distance between two Raman modes of vibrations, which should be meant to be a strain free MoS_2 monolayer though we should not neglect the impact of impurities deposited from the PMMA or PDMS polymers which were used in the transfer process. In addition, blue shift of MoS_2 PL peak illustrates the impact of dielectric constant and hence, Ga_2O_3 could be a perfect substrate material to grow MoS_2 monolayers.

Table 3: Comparison chart of finding the properties of MoS_2 monolayer on different substrates

	$MoS_2/SiO_2/Si$	**MoS_2/Al_2O_3**	**MoS_2/Ga_2O_3**	**MoS_2/GaN**	**Transferred MoS_2 on GaN**
Raman peaks difference (cm^{-1})	21.6	21	19.8	20.6	19.2
AFM step height (nm)	0.740	0.725	0.730	(No step height) Seems embedded inside	---------
PL peaks position	677.5nm	673.4 nm	665.8 nm	677.5nm	675.8nm
PL intensity (counts/sec)	1600	1505	3927	210	144
Power dependent PL exponent	$\alpha = 0.79$	$\alpha = 0.71$	$\alpha = 0.61$	--------	-------
Lattice mismatch (%)	42	33.8	74	1.1	-------
Grain Size (μm^2)	468	216	141	1	-------

CHAPTER 8.
APPLICATIONS OF CVD GROWN MOS_2 MONOLAYERS

8.1 Introduction

In the previous chapters, we have successfully studied the exceptional properties exhibited by MoS_2 monolayers that make them very fascinating for optoelectronic and electrical applications. Most importantly the atomic layer thickness and direct bandgap nature of monolayers are very compatible with the CMOS industry[99], Field Effect Transistors (FETs)[100],[101] flexible electronics[102] gas sensors[103],[104] and photodetectors etc. In this chapter, the interdigitated photodetector with large area MoS_2 monolayer is fabricated and electron transport properties have been studied. In addition, gas sensing ability of as fabricated MoS_2 device was explored using CO_2 gas, in which 200ppm lowest detection limit of CO_2 gas was sensed by the device.

8.2 Fabrication of Interdigitated Device

After growth of large area MoS_2 monolayer, three steps were followed to complete the device fabrication process. The completion of device processed in three steps – in step 1- a metallic interdigitated pattern was fabricated on bare sapphire substrate, in step 2 – MoS_2 monolayers were transferred on as fabricated metallic interdigitated pattern by PMMA, in step 3 – finally, the device was completed by transferring MoS_2/interdigitated device on printed circuit board (PCB) with a wire bonding between PCB and metallic electrodes of the device. In the first step, prior to the fabrication, the substrate was thoroughly cleaned with acetone and iso-propanol. A positive

photoresist S1805 was spin coated on bare sapphire substrate for 30s. The as coated photoresist substrate was soft baked at 115°C for 60s before it was exposed to UV rays for 1.5s under a photolithography process. To develop the pattern, the substrate was dipped in MF319 developer followed by cleaning in DI water for 60s. The metallic contacts were made on the patterned sample by E-beam deposition, in which Ti/Ag metals of (20/200nm) thick were deposited and finally the device was submerged in 1165 developer to remove the excess metal by a liftoff technique. The complete process has been shown in Figure 8-1 through a schematic diagram. The device specifications are as follows: the spacing between metal electrodes is 20µm and the width of each electrode was designed to be 20µm.

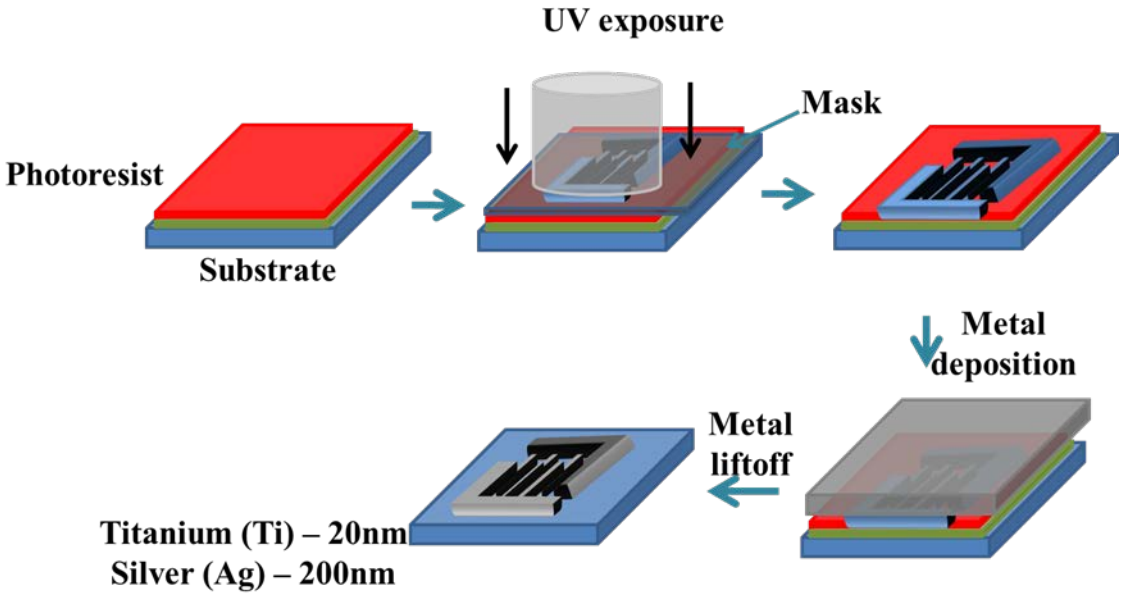

Figure 8-1. Schematic diagram of detailed experiment to fabricate interdigitated pattern

In step 2, the as grown CVD MoS_2 monolayer was transferred on the fabricated device by PMMA. The schematic illustration of the transfer process is shown in Figure 8-2. In this process, the first step involves setting the hot plate at 110°C temperature. Next, spin coat a layer of PMMA on MoS_2 covered substrate and bake it on a hotplate for ~5-10minutes. In this step, PMMA deposited substrate was dipped in DI water and kept inside for 2-4 minutes. Next,

PMMA/MoS_2 layer started detaching from the substrate due to the hydrophobic nature of MoS_2 and was floating on the surface of water. Here the PMMA/MoS_2 layer was transferred to new substrate (bare interdigitated device on sapphire substrate). Later, PMMA/MoS_2/interdigitated pattern was dried for ~10minutes on a hotplate followed by completely removing the PMMA using an acetone solution.

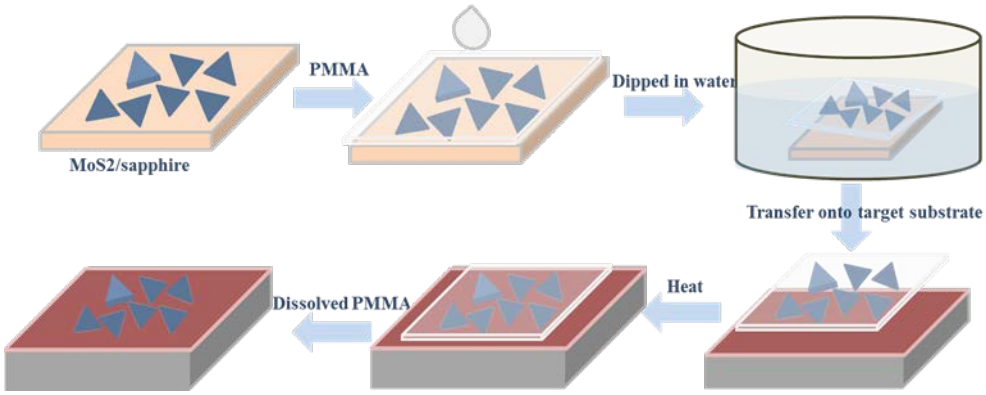

Figure 8-2. Steps to transfer MoS_2 monolayers by PMMA

Finally, the complete device Packaging was done by mounting the device on printed circuit board (PCB), which is connected to the interdigitated pattern by metallic wire. Figure 8-3 shows a photograph of one of the fabricated two-terminal photodetector devices, wire bonded to copper pads on a printed circuit board (PCB).

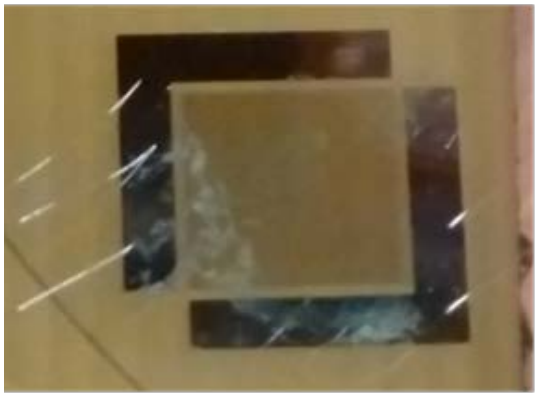

Figure 8-3.Two terminal MoS_2 interdigitated device

8.3 Photodetector

The electrical and opto-electronic properties of MoS_2 interdigitated device was explored by mounting the device on a probe station as shown in Figure 8-4. The schematic of the device with the illumination light from top using a xenon lamp is shown in Figure 8-5.

Figure 8-4.Probe station to measure I-V characteristics of device

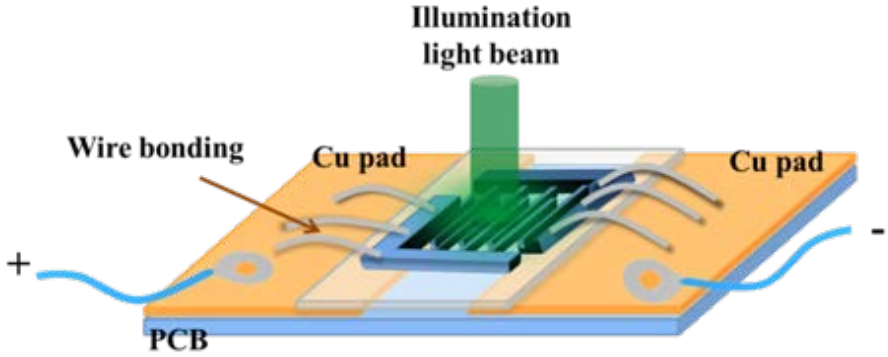

Figure 8-5.Schamatic illustration of the photodetector

8.3.1 Current-Voltage (I-V) Characteristics of Photodetector

In this device characteristics section, we first discuss the I-V measurements in dark and in presence of incident light of different wavelengths as shown in. The measurement had been done at room temperature under the N_2 atmosphere. The device in dark was scanned from -1 to +1V and the respective dark current were measured 5.65µA at +1V and -1V. It has been noted the (I-V) characteristics of the monolayer MoS2 device showed a linear behavior, which exhibit the

Ohmic nature of the metal contacts used. A significant photocurrent $I_{ph} = (I_{illuminated}-I_{dark})$ was obtained in the case of MoS2 monolayers under the illumination of two selected incident wavelengths, 450 and 530nm, obtained from a Xe lamp filtered through a monochromator. Both the incident wavelengths have energy greater than the bandgap of MoS_2 (1.84eV) and causes the photo-generation of charge carriers (excitons) in the material and results in rise in photocurrent.

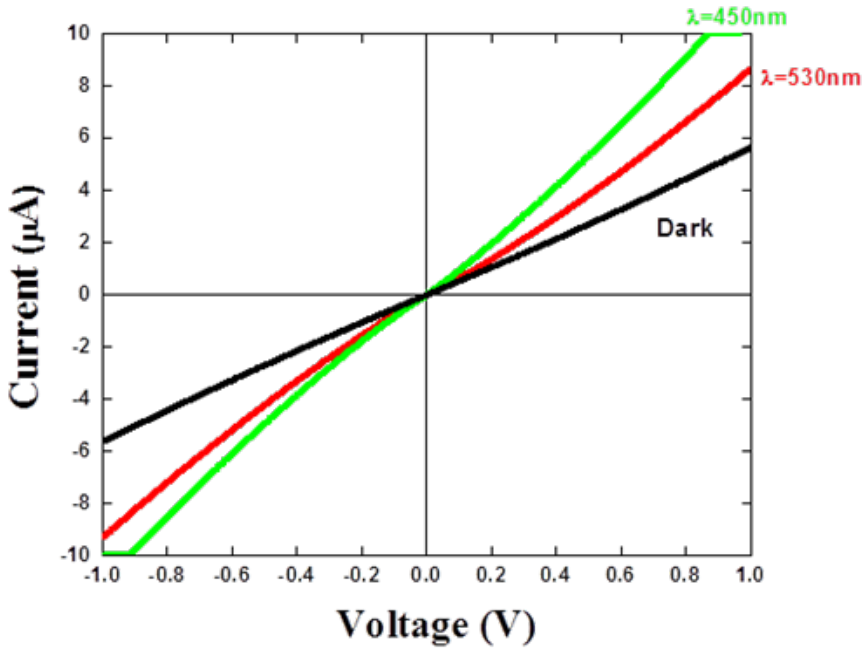

Figure 8-6. Current-voltage characteristics of (a) monolayer MoS_2, in dark conditions and when illuminated under λ=450 and 530nm light.

8.3.2 Photo-Responsivity vs. Wavelength of Photodetector

Photoresponsivity is one of the critical parameter of the photodetector to evaluate its performance. It is expressed as[105],[106],[107], $\mathcal{R} = \frac{I_{ph}}{A \times P_{opt}}$, where I_{ph} is the photocurrent, P_{opt} is the incident optical power density and A is the MoS_2 covered area (~$2mm^2$) on the device. Photoresponsivity is the photocurrent generated from the photodetector with an effective area A per unit power of incident light. The measured spectral photoresponsivity of MoS_2 based photodetector at a biased voltage of 1V is shown in Figure 8-7. In particular, we clearly observe

the near band-edge exciton-related photoresponsivity peaks at 660 and 615nm in the device. The energy separations between the peaks, ~138meV, which is in good agreement with the spin-orbit splitting of the valence band in monolayer. It has been noticed that the responsivity increases for wavelengths below 450nm, due to strong absorption near the van Hove singularities of MoS_2. The monolayer photodetector exhibited a very large responsivity, ranging between 6~10A/W in the measured spectral band in visible range. The responsivity dropped rapidly for wavelengths longer than ~675nm, which corresponds to the direct bandgap nature of MoS_2 and is consistent with the PL measurements.

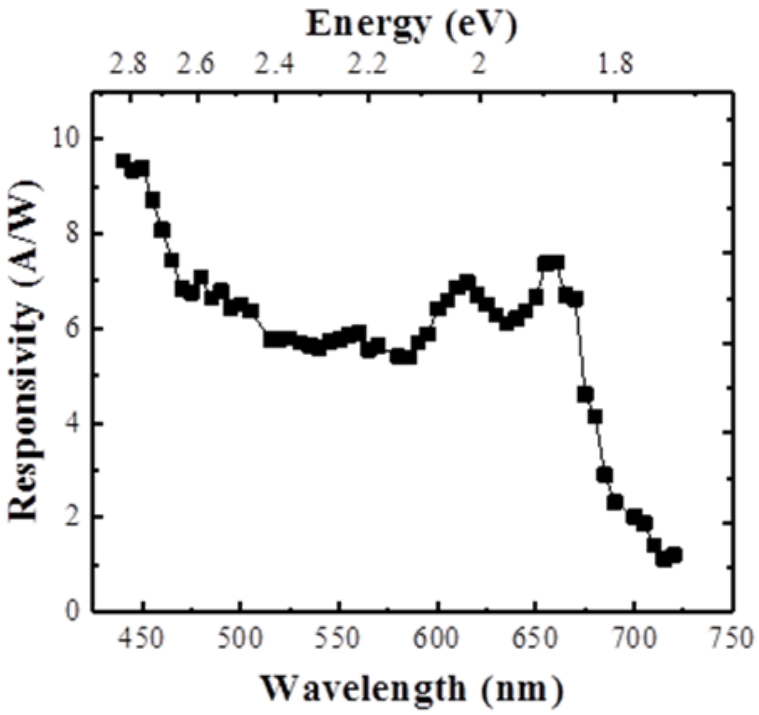

Figure 8-7. Spectral photo-responsivity of the photodetector

To examine the photo-responsivity curve, optical absorbance spectra on bare MoS_2 monolayer was taken as shown in Figure 8-8. As seen, two exciton peaks A at 672nm and B at 623nm were received and also maximum absorbance occurred at 435nm, which is due to Van Hove

Singularity at that point. Thus, the as received absorbance spectra is an exact replica of photo-responsivity curve.

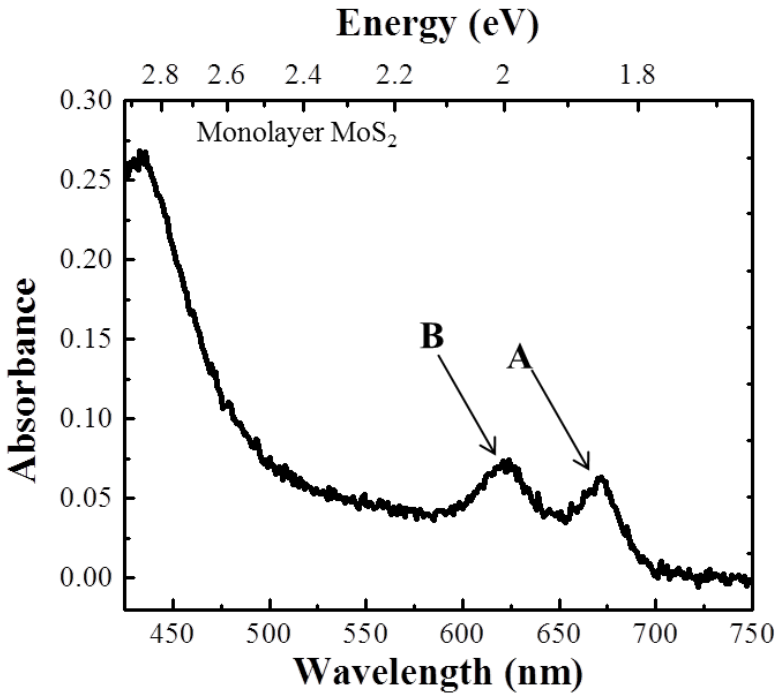

Figure 8-8.Absorbance spectra on MoS_2 monolayer

8.3.3 Photo-Responsivity and Gain vs. Incident Light Intensity

Spectral photo-responsivity has a much dependence on the incident power density. The plot of responsivity with incident power within range of 1μW/cm^2 - 7μW/cm^2 at wavelength of 532nm has been shown in Figure 8-9. Noted that spectral photo-responsivity increases by decrease in incident power and reached at 11.7A/W at lowest power illumination of 1.31μW/cm^2. This can be described by the presence of trap states either in MoS_2 or at the interface of MoS_2 and substrate. Under the illumination of high optical power, there is a reduction in density of available states, which causes the saturation of photoresponse and leads to decrease in photo-responsivity.

The photoresponsivity can also be written as[108],[109], $\mathcal{R} = \eta G \frac{q\lambda}{hc}$, where η is the quantum efficiency, G is the photoconductive gain, λ=532 nm, h is Planck's constant, and c is the velocity of light. The quantum efficiency represents the proportion of incident photons that are absorbed and lead to excess electron-hole pairs. Neglecting optical reflection at the surface, the quantum efficiency can be approximated by the following:

$$\eta \approx \left(1 - e^{-(\propto d)}\right)$$

where $(\propto d)$ is the absorbance at λ=532nm. We estimate η_{mono}≈4.9 % for the monolayers. The resulting photoconductive gain is shown in Figures 7(a) for the monolayer MoS_2. In this cases, we see an increase in responsivity (and thus G) when optical excitation power is reduced, with values of G doubling to reach 550 for the monolayer photodetector. In semiconductors, a high photoconductive gain generally indicates the presence of mid-gap states that trap one type of photo-generated carriers (e.g. holes in GaN, ZnO, MoS_2[110],[111],[112]), thereby resulting in a much longer effective lifetime of the other type of carriers (e.g. electrons) and allowing these to effectively travel multiple times across the contact electrodes in order to maintain electrical charge neutrality for the same absorbed photon. In the case of MoS_2, such traps are likely found either at the material top surface or interface with the sapphire substrate.

To better understand the dynamics of charge carriers, including trapping, in the case of the monolayer photoconductor, we plotted the photocurrent as a function of illumination power in the inset of Figure 8-9 and found it had a sub-linear power dependence: $I_{ph} \propto P_{opt}^{\gamma}$ with γ=0.57. Earlier reports of MoS_2 (phototransistor) detectors exhibiting a similar relationship with illumination yielded an exponent in the range 0.5~1, and hinted at a dependence of the exponent on defects present in the material when below 1. In our devices, the presence of defects is consistent with the photoconductive gain, as well as the grain boundaries commonly associated

with a continuous film of MoS_2. However, as shown below, we also believe that there exists a dependence of the exponent on the on the illumination regime (i.e. range of optical power density) in addition to the presence of defects. Since there exist a very wide range of sizes and quality for MoS_2 materials used as photodetector in the literature, as well as a wide range of optical power densities, comparison between the reported power dependence of photocurrent in MoS_2 photodetector devices must take into account both material characteristics and experimental measurement conditions.

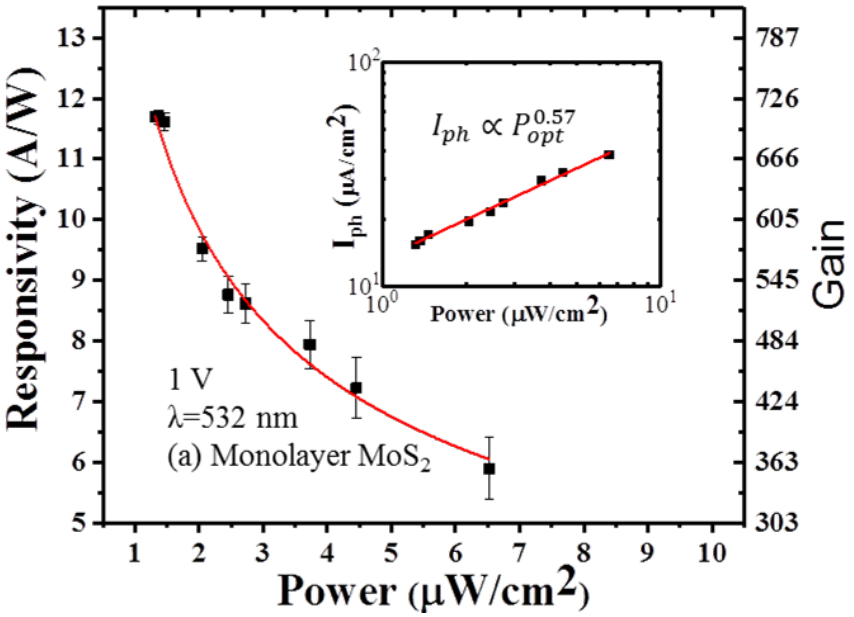

Figure 8-9. Spectral responsivity and Gain dependence on incident power density

8.4 Carbon Dioxide Gas sensor

Gas sensing behavior of MoS_2 has been realized by many different research groups[113],[114],[115],[116]. In this section, we will talk about the gas sensing behavior of MoS_2 which has been exploited for many different types of gases. The basic working principle of MoS_2 based gas sensor depends upon the type of gas being sensed. If the exposed gas is electron donor such as O_2, NH_3, the charge transfers from the gas molecules to MoS_2, which results in electrons accumulation in MoS_2 and leads to increase in current or conductivity through the sensor. In contrast, if the gas is

electron withdrawing (NO_2) then upon exposure, a decrease in current through the device will occur[117]. Since CO_2 is electron rich gas, so it possesses electron transfer characteristics to MoS_2 monolayer as shown in Figure 8-10.

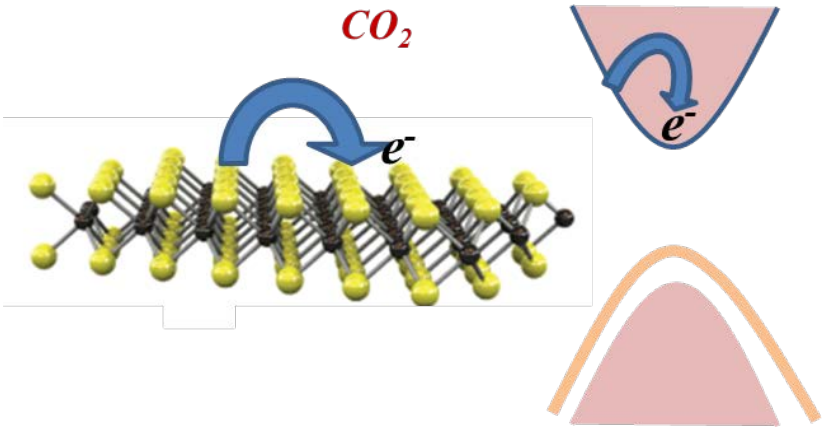

Figure 8-10.schematic illustration of electron transfer from CO2 to MoS_2 monolayer

8.4.1 Experimental Set-up

The experimental setup customized by us is shown in Figure 8-11. Using this set-up the data of real time CO_2 gas sensing behavior of MoS_2 based device had been collected at ambient conditions and analyzed the minimum detection limit of our device. The setup consisted of CO_2 and N_2 cylinders, where CO_2 was a sensing gas and N_2 was a dilution gas. Device was sealed in a quartz tube to avoid any leakage. The N_2 and CO_2 gases were introduced into the quartz tube through the mass flow controllers (MFC). Prior the testing of CO_2 gas, the device was kept under the N_2 atmosphere and dark to minimize the effect of ambient gases and stray light. The electrodes of the device were connected to the source meter to provide the required biased voltage and to measure the respective current.

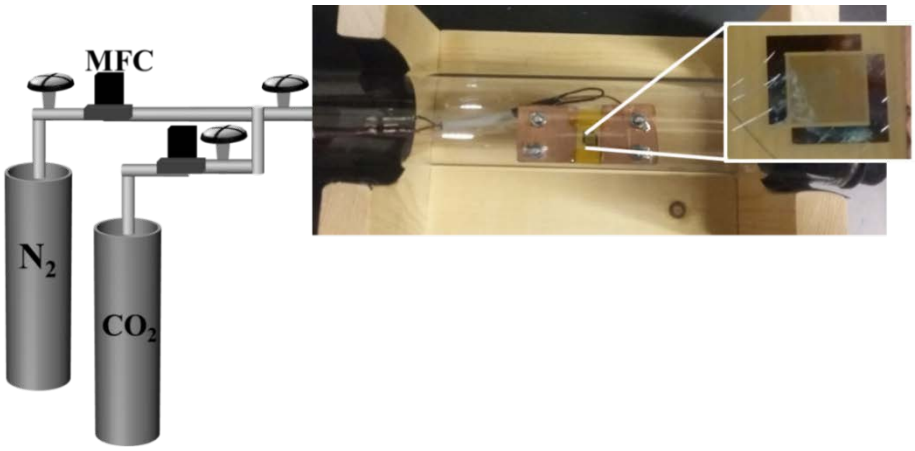

Figure 8-11. MoS_2 monolayer gas sensor setup

8.4.2 Results and Discussion

The sensing behavior of the gas sensor was explored using CO_2 gas and has been shown in Figure 8-12. The sensing response was collected at a biased voltage of 300mV. The base current through the device was recorded at N_2 atmosphere. The CO_2 gas at a 200ppm concentration for 60s was then exposed to MoS2 based gas sensor. Upon the interaction between CO_2 gas and MoS_2 monolayer, a significant rise in current had been seen. When the flow of gas was switched off for 180s and the device was again in total N_2 atmosphere, the current through the device was started to reach its original value. It had been seen that, upon the exposure of higher concentration of CO_2 gas, the current increases abruptly. It has been observed that response time of the sensor was much lower than the recovery time. Sensor was also exposed to the CO_2 gas concentration below 200ppm, but no response was found. Thus, the minimum detection limit of our sensor was 200ppm.

In another study the device sensing response has been recorded by exposing minimum 200ppm CO_2 gas for various durations ranging from 60s to 210s as shown in Figure 8-13. It is clearly exhibit that with the rise of exposure time of CO_2 gas on the MoS_2 device, the current enhances which reveal the electron donor property of CO_2 gas.

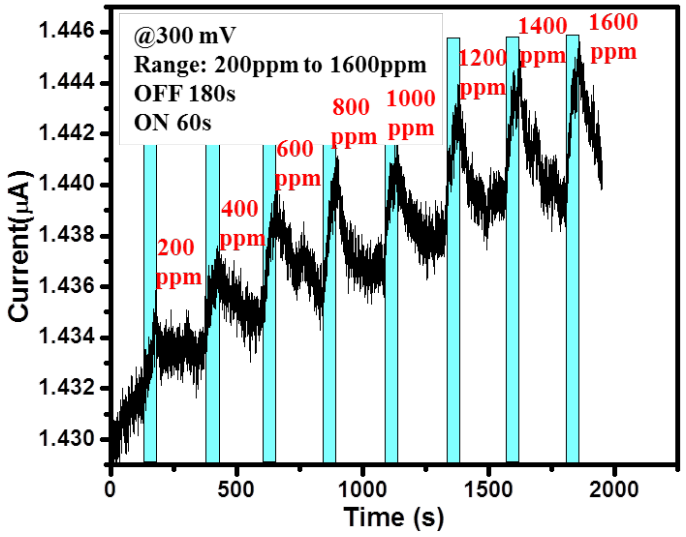

Figure 8-12.Sensor response to different concentrations of CO_2 gas

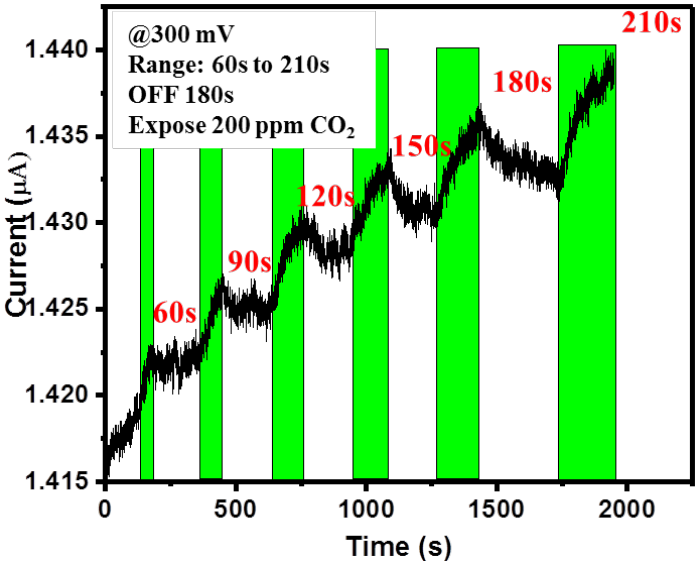

Figure 8-13. Sensor response to different exposure time of CO_2 gas

The relation between changes in current with test gas concentration is called a sensitivity, which is defined for sensors as,

Sensitivity (%) = $\left(\frac{I_{CO2}-I_{inert}}{I_{inert}}\right)$ X 100, Where I_{inert} is the current in N_2 inert atmosphere and I_{CO2} is the current in presence of test gas.

Figure 8-14 represent the plot of sensitivity with concentration of CO_2 gas exposed. Sensitivity increases with the increase in exposed gas concentration. However, at higher concentration of CO_2, saturation in sensitivity has been seen.

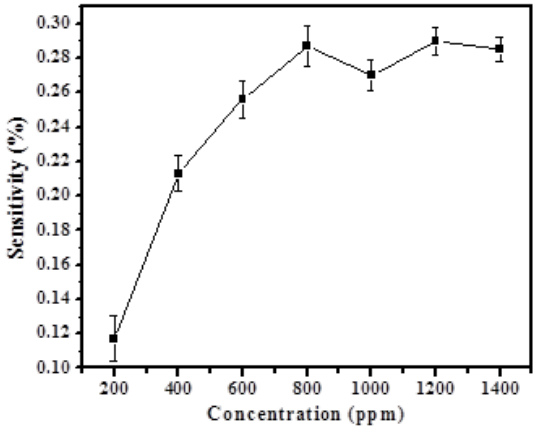

Figure 8-14.Sensitivity vs CO_2 concentration

CHAPTER 9.
NOISE

9.1 Introduction

Noise is the significant problem in all semiconductor devices. The presence of noise limits the accuracy of the detected signal. In semiconductor devices, it is usually an un-called signal at the low frequencies; however, sometimes the noise signal is useful for the quality check in semiconductor devices. The inherent noise in the devices is a superimposition of many types of noises. Some of the major types are: thermal noise, shot noise, generation-recombination noise and flicker noise or 1/f noise.

9.1.1 Shot Noise

Shot noise is one of the most fundamental noises, which is related to the structure and nature of matter. It arises by considering a discrete nature of charge carriers and is governed by statistical laws. In photoconductors, shot noise is caused by the statistical fluctuation in charge carriers, which further cause a fluctuation in the flow of current.

Shot noise current is expressed by the formula,

$$I_{SN}^2 = (2qI_{dark}\Delta f) \qquad 7$$

Δf is the noise measurement bandwidth, and q is the electronic charge.

Shot noise is an intrinsic noise and is independent of the frequency and solely determined by measuring the dark or saturation current and the bandwidth

9.1.2 Thermal Noise or Johnson Noise

Thermal noise is also another type of fundamental noise. It is caused by the collisions between moving free electrons and the lattice atoms at temperature T inside a matter of resistance R which generates fluctuations in the motion of free electrons; in contrast to shot noise, which is produced by the fluctuations in the number of free charge carriers. The well-known thermal noise current expression is

$$I_{Th}^2 = 4\mathrm{KTR}\Delta\mathrm{f} \qquad 8$$

K is Boltzmann's constant, and Δf is the frequency bandwidth

9.1.3 Flicker Noise or 1/f Noise or Pink Noise

Low frequency noise or 1/f noise is a matter of growing concern in nanoscale devices. It is the fluctuation in the conductance of the device. The typical feature of 1/f noise is its dependence on frequency. The power spectral density (PSD) or square of the noise current is inversely proportional to the frequency. It was first detected by Johnson while working on vacuum tubes. Later, this unwanted noise was further detected in photodiodes, MOSFETs [118], crystal rectifiers and photoconductors [119]. At low frequencies (f < 10Hz), this noise is the most dominant in the electrical devices. However, at higher frequencies, 1/f noise was expected to decrease faster, but this trend has never been observed because at higher frequency, 1/f noise merges or disappears in thermal or shot noise. Unlike other noises (shot and thermal), which are totally intrinsic phenomena, 1/f noise is totally extrinsic and a surface phenomenon, and is particularly sensitive to imperfections, contact potential, surface states, trapping/detrapping states, defect-defect scattering and variations in charge mobility. Therefore, this noise is quite prevalent and significant in thin film and polycrystalline devices.

In order to understand the 1/f dependence, we must first consider the semiconducting thin film consists only one type of trap state and trapping/detrapping occur at a time constant τ_1. This single process assists with the finding of auto-correlation factor of the resistance of thin film decay like $\exp(-t/\tau_1)$ [120],[121]. The Fourier transformation of this function leads to a noise spectrum, $S_x(f)$ or PSD,

$$S_x(f) = \frac{\tau_1/\pi}{1+(\omega\tau_1)^2} \qquad 9$$

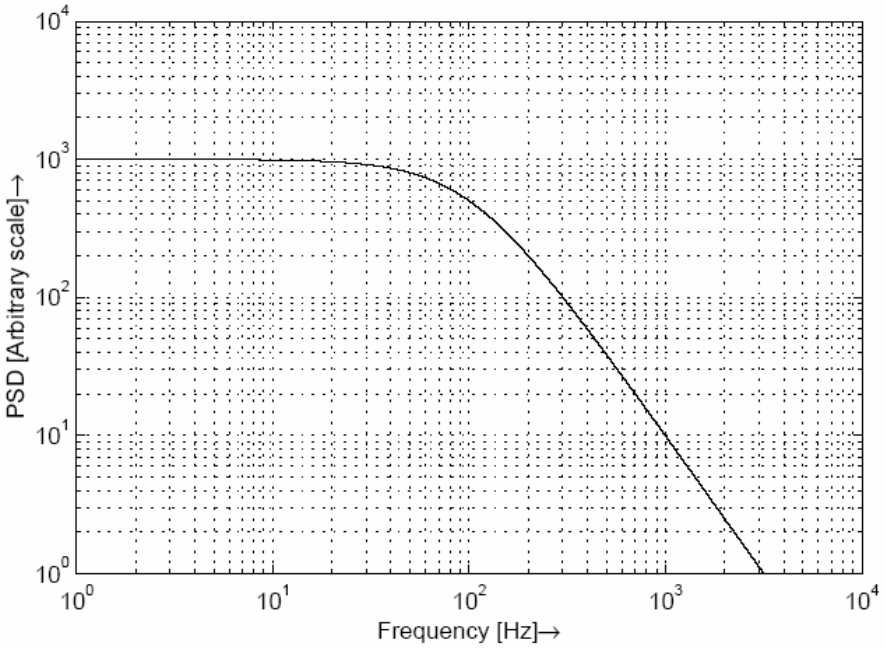

Figure 9-1: PSD with frequency for single trap state[122]

Now the case for an infinite number of trap states with different time constants will lead to the integration of all trap states. Thus,

$S_{1/f}(\omega) = \int_0^\infty \frac{k}{\tau_1} \frac{\tau_1/\pi}{1+(\omega\tau_1)^2} d\tau_1$, $\frac{k}{\tau_1}$ is the frequency of occurrence of one event related to τ_1 time constant, k is a constant. On solving, the above equation leads to $S_{1/f}(\omega) = \frac{C}{\omega} = \frac{C}{2\pi f}$.

Thus, the total power spectral density (PSD) depends inversely to the frequency as hence illustrated in Figure 9-2.

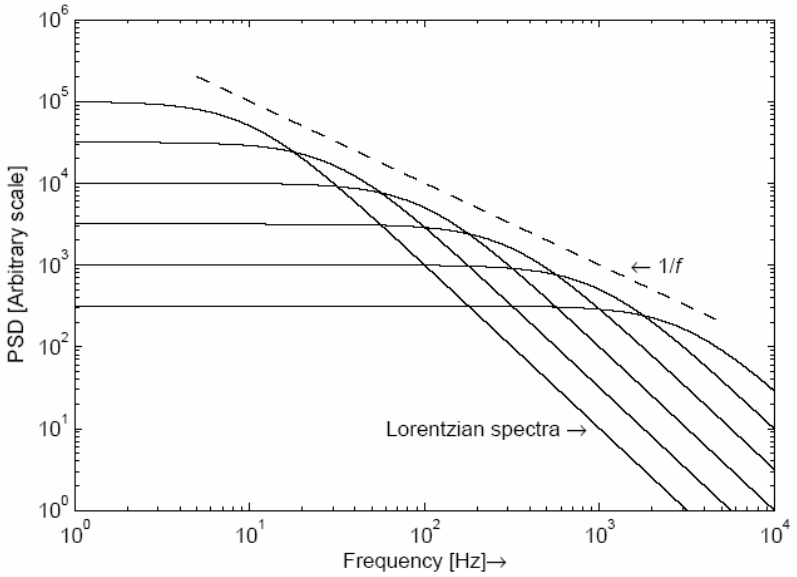

Figure 9-2: 1/f dependence of PSD due to many trap states[122]

9.2 Experimental

Herein, we gauge systematically 1/f noise spectral density ($S_{1/f}$) at room temperature using a 3582A Hewlett Packard spectrum analyzer as shown in Figure 9-3.

Figure 9-3. Spectrum Analyzer

The photoconductor device was connected with the spectrum analyzer as shown in Figure 9-4. The device resistance 178Kohm was calculated using I-V curve in dark at 1V from Figure 8-6.

Since the used battery was of 1.5V, therefore, 90Kohm resistance was connected, which enabled 1V potential across the device.

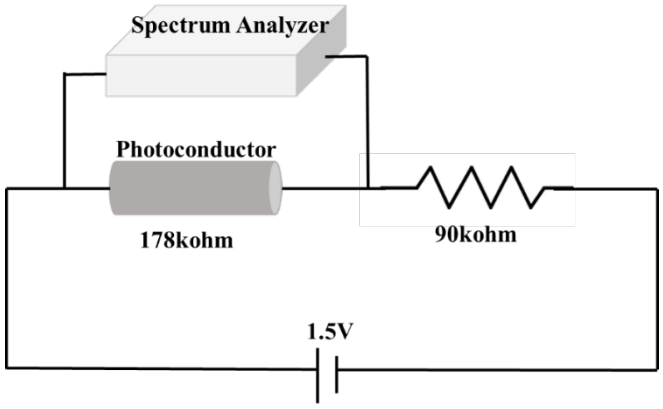

Figure 9-4: Schematic diagram of measurement setup of noise

9.3 Results and Discussion

The frequency dependence of noise spectral density is illustrated in Figure 9-5. The pattern of decrease of noise spectral density with the frequency clearly exhibits the inversely proportional of NSD on the frequency and endorses the theory of the cause of 1/f noise spectrum. Thereafter, noise spectral density (S1/f) at very low frequency 1 Hz was extracted out to be 5.33 x 10^{-21} A^2Hz^{-1}.

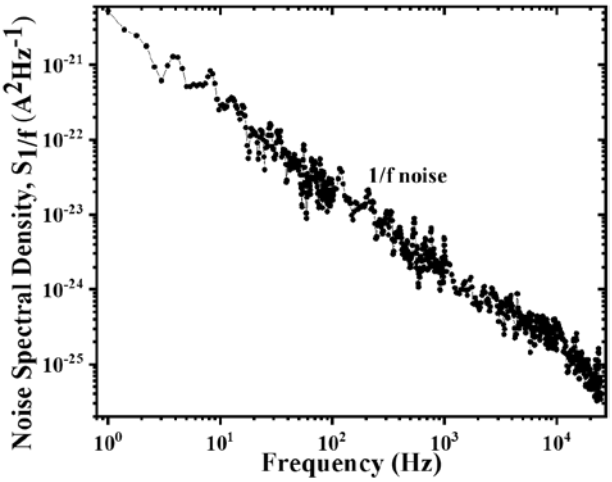

Figure 9-5: NSD with the frequency

Next, to determine the accurate sensitivity of the photodetector, we used the above calculated NSD at 1Hz. Specific detectivity (D*) is a figure of merit of the device and defines the true sensitivity, irrespective of the area of the thin film. The specific detectivity[123],[124] is defined as

$$D^* = RA^{1/2}/S_{1/f}^{1/2}$$

Where A is the area of the MoS_2 covered area which is $2mm^2$, R is the responsivity in AW^{-1}. After the careful addition of values, Figure 9-6 shows the calculated specific detectivity values at different wavelengths and the achieved value as high as is ~1.8 x 10^{10} Jones.

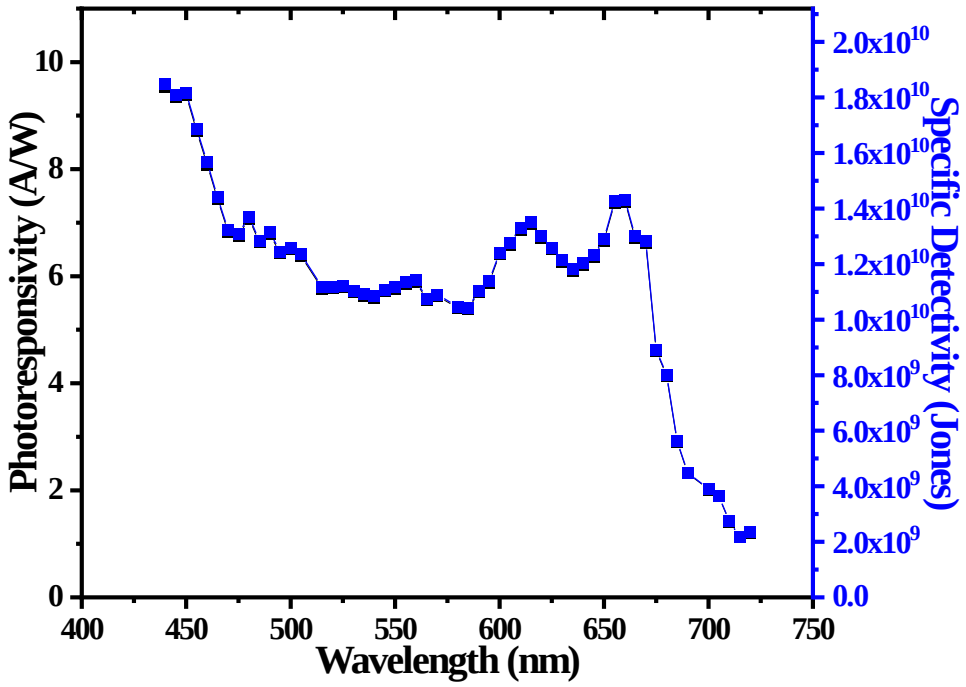

Figure 9-6: Specific detectivity values at different wavelengths

CHAPTER 10.
2D $MO_{1-X}W_XS_2$ TERNARY COMPOUNDS ON SAPPHIRE SUBSTRATES

10.1 Introduction

Since the 2D TMDC materials are known for thickness dependent bandgap property. Afterwards intensive study was carried out to modulate the bandgap of these TMDC materials for various applications in optoelectronic devices. In multiple efforts, alloying the 2D materials was extensively studied to tune the bandgap of the material such as the synthesis of $Mo_{1-x}W_xSe_2$, $Mo_{1-x}W_xS_2$[125] and $MoS_{2x}Se_{2(1-x)}$[126] monolayers. This is because these alloys are thermodynamically stable at room temperature as predicted by theoretical calculations[127]. Thus, here we studied the synthesis of doped 2D MoS_2 monolayer material with another transition metal atom (tungsten) through LPCVD and extensively investigated the change occur in the bandgap with the increase or decrease of W concentration through Raman and optical characterization.

10.2 Experimental

Unlike the previous CVD growth of MoS_2 monolayers, in this study a W containing precursor WS_2 was used with the MoS_2 powder as a precursor for Mo. The growth conditions and method of MoS_2 monolayers have been exactly the same as discussed in CHAPTER 3. In this growth method, high purity MoS_2 and WS_2 powder precursors (Alfa Aesar) were placed in a quartz boat at the center of a quartz tube. The growth occur at a pressure of 10 mbar under 20 sccm Ar flow, with the furnace temperature ramped to 970°C with a heating rate of 20.8°C/min, and hold at

970°C furnace temperature for a duration of 20 min. Afterwards, the furnace was allowed to cool down naturally.

10.3 Results and Discussion

10.3.1 Topography Study by Optical Microscope

Optical microscope images of as grown single crystal $Mo_{1-x}W_xS_2$ islands are shown in Figure 10-1. The common morphology of grown ternary compounds found is the triangular shape, with the lateral size varies from 40µm to 90µm.

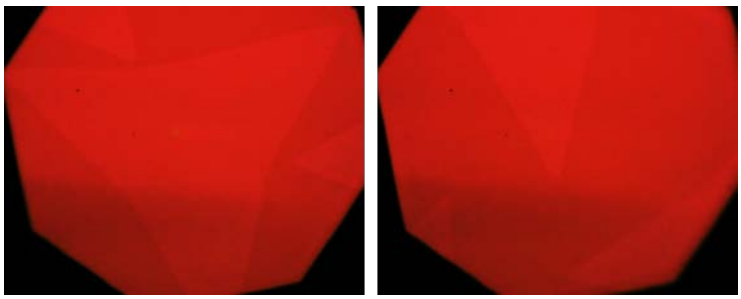

Figure 10-1.Optical images of as synthesized $Mo_{1-x}W_xS_2$ monolayered triangles

10.3.2 Micro-Raman Characterization of as Grown Ternary Compounds

Non-destructive micro-Raman spectroscopy technique was employed on as grown $Mo_{1-x}W_xS_2$ crystals. Since the alloyed triangular flakes were grown at different compositions of W, so the complete dependence of $Mo_{1-x}W_xS_2$ Raman signature peaks on x is shown in Figure 10-2. The recorded Raman spectra of pure MoS_2 (x=0) represent two characteristics peaks E^1_{2g} (384.3cm^{-1}) and A_{1g} (404.5cm^{-1}). With the rise in W doping (x ~ 27%), WS_2 monolayer Raman peaks E'^1_{2g} (+2LA) (352-357cm^{-1}) and A'_{1g} (416.7cm^{-1}) starts appearing with the two Raman peaks of MoS_2 monolayer. It has been noted that with an increase in W concentration, the relative intensity of WS_2 peaks starts increasing and MoS_2 Raman peaks starts decreasing. The broader width of WS_2 E'^1_{2g} peak is due to it consists of two peaks (first order mode at 357cm^{-1} and second order mode 2LA at 352cm^{-1})[128]. A significant red shift in MoS_2 Raman peaks (E^1_{2g} from

384.3 to 376 and A_{1g} from 404.5 to 396 cm-1) has been seen as the dopant W incorporated as shown in big red oval shaped circle in Figure 10-2. This shift is attributed to the local strain caused by mixing two different phases (Mo and W) in an alloy $Mo_{1-x}W_xS_2$ crystals[129].

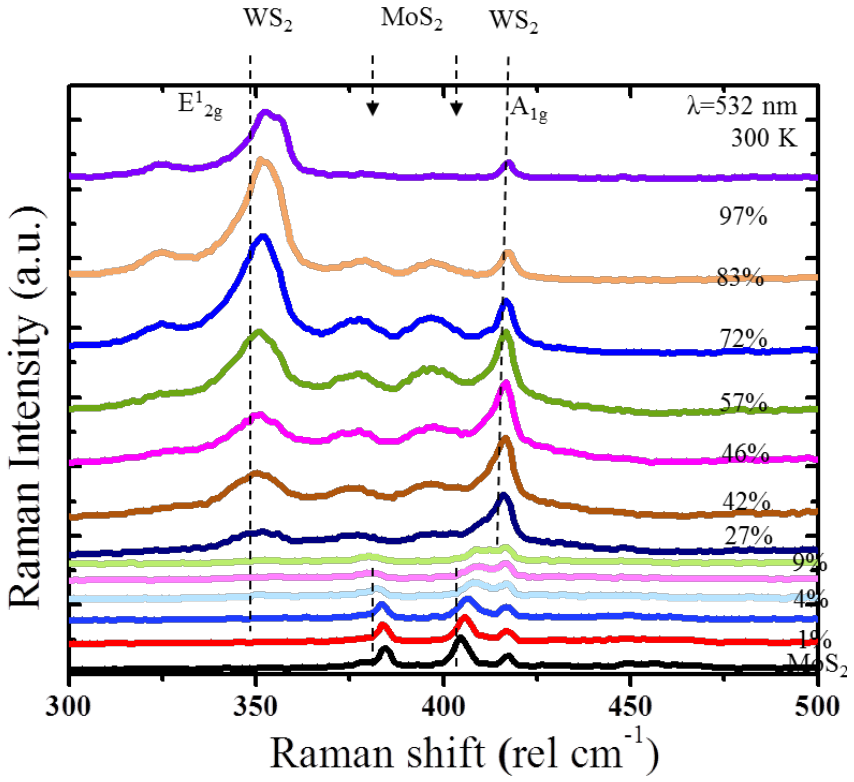

Figure 10-2.micro-Raman spectra at different compositions of $Mo_{1-x}W_xS_2$ monolayers

10.3.3 Micro-PL Characterization of as Grown Ternary Compounds

The optical properties of LPCVD grown ternary compounds has been analyzed using photoluminescence spectroscopy. The PL spectra of $Mo_{1-x}W_xS_2$ at different compositions have been shown in Figure 10-3. As the value of x increases from 0 to 1, the PL peak position blue shifts from 1.853eV to 2.01eV. The exact value of composition x can be estimated using the PL emission peak, assuming a linear relationship for the emission energy, $E_g = (1-x)E_{MoS2} + xE_{WS2}$, Where E_g is the PL peak position, E_{MoS2} = 1.853eV and E_{WS2} = 2.01eV.

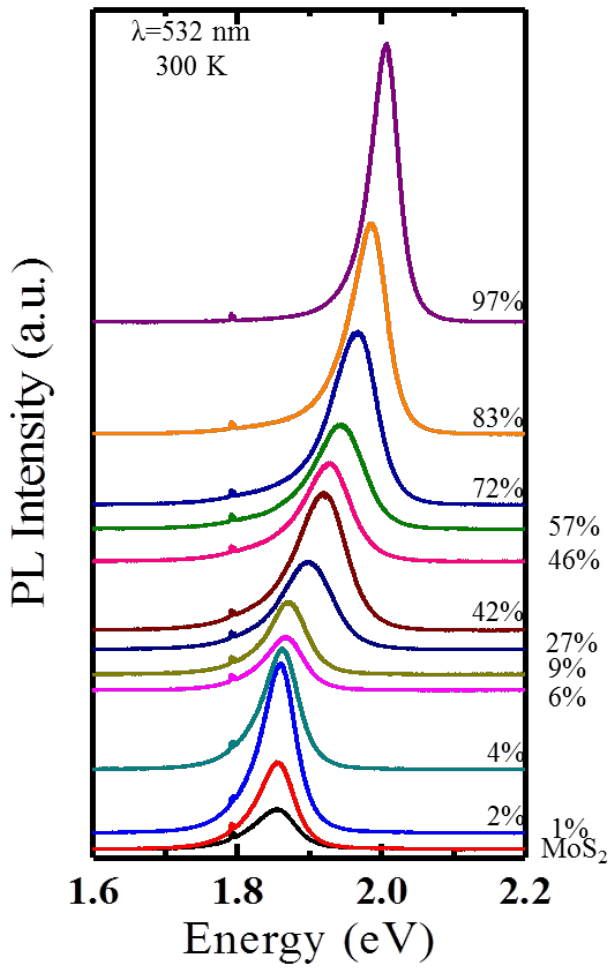

Figure 10-3. Micro-PL spectra at different compositions of $Mo_{1-x}W_xS_2$ monolayers

CHAPTER 11.
HETEROSTRUCTURES

11.1 Introduction

Semiconductor heterostructures play a vital role in the modern semiconductor devices such as solar cells and thin film transistors. Lateral heterostructures consist of binding two different materials. Over the last few decades, forming a perfect lattice matched heterostructure remains a big challenge. It is due to the fact that to form a perfect heterostructure, lattice matching between two different semiconducting materials is an essential requirement, and till date, no such two different materials were found with the same lattice constants. Why do we need two materials with the same lattice constant? It is because when two different materials are combined or fused together, due to lattice mis-matching, inevitably large number of defects also arises at the interface. These defect sites behave like the generation and recombination centers or trap states for the charge carriers, due to which the charge carrier transport or the flow of charge carriers across the interface is greatly hampered and results in the poor performance of the opto-electronic device[130]. Some heterostructures are widely developed using III-V semiconductors for high frequency applications. In-spite of many efforts, the lack of perfect lattice matching between two materials limits the III-V based heterostructures for device fabrication. Most state-of-the-art efforts to reduce these defects or the strain are by inserting a thin oxide layer between GaAs/GaN, Si/GaN[131], and by inserting an amorphous thin InAs buffer layer between InGaAs and GaAs(111)[132]. However, the formation of

such structures is quite difficult as the buffer layer should be very thin and lack of uniformity cause further defects.

After the detailed study of MoS_2 monolayers from growth to the charge transport properties involving the in-depth characterization, these 2D MoS_2 materials also show the possibilities of formation of lattice matched heterostructures with other 2D materials. The limitation of lack of lattice matching and defect formation at the interface can very well be overcome by combining these Vander walls based 2D materials. Among the many combinations of two different 2D TMD materials, MoS_2/WS_2 is widely explored because of perfect lattice match materials with different work functions[133,134,135,136] and the formation of type II heterojunction[137,138,139,140,141,142]. In type II heterojunction, the lowest conduction band minimum (CBM) lies in the MoS_2 monolayer, and the highest valance band maximum (VBM) resides in the WS_2 monolayer as illustrated in Figure 11-1.

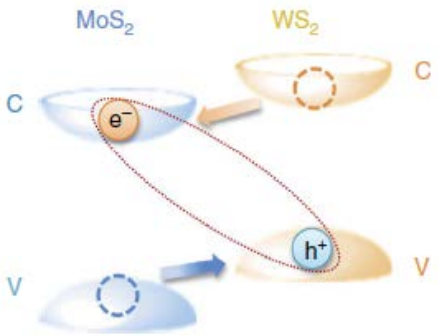

Figure 11-1: Type II band alignment diagram of MoS2/WS2 heterostructure[143]

Optical excitation of these heterostructures with a laser energy higher than the respective bandgaps of MoS_2 and WS_2 leads to the formation of interlayer exciton. In the interlayer exciton, electron lies in the minimum of the conduction band of one material and hole in the maximum of the valance band of adjacent connected material. Similarly, in the case of MoS_2/WS_2 heterostructures, electron flows from WS_2 to MoS_2 and start accumulation in the conduction

band of MoS_2 and holes flow from MoS_2 to WS_2 and start accumulation in WS_2 monolayer and results in the formation of interlayer excitons. Such heterostructures (HS) are very rare and not much is known about their characteristics. They can only be achieved through a synthetic growth process such as chemical vapor deposition (CVD). This is unlike vertical heterostructures, for which the materials can be mechanically stacked one layer on top of the other. The CVD growth of in-plane heterostructure is a thermodynamically driven process and presents several challenges to control the vapor pressure of the precursors. Additionally, new analytical tools need to be developed in order to gain access to and understand the physical properties of these HS.

11.2 Experimental Growth of Lateral Heterostructures

Unlike the previous CVD growth of MoS_2 monolayers, in this study a W containing precursor WS_2 (2g) was used with the MoS_2 powder (2g) as a precursor for Mo. The growth conditions and method of MoS_2 monolayers have been the same as discussed before. In this growth method, high purity MoS_2 and WS_2 powder precursors (Alfa Aesar) were placed in a quartz boat at the center of a quartz tube. The growth occurs at a pressure of 10 mbar under 20 sccm Ar flow, with the furnace temperature ramped to 970°C with a heating rate of 20.8°C/min, and hold at 970°C furnace temperature for a duration of 20 min. Afterwards, the furnace was allowed to cool down naturally.

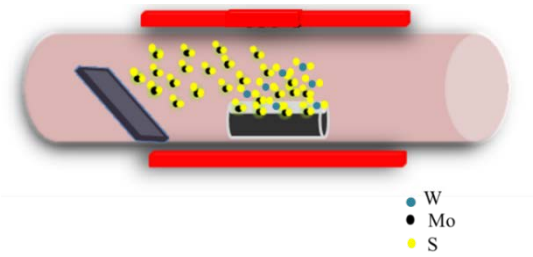

Figure 11-2: Illustration of CVD to grow MoS_2/WS_2 HS

The growth mechanism of LHS occurs in sequence as shown in Figure 11-3. Since the vaporization point of MoS_2 precursor is lower than the WS_2 precursor, therefore, at the beginning of the reaction, MoS2 vapor pressure at the top of the substrate is the dominating one and MoS_2 adatoms starts depositing in the form of monolayers but after some time, the vapor pressure of WS_2 becomes dominant and the MoS2 source starts depleting and the equilibrium conditions favors the deposition of WS_2 adatoms. Also because the MoS_2 and WS_2 molecules have huge similarity, and it leads to the diffusion of WS_2 molecules at the MoS_2 terminating edges and hence formation of WS_2 monolayers with the MoS_2 monolayer in the core.

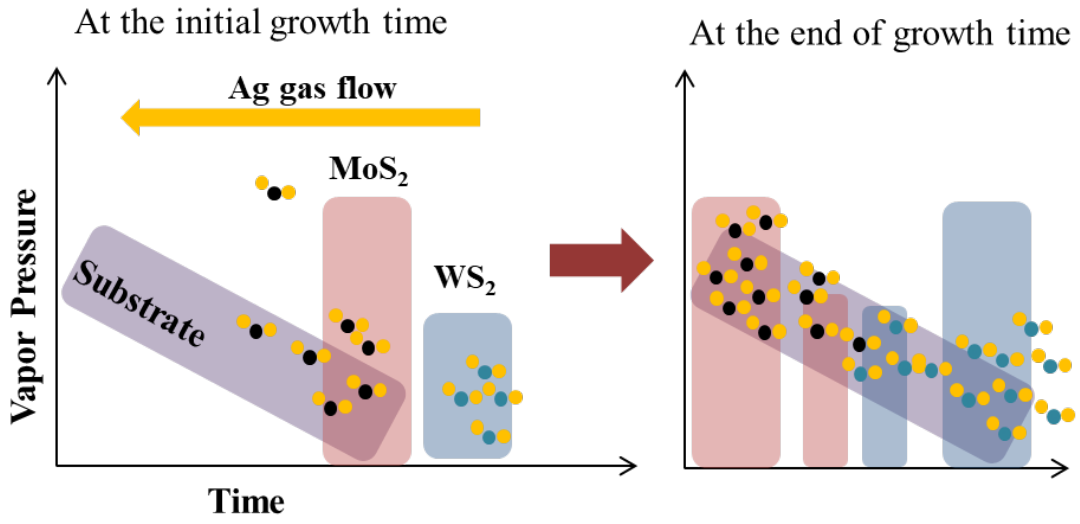

Figure 11-3: Illustration of variation of vapor pressure to deposit the LHS

11.3 Results and Discussion

11.3.1 Topography Study by Scanning Electron Microscope and Confocal Microscope

Topological characterization of flakes revealed the formation of some hexagons/triangles with dark contrast in the core as shown in SEM images in Figure 11-4. Heterostructures with a shell region were expected to be WS_2 monolayer with MoS_2 region at the core.

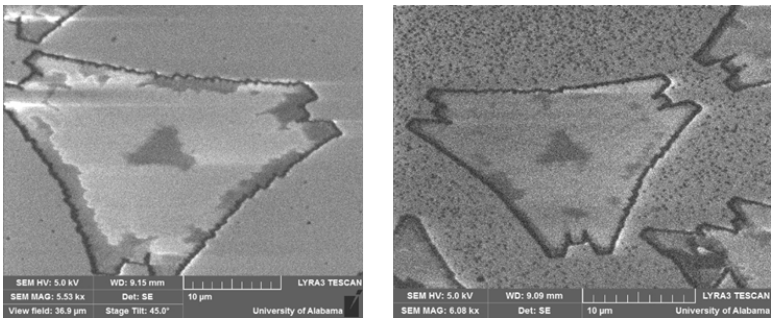

Figure 11-4: SEM images of MoS_2/WS_2 heterostructures

The grown heterostructures were examined under a confocal microscope and images are shown in Figure 11-5. Nano flakes were excited using 560nm wavelength. Two detectors were used with a detection bandwidth of 610-630nm for detecting WS_2 monolayer and 665-680nm for detecting MoS2 monolayer. As a result, the clear contrast was visible between the middle portion and the peripheral region of the formed hexagon. The edge length of core triangular MoS_2 region is 12µm and the diagonal shell WS_2 region is ~25µm.

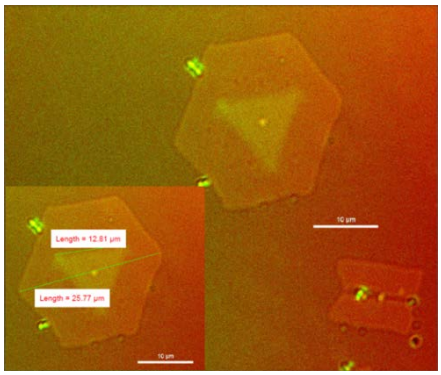

Figure 11-5. Confocal microscope image of heterostructure with an inset image with dimensions

11.3.2 Optical Characterization of core, shell and junction regions of MoS_2/WS_2 Heterostructure

To confirm the spatial distribution of as-grown hexagonal crystals, they were characterized using micro-Raman and PL spectroscopy at room temperature using 532nm wavelength on the points shown in optical images. Three different Raman spectra shown in Figure 11-6 had been taken from the interface, core, and shell regions. Raman spectra shown in red color represents two

characteristic Raman peaks of monolayer MoS_2, i.e. E^1_{2g} (in-plane mode) and A_{1g} out of plane mode at 383.5cm^{-1} and 404.7cm^{-1}. At the shell region, the Raman peaks existed at 353.2cm^{-1} and 417.8cm^{-1} and are shown in blue color, which in accordance with the pure WS_2 monolayer 2LA(M) and A_{1g} peaks[144,145,146]. The slightly broad 2LA(M) Raman mode of WS_2 monolayer is due to it consisting of 2 peaks, one is 2LA(M) at ~353.2cm^{-1} and another is E^1_{2g} at ~357cm^{-1}. 2LA(M) mode is a longitudinal acoustic in-plane vibration mode. However, Raman spectra at the junction or interface gave four Raman peaks as shown in yellow color which are characteristic peaks of both MoS_2 and WS_2 monolayers. Thus, the nature of as-grown MoS_2/WS_2 lateral heterostructures had been observed by the micro-Raman spectroscopy. Moreover, to further explore the monolayer nature of heterostructures, micro-PL spectra was taken at the same locations where Raman spectra was taken previously. The PL spectra at the core region exhibited a peak at 1.86eV, which is a bandgap of monolayer MoS_2. At the shell region PL peak existed at 1.99eV and that shows the monolayer WS_2. In addition, at the interface region, two PL peaks occurred simultaneously representing one for MoS_2 and the other for WS_2 monolayer. The small intensity of both peaks at the interface shows the charge carrier transfer between different bandgap materials.

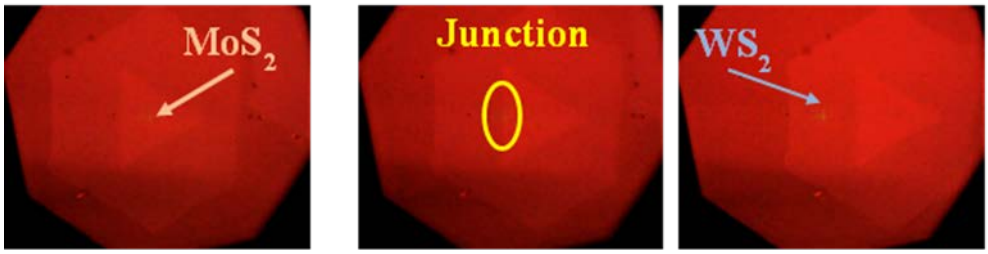

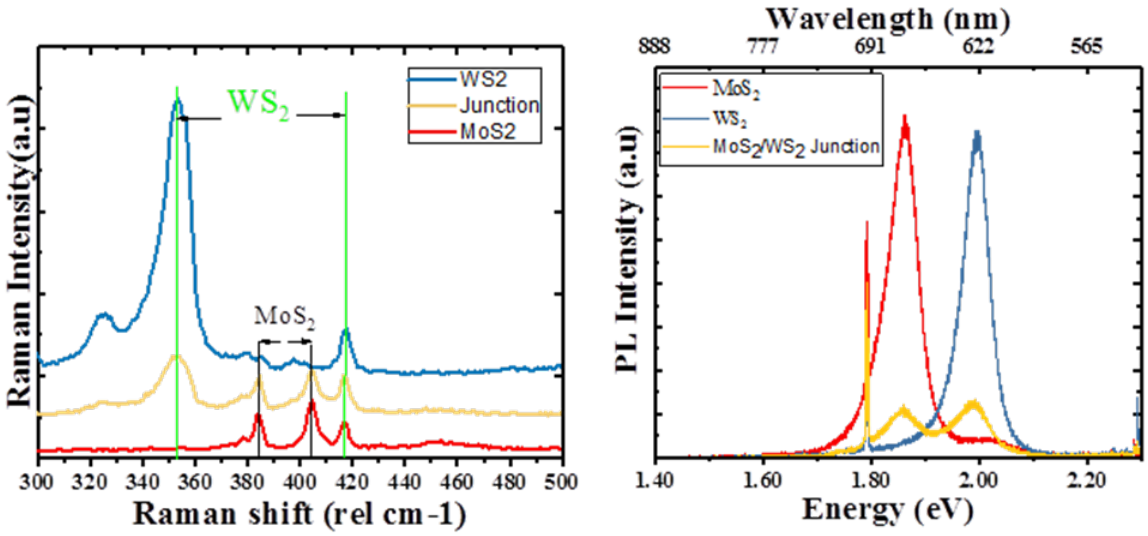

Figure 11-6. Optical microscope images and the Raman and PL characterization of heterostructures

11.3.3 Surface Morphological and Kelvin Probe Force Microscope Characterization of MoS_2/WS_2 Heterostructure on Sapphire and on Gold Substrates

To access the surface morphology of the as-grown lateral heterostructures, atomic force microscope analysis had been conducted as shown in Figure 11-7. AFM imaging on the 20µm topography image revealed the crystal at the core region, which is supposed to be MoS_2, is spatially surrounded by another crystal WS_2. The relatively bright MoS_2 core region signaled that it is not a monolayer in nature, however, corresponding step height at WS2 showed the thickness of as-grown crystals is less then 1nm, which exhibited the monolayer nature of WS_2 region. Since MoS_2 and WS_2 are two direct bandgap semiconducting materials with the same thickness in monolayer form but with different work-functions. Therefore, the seamless stitching between these two materials must be the cause of built-in-potential at the MoS_2 and WS_2 junction. Scanning kelvin probe force microscopy (SKPFM) is another variant of AFM and a very powerful tool in which local contact potential difference is measured between the conducting AFM tip and the sample. Thus, to explore the electrical properties of MoS_2/WS_2 lateral

heterostructures under thermal equilibrium, SKPFM analysis was assessed to find out the semiconductor junctions' most significant parameters such as built-in-potential and junction width shown in Figure 11-8.

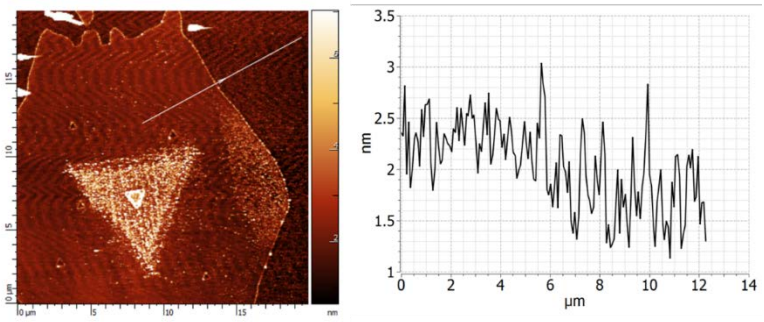

Figure 11-7. Topography image and corresponding step height analysis of a lateral heterostructure MoS_2/WS_2 crystal.

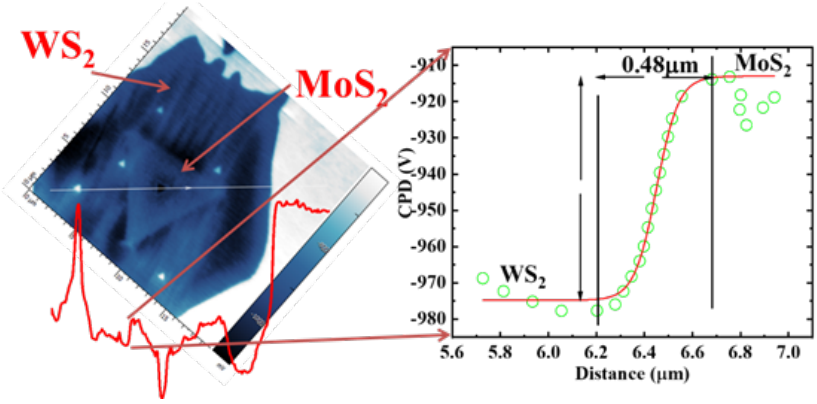

Figure 11-8. Scanning kelvin probe force microscopy imaging and contact potential difference across the MoS_2/WS_2 regions.

In this technique, the contact potential difference between semiconducting region (MoS_2 and WS_2) and the tip can be expressed as [147]

$$CPD_{WS2} = \frac{Wtip - W_{WS2}}{q}$$

$$CPD_{MoS2} = \frac{Wtip - W_{MoS2}}{q}$$

The scanned image of surface potential distribution on MoS_2/WS_2 heterostructure is shown in Figure 11-8 and the corresponding potential distribution profile has been shown in red. The Zoom-in profile (on the right of the image) represents the contact potential difference across the junction of MoS_2 and WS_2 monolayers. The fermi level difference between both semiconductors is extracted by subtracting the CPD of both the materials as mentioned,

$$\Delta E_F = \Delta CPD_{WS2\text{-}MoS2} = CPD_{MoS2} - CPD_{WS2}$$

The typical values of built-in-potential and junction width were extracted out to be 64meV and 0.48µm. The generated built-in-potential influenced the naturally separation of photo-generated electron and hole pairs in both MoS2 and WS2 monolayers in which electrons transfer to MoS_2 conduction band region and holes reside in WS_2 valance band region. Therefore, this inherent property of 2D heterostructures of intrinsic separation of generated electron-hole pairs within these materials is highly influential and significant in flexible optoelectronic and photovoltaic devices. The same study was also conducted on another MoS_2/WS_2 crystal as shown in the optical image in red circle in Figure 11-9.

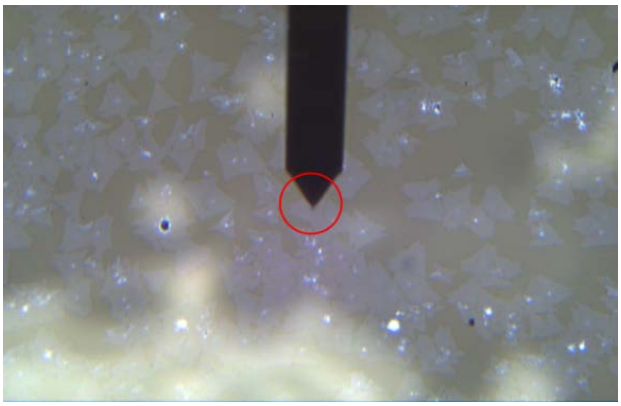

Figure 11-9. Optical image of selected MoS_2/WS_2 crystal on sapphire substrate for the analysis by SKPFM

The topography imaging done by AFM and the collected height profile of the selected heterostructure crystal is shown in Figure 11-10. The scanned height profile from WS_2 to MoS_2

region is completely horizontal and confirms the same thickness of both the materials, which supports the formation of lateral heterostructure monolayer. Since these two materials (MoS_2 and WS_2) have different work-functions, the corresponding contact CPD imaging collected by SKPFM demonstrated the clear contrast between the core MoS_2 and shell WS_2 regions.

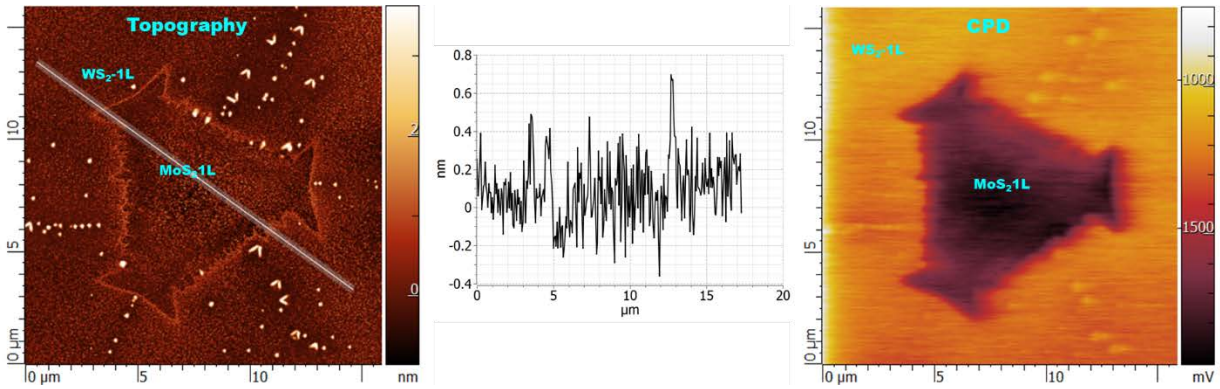

Figure 11-10. Topography and CPD imaging of another MoS_2/WS_2 monolayer crystal

In the further study on these heterostructures, a confocal photoluminescence imaging and spectra was recorded using 638nm and 532nm laser wavelengths as shown in Figure 11-11. At 638nm excitation wavelength, PL spectra was recorded at three different regions as shown in the rectangular boxes in the PL mapping image in Figure 11-11(a). The PL peak related to A exciton of MoS_2 monolayer occurred at 668nm shown in the red curve along with the broad and intense peak of heterojunction in the blue curve. Due to the inability to record below 638nm wavelength, the exact PL peaks of WS_2 monolayer and the junction was not captured. Further analysis with a 532nm excitation wavelength allowed us to record the complete spectra of MoS_2, WS_2 and the junction along with the exact PL peaks and is shown in Figure 11-11(b). It is noteworthy to understand that PL peak at the junction was recorded at 636nm, which is red shifted as compared to pure WS_2 PL peak at 628nm. Again, the broad peak at the hetero-junction is clearly visible as compared to the sharp WS_2 PL peak. The red shift of peak at the junctions is pointing towards the formation of ternary compound or alloy ($Mo_xW_{1-x}S_2$) at the transition region. Using Vegard's

law in the compound semiconductors, $E_{g,\ alloy} = xE_{MoS2} + (1-x)E_{WS2}$, the composition x was calculated to be around 0.21.

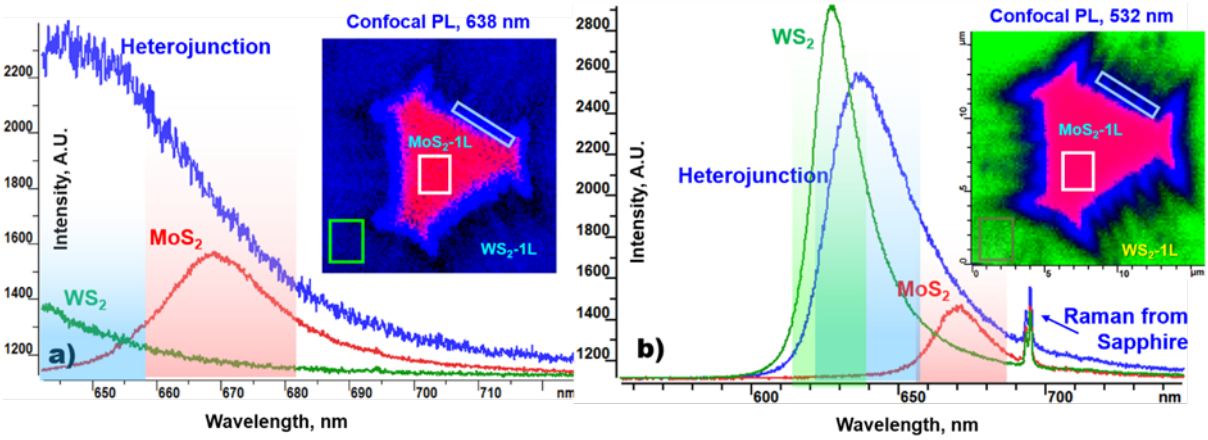

Figure 11-11: PL spectra and PL mapping images collected at (a) 638nm, (b) 532nm excitation wavelengths

However, conventional Raman and photoluminescence characterizations are a far field optical technique because of the diffraction limited spot size (400-550nm) and the applications of these techniques are restricted to the micro- and macro-worlds. In order to completely understand the lateral integration of two semiconducting materials at the nanoscale level, an essential nanoscale characterization technique is required, which should be near field technique with a significant high spatial resolution at the nanometric level. Plasmon enhanced optical spectroscopy such as tip enhanced Raman spectroscopy (TERS) and tip enhanced photoluminescence spectroscopy (TEPL) bridge the gap to NanoPL and offer high optical spatial resolution. These new techniques coupled with scanning probe microscope (SPM) provide an abundance of information on structural and optical properties of interfaces in such novel heterostructures. However, in order to study TERS in gap-mode conditions, these materials were transferred on metallic substrate through gold assisted transfer procedure[148]. In this transfer technique, a thin film of gold, ~70nm, was coated on the MoS_2/WS_2 on the sapphire substrate. Later, a transfer wafer was connected

using an epoxy resin to the gold coated sapphire substrate. When the epoxy resin was cured, the transfer wafer with a gold film consisting of heterostructures was stripped away from the sapphire substrate as illustrated in Figure 11-12.

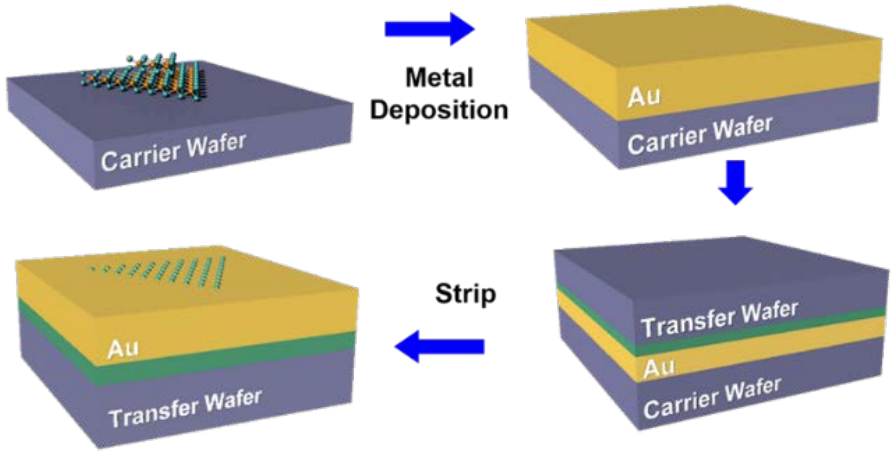

Figure 11-12: Illustration of transfer of MoS_2/WS_2 heterostructures from the sapphire substrate using a thin gold film

After the transfer of heterostructures on gold substrate, it was required to confirm if the structural and electrical characteristics of heterostructures were still alive, so, we had located the same heterostructure crystal that was characterized before transfer as shown in an optical image Figure 11-13. The optical image on sapphire was flipped horizontally for the ease of comparison between the images before and after transfer. The tip of the AFM cantilever is located over the same crystal and the characteristic marker spots are connected through yellow dotted lines.

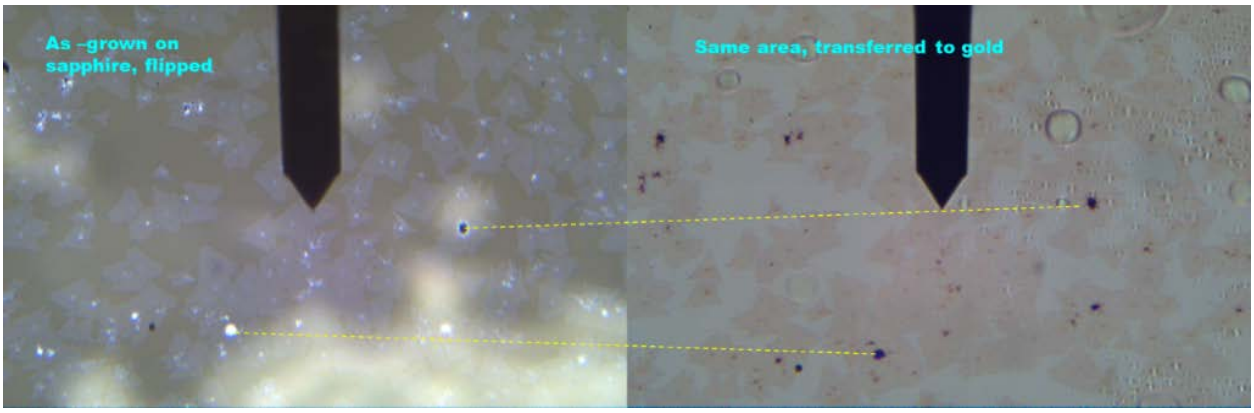

Figure 11-13. Optical image of same heterostructure crystal to be analyzed on before transfer (sapphire substrate) and after transferred on gold substrate

Subsequently, after locating the same crystal, topography and SKPFM measurements were conducted as shown in Figure 11-14. As can be seen in the topography image, MoS_2 core region is quite indistinguishable from the WS_2 shell region and the height profile is fairly smooth. Moreover, SKPFM image clearly shows the bright core MoS_2 region and the WS_2 shell region and the corresponding contact potential difference profile is shown. The extracted value of CPD between MoS_2 and WS_2 monolayers was ~150meV, which is quite consistent with the reported values[149]. The topography image (e) is the AFM image before transfer and was flipped to show a comparison of flake before and after transfer.

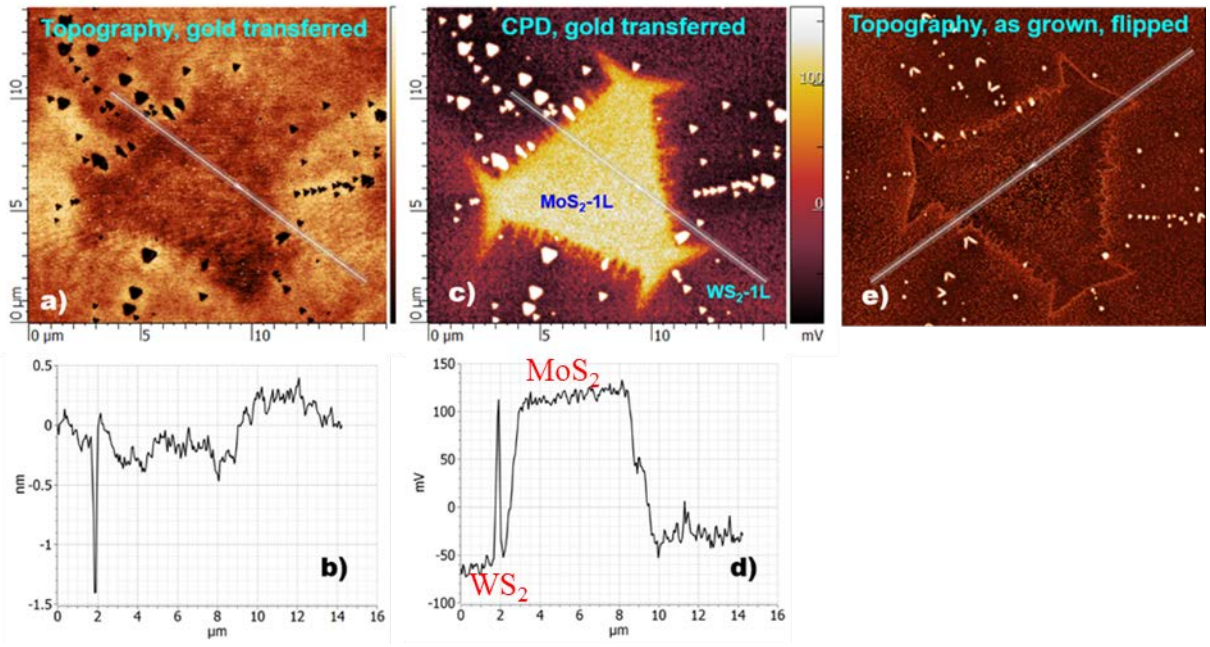

Figure 11-14. (a) topography image and same heterostructure crystal on gold substrate with corresponding height profile (c), (b) SKPFM image of same crystal and the corresponding potential profile in (d), (e) again the topography image of as grown crystal before transfer just for the close comparison.

11.3.4 Tip Enhanced Raman Spectroscopy (TERS) Characterization of MoS_2/WS_2 Heterostructure on Gold Substrate

To overcome the limitation of diffraction spot size of the probing laser light in conventional optical Raman and PL spectroscopy, TERS and TEPL was used. These techniques are based upon the principle of amplification of Raman or PL signal from the nano-sized region under the SPM tip with a high spatial resolution. In these techniques, the incident laser light on the sharp metallic nanotip creates the surface plasmons, which enhances the local electric field in the vicinity of the nanotip apex. This local electric field is further used to amplify Raman or PL signal from the nano-sized volume of a sample placed under the tip. Also, by scanning a metallic tip on the sample surface, a Raman map can be obtained with a significantly high resolution at

the nano scale level [150]. In the last few years, TERS has become a vital tool to study the spatial distribution of chemicals, interfaces, and to explore the physical or opto-electronic properties of the materials at a high spatial resolution, which was unachievable by any other conventional optical or analytical tool.

Here, MoS_2/ WS_2 lateral heterostructures are studied under the TERS characterization using two excitation laser wavelengths 638nm and 785nm. It is important to note that 638nm wavelength is in resonance with the bandgap of MoS_2, WS_2 monolayers, while 785nm is non-resonant wavelength and below the bandgap of MoS_2, WS_2 monolayers. The recorded TERS spectra and the mapping at 638nm excitation wavelength on heterostructure is shown in Figure 11-15. The TERS mapping is shown in the inset of Figure 11-15(c), which is a small section of the CPD mapping shown in Figure 11-15(a) and (b). As can be seen, the junction area in blue color between MoS_2 and WS_2 is clearly visible in TERS imaging, which was not possible under any conventional confocal Raman spectroscopy. After the collection of TERS spectra, some interesting features had been noted. First in green colored WS_2 spectra, four unusual Raman peaks had been observed at 146.5cm^{-1}, 176cm^{-1}, 200 and 215cm^{-1} as shown in Figure 11-15(e), neither of these peaks had been widely reported under normal Raman characterization [151,152,153]. However, there are few reports on these peaks and the assigned labels are ZA(M), E'(M)^{TO2}-LA(M) or LA(M), E"(M)^{TO1}-ZA(M) and E"(M)^{TO1}-TA(M) [68,154,155,156,157]. Another interesting point to be noted was the peak at 433cm^{-1}, which was not reported before.

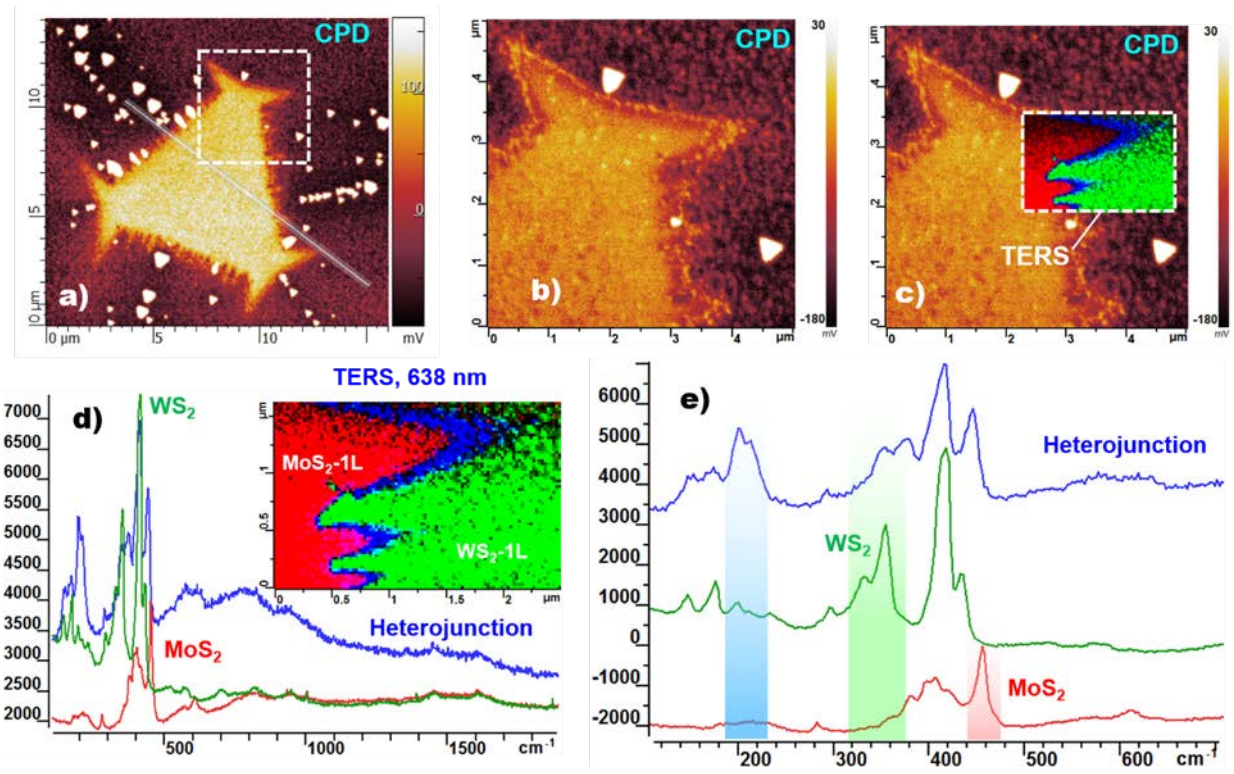

Figure 11-15: (a) CPD image of same heterostructure crystal on gold substrate, (b) Zoom in image of same crystal and (c) inset is the TERS image with a 638nm excitation, (d) collected TERS spectra at MoS_2, WS_2 and the junction, (e) Zoom in TERS spectra from 100 to 700cm^{-1}.

Monolayer MoS_2, TERS spectra is shown in red curve, which clearly exhibit the E^1_{2g} and A_{1g} peaks corresponding to monolayer nature. However, very interesting and significant peak was realized at 455cm^{-1}, which was never observed before under the normal Raman spectra. The inset image in Figure 11-15(d) is a high resolution TERS mapping image and Mapping shows the distinct regions of monolayer MoS_2 in red color and WS_2 in green and the junction boundary between them in blue color, which varied from pixel limited 25nm to few hundreds of nm. The collected TERS spectrum on the junction area is also shown in blue color. The TERS Raman peaks at the junction region is quite the same as from WS_2 monolayer and this is because of high W concentration and very low Mo atoms doped at the junction, however, few significant changes had been noted. First, the peak intensities at 200cm^{-1} and 215cm^{-1} is quite high as compared to

the intensities in WS_2. Also, the peak intensity of E^1_{2g} peak of WS_2 is very low at the junction. Second, most important point observed that the existence of new peak at 444cm^{-1}, which lies in-between WS_2 at 433cm^{-1} and MoS_2 at 455cm^{-1} peaks.

It is a common knowledge that Raman peaks are greatly influenced by both resonant and non-resonant excitation wavelengths. For instance, in TERS due to vertical electric field between metallic tip and metallic surface consists of out-of-plane vibration of surface plasmons, thus at non-resonant excitation wavelength, only out-of-plane vibrational modes of thin film should be enhanced, while at the resonant excitation, in-plane modes would also be enhanced comparatively at a certain extent. Therefore, to gain a deeper insight into the Raman modes of the heterostructures, TERS spectra should be collected at both resonant and non-resonant excitations. Therefore, here we had collected the TERS spectra and imagining of the heterostructure using a non-resonant wavelength 785nm, which is below the bandgap of both MoS_2 and WS_2 monolayers as shown in Figure 11-16.

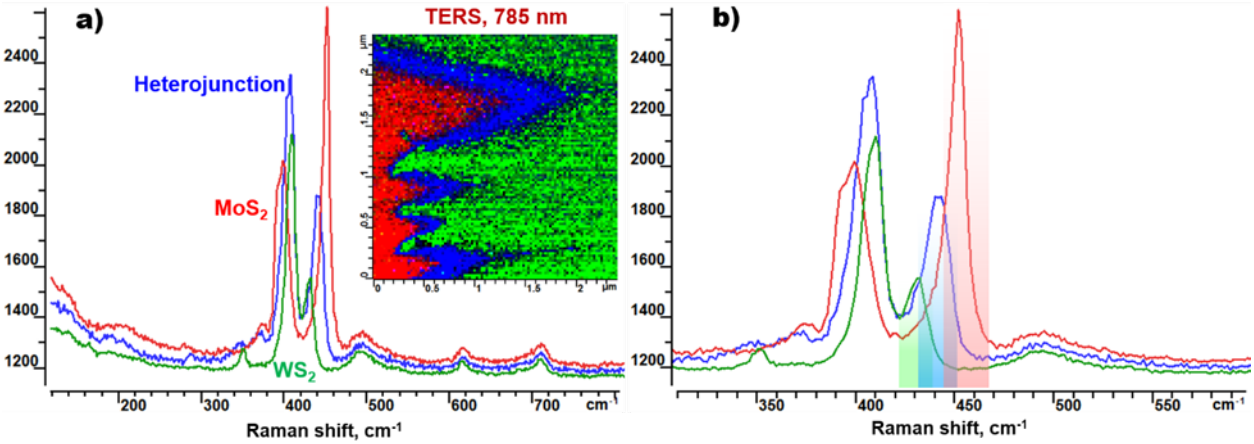

Figure 11-16: (a) TERS spectra collected at MoS_2, WS_2 and junction at non-resonant 785nm wavelength and the corresponding TERS image, (b) Zoom in TERS spectra from 300 to 600cm^{-1}

In the inset of Figure 11-16(a), TERS mapping image at 785nm excitation is shown, which is quite similar to 638nm excitation image, however, the TERS spectra on all the three different regions MoS_2, WS_2 and the junction is significantly different then the spectra at 638nm.

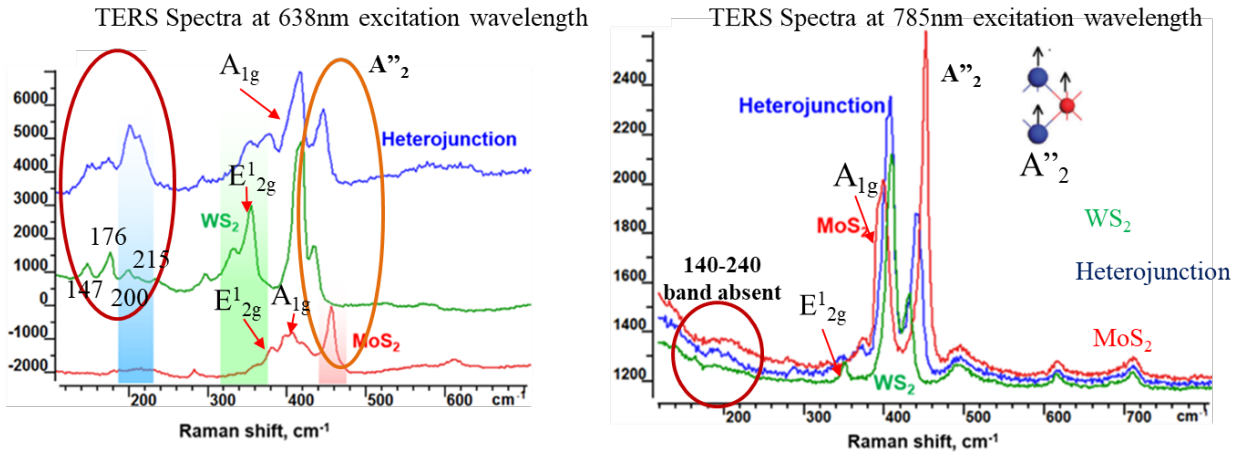

Figure 11-17: Comparison of TERS spectra at 638nm and 785nm excitation wavelengths

First to note is the absence of Raman peaks in WS_2 monolayer from 140-240cm^{-1} at 785nm excitation as shown in comparison of TERS spectra at the excitation wavelengths of 638nm and 785nm in Figure 11-17. Also, the E^1_{2g} peak was greatly reduced at non-resonant excitation. Since E^1_{2g} is an in-plane vibrational Raman mode, and the significant reduction in its intensity endorsed our view that at non-resonant 785nm excitation wavelength, only the out of plane modes will be enhanced. In-addition, out-of-plane mode A_{1g} and the unknown peak at 433cm^{-1} still exist. The TERS spectra at the junction is shown in blue curve. In this TERS spectra, E^1_{2g} peak for both WS_2 and MoS_2 is practically absent, however, A_{1g} peak was clearly noticeable. Also, the peak at 444cm^{-1} was also present.

Since the TERS at non resonant 785nm excitation wavelength is able to excite only the out-of-plane modes, which is evident by the absence of in-plane E^1_{2g} peak in WS_2, MoS_2 monolayers and the presence of only out-of-plane A_{1g} peak at 785nm excitation. Therefore, the peaks from 140-240cm^{-1} must also be in-plane modes of vibration as all these peaks are absent at 785nm

excitation but present at 638nm resonant wavelength excitation. Therefore, the earlier reported assignment of 146.5cm^{-1} to ZA(M) is clearly wrong as ZA(M) is the out-of-plane mode and otherwise must be existed at 785nm excitation. Instead, we labelled this peak as E"(M)^{TO1} – E'(LA). The mode at 200cm^{-1} is labelled as E'(M)^{LO2}–E'(LA) and the mode at 215cm^{-1} is E'(M)^{TO2}–E'(TA). All these modes were labelled by analyzing the phonon dispersion relation of WS_2 monolayers[158] shown in Figure 11-18 and extracted all the Raman peaks as mentioned in Table 4.

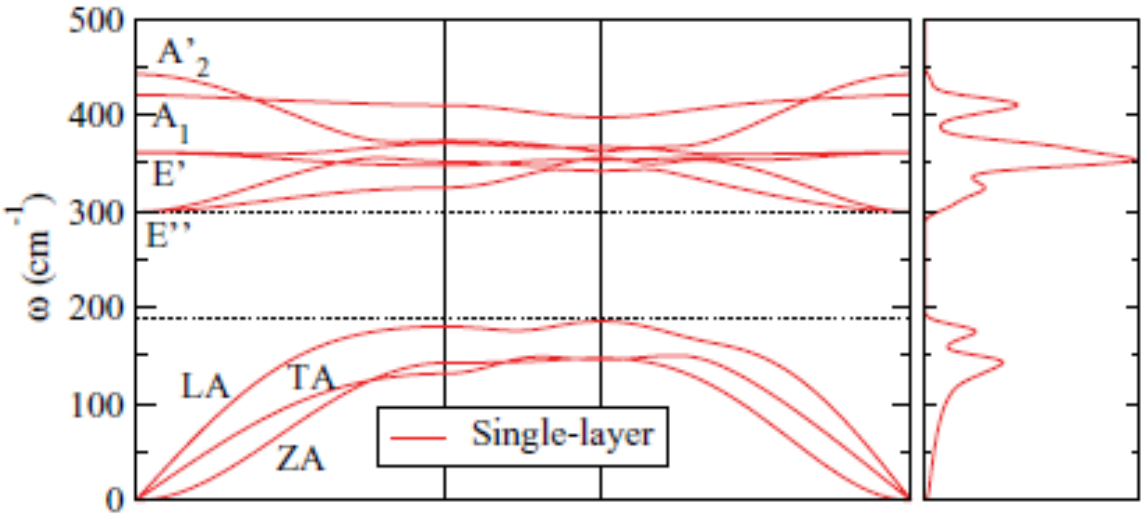

Figure 11-18: Phonon dispersion relation for WS_2 monolayer[158]

Table 4: Extracted values of Ist order Raman modes in WS_2 from the above figure.

WS2	at Γ	at M	Active		1L	
	-	133	R		E' (LA/TA)	TA
		181				LA
	-	144		IR	A2'' (ZA)	ZA
	300	326	R		E''	TO1
		354				LO1
	361	349	R,	IR	E'	TO2
		374				LO2
	442	374		IR	A2'' or A2'	ZO1
	421	412	R		A1' or A1	ZO2

Table 5: All possible combinations of 2nd order phonon Raman modes by combining single phonon modes from the above table

		IR							IR	
	WS2	MODE 2								
	at M	E'(TA)	A2" (ZA)	E'(LA)	E''(TO1)	E''(LO1)	E'(TO2)	E'(LO2)	A2''(ZO1)	A1(ZO2)
	E'(TA)	266	11	48	193	221	216	241	241	279
IR	A2" (ZA)	277	288	37	182	210	205	230	230	268
	E'(LA)	314	325	362	145	173	168	193	193	231
MODE 1	E''(TO1)	459	470	507	652	28	23	48	48	86
	E''(LO1)	487	498	535	680	708	-5	20	20	58
	E'(TO2)	482	493	530	675	703	698	25	25	63
	E'(LO2)	507	518	555	700	728	723	748	0	38
IR	A2''(ZO1)	507	518	555	700	728	723	748	748	38
	A1(ZO2)	545	556	593	738	766	761	786	786	824

Table 5 represents all the possible combinations of 2nd order Raman modes those we have calculated by adding and subtracting the Ist order Raman modes shown in Table 4. In this table, numbers in blue color represent in-plane Raman modes only, black color represent the out-of-plane Raman modes only, and the red color is for mixed (in-plane and out-of-plane) Raman

modes. For instance, all the white boxes in the diagonal is twice of the Ist order Raman mode value (2E'(TA) = 2x133 = 266cm^{-1}). Thus, from this table, possible 2nd order Raman modes for WS2 monolayers were labelled and matched with our TERS spectrum.

The complete set of TERS peaks of WS_2 monolayer and an alloyed interface is mention in Table 6. All these modes are combinations of in-plane vibrations and thus gives the sense of existence only at resonance excitation wavelength. Also, the Raman vibrational mode at 433cm^{-1} in WS_2, 455cm^{-1} in MoS_2 and at 444cm^{-1} at junction corresponds to the IR active A_2" mode. The position of this mode should be solely a function of Mo and W atoms stoichiometry ratio inside the crystal and it must shift its position as the value of Mo and W concentration changes.

Table 6: TERS peaks of shell WS_2 region and an alloyed interface region at 638nm and 785nm excitation wavelengths

WS_2 TERS peaks (cm^{-1})	Alloyed interface TERS Peaks (cm^{-1})	excitation wavelengths		Peak names	
		638nm	785nm		
147	147	Present	Absent	E"(M)^{TO1}-E'(LA) (purely in-plane)	
176	176	Present	Absent	LA(M) (purely in-plane)	
~200	~200	Present	Absent	E'(M)^{LO2}–E'(LA) (purely in-plane)	
~215	~215	Present	Absent	E'(M)^{TO2}–E'(TA) (purely in-plane)	
--	**444**	**Present**	**Present**	**A"$_2$/A$_{2u}$(Γ)**	**Position may be a function of Mo/W concentration**
433	**--**	**Present**	**Present**	**A"$_2$/A$_{2u}$(Γ)**	

*Note: M and Γ in brackets only represent that these modes exist at M and Γ positions of the phonon relation.

To explore the variation of the position of A"$_2$ mode with the change of Mo and W concentration, confocal PL spectra and the TERS spectra was collected on different alloy concentrations in $Mo_xW_{1-x}S_2$ ternary compounds as shown in Figure 11-19.

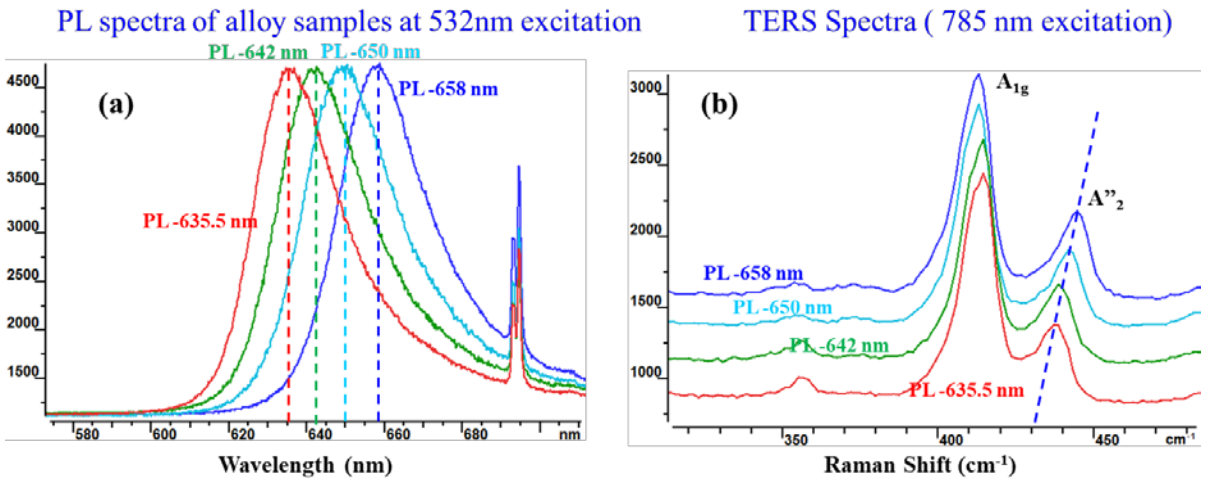

Figure 11-19: (a) Confocal PL spectra of different alloy samples at 532nm excitation, (b) TERS spectra of same positions at 785nm excitation and the variation of A"$_2$ peak position is noted.

The confocal PL peak spectra were collected using 532nm excitation wavelength and the positions of PL peaks of four different ternary alloys are 658nm, 650nm, 642nm and 635.5nm. Different PL peak positions clearly exhibit the different Mo and W compositions in these samples. Thereafter, the TERS spectra using non-resonant excitation wavelength 785nm was collected at the same locations where confocal PL spectra was taken shown in Figure 11-19(b). Clearly the red shift in A"$_2$ peak is seen as W concentration increases relative to Mo concentration. Therefore, A"$_2$ peak position is a function of Mo and W adatoms concentration and can be varied between pure WS_2 (433cm^{-1}) to pure MoS_2 (455cm^{-1}) monolayers.

Table 7: PL positions and the respective TERS spectra of various alloyed samples

PL	**658 nm**	**650 nm**	**642 nm**	**635.5 nm**
TERS (A"$_2$ peak)	**443.9 cm^{-1}**	**441.6 cm^{-1}**	**438 cm^{-1}**	**437 cm^{-1}**

The variation of TERS peak position of A"$_2$ in alloy samples with the respective PL peak positions has been clearly drawn in Table 7.

The alloyed samples used to verify the A”2 peak variation was tested under SKPFM and an AFM. The images are shown Figure 11-20.

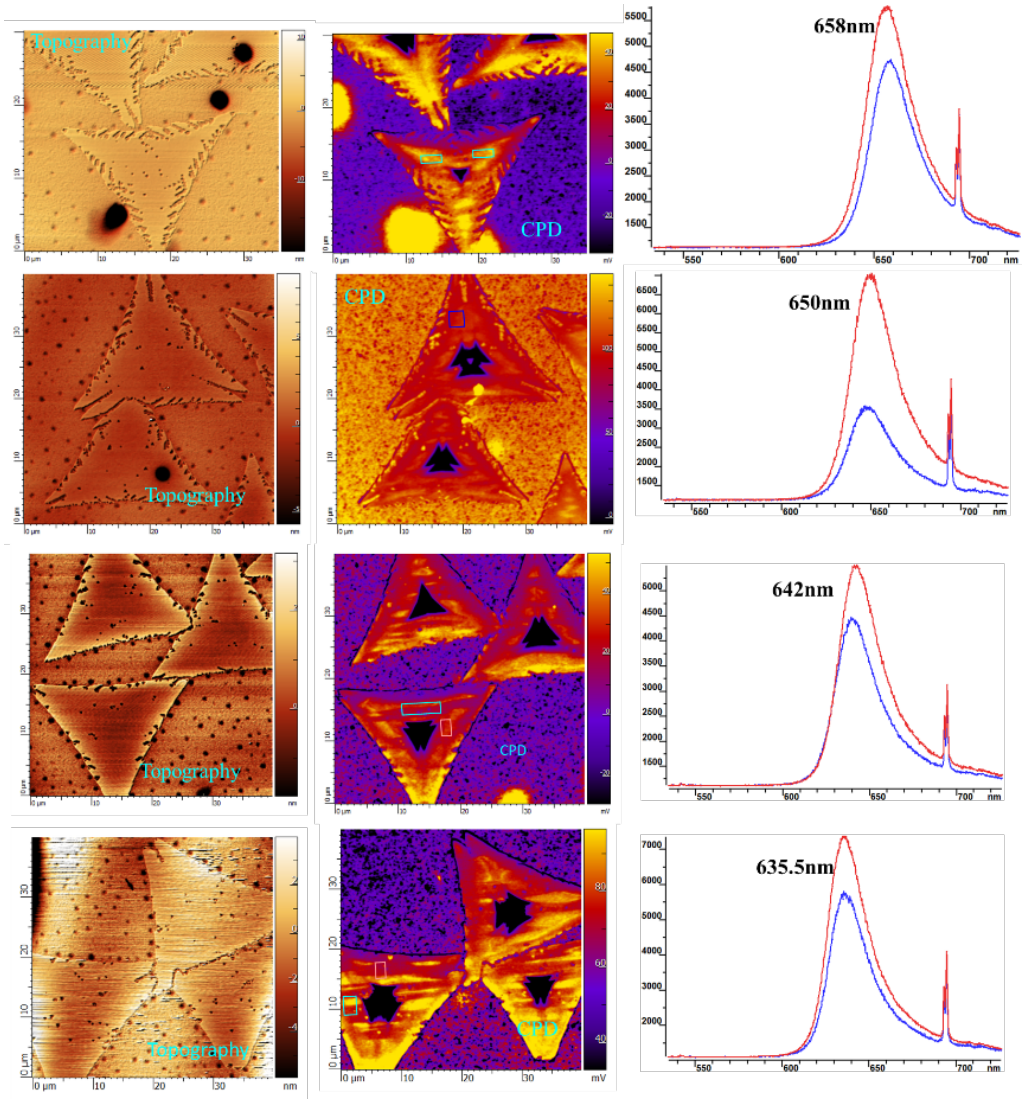

Figure 11-20: Topography and CPD images of various alloys

11.4 Experiment to Stack Vertical Heterostructures

Prior the fabrication of vertical heterostructures, PDMS stamp was synthesized. In this procedure, 10g of silicon elastomer base and 1g of silicon curing agent was mixed well for around 5 minutes and left no bubble inside the liquid solution. Poured the solution in a plane smooth petri-dish, poured quantity was small enough to make very thin layer of PDMS in petri-

dish (remember thick PDMS would not be able to lift-off monolayers). Afterwards, petri-dish was kept on horizontal surface and was letting the PDMS to dry for 48 hours at room temperature. After the assigned time, PDMS was dried and was like a rubber with a sticky in nature.

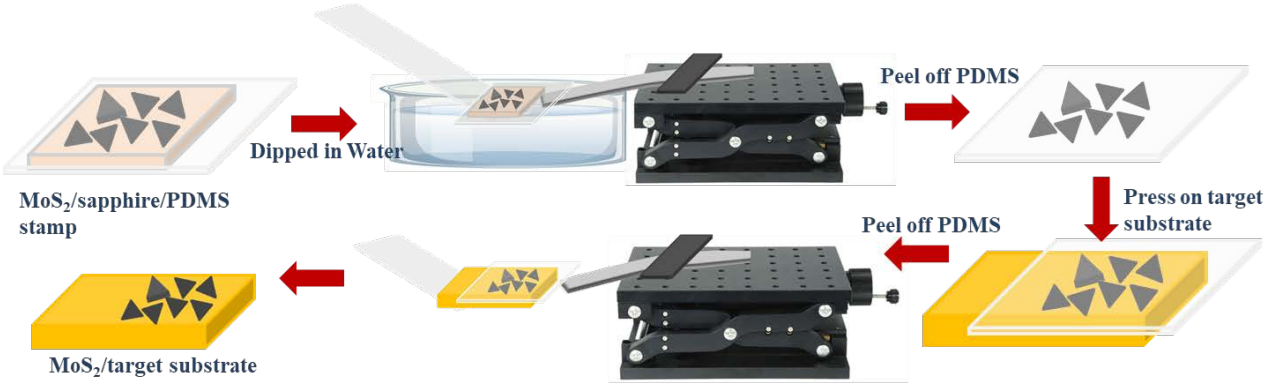

Figure 11-21: PDMS stamping process to transfer 2D materials

Stacked MoS_2/WS_2 heterostructures were prepared mechanically by PDMS stamping method as shown in Figure 11-21. Prior the preparation, MoS_2 and WS_2 monolayers were grown individually on sapphire substrate by a procedure as explained in CHAPTER 3. Now, a portion of PDMS was taken with a size slightly greater than the MoS_2 coated sapphire substrate. Bottom side of PDMS was placed on the MoS2 and was pressed hard uniformly using a flat surface. After that, small extended portion of only PDMS on PDMS/MoS_2/sapphire was glued to the mechanical motor and the rest of PDMS/MoS_2/sapphire was dipped inside water in a glass petri-dish. After 5 minutes, tried to remove very carefully and very slowly PDMS/MoS_2 from the sapphire substrate. Point was taken into consideration that due to hydrophobic nature of MoS_2, PDMS/MoS_2 should very easily be removed from the sapphire substrate. After the removal, PDMS stamp was looked yellow and sapphire substrate was quite clean transparent. Thereafter, N_2 gas was blown on the MoS2 side on PDMS/MoS_2 to remove water vapors. Now, MoS_2/PDMS was placed and pressed on WS_2 coated sapphire substrate followed by heating on a

hot plate at 100ºC for 5 minutes to remove excess water vapors. Following this, PDMS/MoS_2/WS_2/sapphire was sticked on the glass slide and the same extended portion of bare PDMS was sticked to mechanical motor using a double-sided scotch tape. Now, extremely slowly PDMS was lift off (total time taken was ~20-30minutes) after resting MoS_2 triangles on top of WS_2 triangles.

11.5 Results and Discussion

11.5.1 Optical Characterization of stacked regions of vertical $MoS_2/Mo_xW_{1-x}S_2$ Heterostructure

The stacked heterostructures are displayed in an optical microscope images in Figure 11-22. The optical contrast between individual monolayers and a bilayer region is clearly visible.

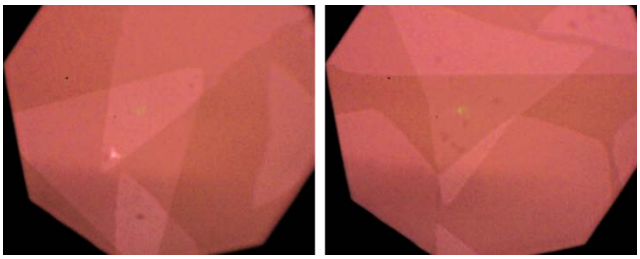

Figure 11-22. Optical microscope images of stacked $MoS_2/Mo_xW_{1-x}S_2$ heterostructure

A typical Raman spectrum of MoS_2 monolayer, $Mo_xW_{1-x}S_2$ alloy and stacked bilayer $MoS_2/Mo_xW_{1-x}S_2$ is illustrated in Figure 11-23 at the colored points shown in optical images. Raman spectra was recorded using 532nm incident laser light at room temperature. In MoS_2 Raman spectrum shown in blue curve and the peaks were observed at 384.5cm^{-1} and 404.7cm^{-1}, which corresponds to typical vibrational modes E^1_{2g} and A_{1g} of MoS_2 monolayer. The Raman spectrum of an alloy $Mo_xW_{1-x}S_2$ in red color exhibit four Raman peaks at 353.2cm^{-1} (consist of 2LA(M) and E^1_{2g}), 379.5cm^{-1}, 397.6cm^{-1} and 417.7cm^{-1}, respectively. The Raman peaks at 353.2cm^{-1} and 417.7cm^{-1} are WS_2 monolayer, and the peaks at 379.5cm^{-1} and 397.6cm^{-1} are the red shifted MoS_2 monolayer peaks due to strain. The stacked hetero-bilayer Raman is shown in

yellow curve. Although its Raman spectrum is an almost a superposition of the spectra of individual MoS_2 and an alloy monolayer, however, the point to note here is that in stacked bilayer Raman spectra, MoS_2 peaks are quite broad. It is because MoS_2 peaks are comprised of both strained and unstrained MoS_2 Raman peaks (strained peaks from an alloy and unstrained from pure MoS_2 monolayer)

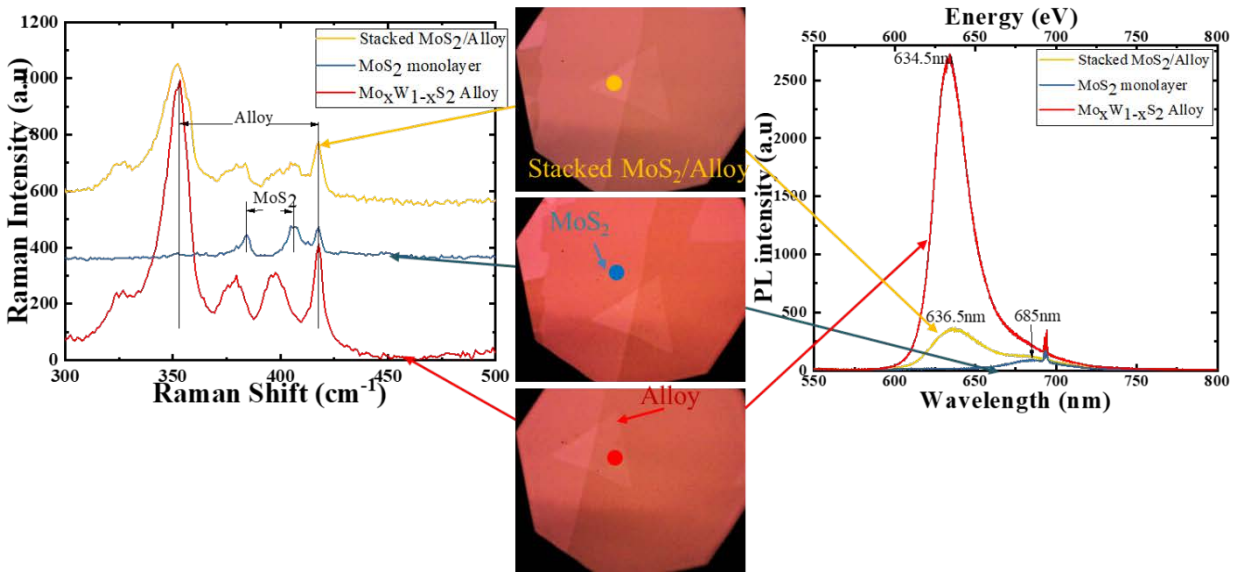

Figure 11-23: Left, Raman spectra and right PL spectra at the colored points on an optical images at 532nm excitation wavelength

In order to obtain the information regarding bandgaps of stacked hetero-bilayer, MoS2 and alloy monolayer. Micro-Photoluminescence (PL) spectroscopy was conducted at the same colored spots in optical images where Raman spectrum was taken as shown in Figure 11-23 using a 532nm green laser at room temperature. PL spectra was collected from MoS_2, alloy MLs, together from the stacked hetero-bilayer $MoS_2/Mo_xW_{1-x}S_2$. $Mo_xW_{1-x}S_2$ alloy showed strong PL peak at 633nm and MoS_2 monolayer PL peak occurred at 685nm, respectively, these PL peaks are due to the recombination of respective A excitons. However, in stacked bilayer, both PL peaks from $Mo_xW_{1-x}S_2$ alloy and MoS_2 are visible in addition to the largely suppressed alloyed

PL peak. The PL quenching of formed intralayer excitons in hetero-bilayers was largely reported in several publications[159,160,161]. It has been explained by the charge separation principle. The electrons and holes in the formed intralayer excitons in individual MoS_2 and $Mo_xW_{1-x}S_2$ layers are get separated because of the type II heterostructure nature of the stacked hetero-bilayer. In this type II heterostructure for instance, holes get transferred towards $Mo_xW_{1-x}S_2$ monolayer alloy and electrons towards the MoS_2 monolayer. Therefore, in the end, interlayer excitons are formed with electrons reside in MoS_2 layer and holes reside in $Mo_xW_{1-x}S_2$ layer. The sharp peak had also been observed around 700nm, which was due to pre-doped Cr^{+3} ions in sapphire substrate.

PL mapping image and the spectra at three different spots was also captured as shown in Figure 11-24. The collected spectra at the colored spots clearly exhibit PL peaks of MoS_2 and $Mo_xW_{1-x}S_2$ monolayer alloy, together with the PL peaks from stacked hetero-bilayer. Here also, the alloyed PL peak in stacked structure was red shifted by 3nm (~10meV) as compared to individual alloy layer. The mapping was done with the selected 636nm emission wavelength by the detector, which corresponds to alloyed PL peak and the final image showed only the alloyed monolayer with the intensity distribution. It showed high intensity at the edges of the triangle as compared to low intensity at the center.

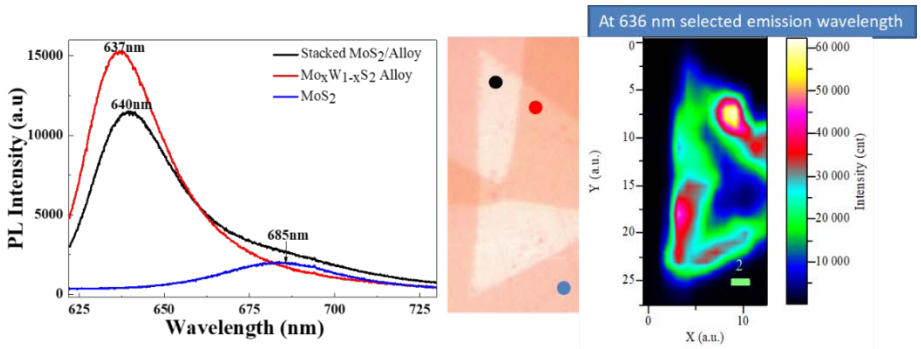

Figure 11-24: PL spectra collected colored points of VHS and PL mapping image at 636nm emission wavelength

Similarly, Raman mapping was done and the spectra was collected on the colored spots shown in Figure 11-25. In the Raman mapping, images were scanned by selecting 385cm^{-1}, 407cm^{-1} Raman peaks corresponds to MoS_2 and 417cm^{-1}, which corresponds to alloy WS_2 peak. Therefore, the final mapped images clearly showed the bigger layer is pure MoS_2 stacked on top of the pure alloyed monolayer.

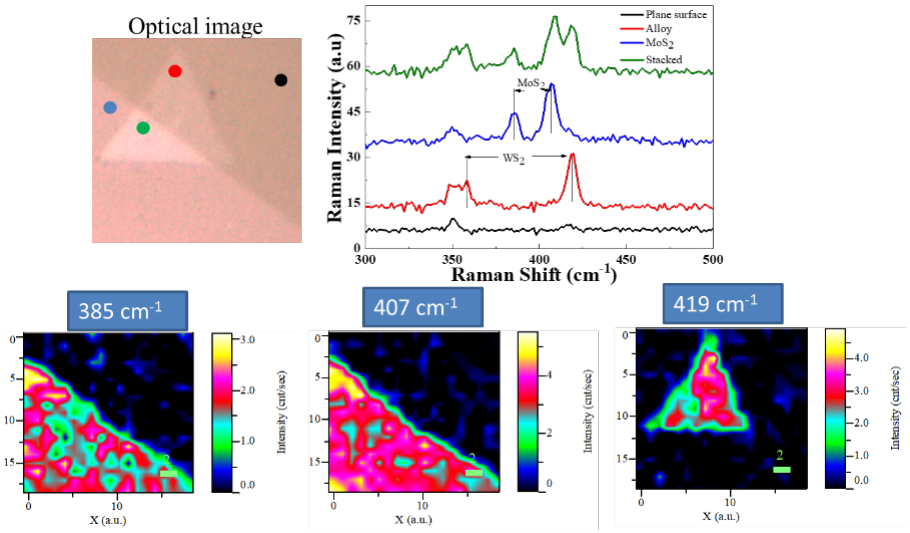

Figure 11-25: Optical image of VHS with the corresponding Raman spectra at the colored points shown in an optical image and also the Raman mapping image at MoS_2 peaks 385cm^{-1}, 407cm^{-1} also at WS_2 peak 419cm^{-1}.

CHAPTER 12.
SUMMARY AND CONCLUSION

This thesis includes the experimental method to synthesize atomically thick MoS_2 monolayer and deep characterization techniques to investigate the electronic and optical properties. The whole thesis is divided into two sections. Section I in this dissertation focused on the synthesis of a large area of high quality MoS_2 monolayer on various substrates. The most conventional defect analysis characterization techniques are also introduced in this section. This section also includes the electron transport properties of MoS_2 monolayer and the sensing ability of grown flakes. Noise measurement is a very formidable task in any device, thus this section also includes the various types of noises and their measurements. Section II in this dissertation discusses the synthesis of most complex $Mo_{1-x}W_xS_2$ ternary alloys and MoS_2/WS_2 lateral heterostructures. Study of Raman modes of vibrations at MoS_2, WS_2 and at the junction is clearly illustrated and brings some unknown modes into the light.

12.1 Section I Summary

Low pressure CVD is the one of the most versatile and simplest techniques to synthesize high quality MoS_2 monolayers and to understand the growth mechanism. The MoS_2 monolayer growth process was developed on sapphire substrate and temperature effect was studied for yield enhancement of monolayers in CHAPTER 3. The in-depth optical characterization was done to understand the monolayer nature and the comparison of Raman peaks was done for monolayer,

bilayer and bulk MoS2. The specific area growth of MoS2 monolayers was conducted on patterned 5nm SiO2 circles of various sizes on sapphire substrate in CHAPTER 4. The same growth method was conducted on various oxide thick SiO2/Si substrates and was characterized thoroughly in CHAPTER 5. GaN is a semiconducting substrate and with the same lattice constant as MoS_2 monolayers. Thus, growth of MoS_2 was conducted on GaN substrates and was characterized optically and the strain generated on MoS_2 monolayers due to substrate in CHAPTER 6. In an another study of MoS_2 on Ga_2O_3, the effect of high dielectric constant of insulator Ga_2O_3 material on the MoS2 PL can be seen and was elaborated in CHAPTER 7. The electron transport nature of semiconducting MoS_2 monolayer was explored in CHAPTER 8 through the study of I-V characteristics. Photoconductor's responsivity and the effect of incident power density was studied. The gas sensing behavior of MoS_2 monolayer was also studied through the exposure of an MoS_2 device to electron rich CO_2 gas. Different concentrations of CO_2 gas were exposed and a subsequent rise in the dark current was noted. Noise in any type of device is very significant to study especially at low frequencies to measure the true sensitivity of the device. In CHAPTER 9, 1/f noise theory was studied, noise spectrum density was calculated and further the true value of specific detectivity was calculated.

12.2 Section I Conclusion

Findings from the optimization of the growth parameters of 2D MoS_2 monolayers is that the growth temperature should be high enough to enhance the vapor pressure of the precursor on top of the substrate. The right optimum temperature was achieved by analyzing the increase in the flake size with the increase in the precursor temperature. In our case, 970ºC is the precursor temperature and 800ºC is the growth temperature to receive large sized triangular flakes (~100μm) and thin film area around few mm^2. The grown MoS_2 flakes were optically characterized using Raman and photoluminescence spectroscopy using 532nm excitation

wavelength. The clear change in separation in the in-plane and out-of-plane Raman modes are seen with the MoS_2 thickness changes from single layer to bulk. Intense emission peak ~1.84eV in the photoluminescence study further endorse the existence of single layer MoS_2 on sapphire substrate. In MoS_2 monolayer, K and K' points in the Brillion Zone are not the same because of the center of symmetry breaking, thus, they can selectively be excited by right or left circular polarization excitation wavelengths and can gain net polarization from the MoS_2 monolayers. On the study of growth of MoS2 on different substrates (sapphire, SiO_2, GaN and Ga_2O_3), MoS_2 crystals on GaN are oriented in specific directions due to the fact that both MoS_2 and GaN have the same crystal symmetry with almost the same lattice constant. On the AFM measurement of MoS_2 on GaN, MoS_2 step height was not detected as was detected on sapphire substrate in the height mode but was clearly observed in the phase mode. Therefore, it is speculated that perhaps MoS_2 monolayers are embedded inside the GaN substrate during the growth, however, we are limited by suitable characterization to further support our observation. In the MoS_2/Ga_2O_3, the large dielectric constant ~18 of Ga_2O_3 is clearly observed in the blue shift in PL emission peak of MoS_2 as compared to sapphire and silicon. This blue shift is due to the quantum confinement of excitons inside MoS_2. High dielectric constant of the substrate causes less interaction of the formed excitons in MoS_2 with the trap states between MoS_2 and the substrate which leads to the enhancement of exciton energy and hence the occurrence of blue shift in the emission peak. The I-V characteristics study of MoS_2 monolayers explains the formation of ohmic contacts with Ti/Ag metal electrodes. It is due to the large work-function of Ti/Ag metal as compared to MoS_2 monolayer, which results in the lowering of MoS_2 fermi level to align with the metals fermi level and hence the formation of ohmic contacts. Carbon dioxide is an electron donor gas and as the gas was exposed to the MoS_2 device, gas molecules adsorb on the MoS_2 monolayer.

Subsequently, a sudden rise in the current in MoS_2 illustrates the rise in electrons reaching the electrodes. This happens by the transfer of electrons from the lone pair of oxygen molecules to MoS_2 conduction band and hence more electrons flow and increase in current. A minimum concentration of detected CO_2 gas was 200ppm. I observed that after the gas was switched off, an increased current takes infinite amount of time to reach its initial current. This may be due to gas molecules still staying adsorbed on the MoS_2 monolayer. This issue can be resolved by heating the MoS_2 device to around 60ºC-70ºC[162]. It will desorb CO_2 molecules more quickly and hence the sensor will reach its initial current value in minimum time.

12.3 Section II Summary

Section II in this dissertation deals with the $Mo_{1-x}W_xS_2$ ternary alloys, lateral and vertical heterostructures. The LPCVD was used for one step growth of these compounds, however, for the synthesis of vertical MoS_2/WS_2 heterostructures, PDMS based transfer process was developed, in which MoS_2 monolayers were mechanically transferred on WS_2 monolayers. MoS_2 based ternary compounds have been discussed in detail in CHAPTER 10. In this chapter, different concentrations of W were infused in-situ in MoS_2 monolayers during the growth and results in $Mo_{1-x}W_xS_2$ monolayers on sapphire substrate. Optical characterization which includes micro Raman and micro-photoluminescence was systematically done to explore the change in Raman peaks from MoS_2 to WS_2 and the change in PL emission peak as well. CHAPTER 11 is solely based upon the heterostructures (lateral and vertical). Lateral heterostructures were synthesized using pure MoS_2 and WS_2 powder precursors in LPCVD. These LHS were characterized using SEM, confocal optical microscope, and AFM to study the topography. Raman and PL characterization was performed at three regions: core, shell and at junction using 532nm excitation wavelength. The presence of all the Raman peaks of MoS_2 and WS_2 at the junction had clearly demonstrated the transition region. In PL measurement at the junction, the

PL emission peak at 636nm was detected, which is attributed to the $Mo_{1-x}W_xS_2$ type transition region. In order to further investigate the transition region, TERS was performed using 638nm and 785nm excitation wavelengths. The excitation wavelength 638nm is in resonance with the bandgaps of MoS_2 and WS_2, however, 785nm is in non-resonance condition. WS_2 Raman modes between 140-230cm^{-1} were observed only when excited by 638nm wavelength but were absent at 785nm wavelength. In addition, a strange Raman mode had been observed at 433cm^{-1} in WS_2, 444cm^{-1} in junction region and at 455cm^{-1} in MoS_2 monolayer region. These modes were a function of the stoichiometric ratio of Mo or W atoms concentration in the monolayer, thus shift in the 444cm^{-1} peak had been observed on different ternary compounds.

In this section, vertically stacked MoS_2/WS_2 heterostructures are also studied, which were synthesized by PDMS transfer process. Collected Raman spectra from the WS_2 region elucidated the existence of impure WS_2 monolayer, and the ternary nature was seen by the existence of a PL peak at 634.5nm, rather than a pure PL peak at ~624nm. Therefore, the stacked structure was vertical $MoS_2/Mo_{1-x}W_xS_2$ heterostructure. The significant decrease in PL at the bilayer stacked region signaled towards the formation of interlayer exciton.

12.4 Section II Conclusion

The different concentrations of W atoms in MoS_2 monolayers leads to the change in the bandgap. Thus, bandgap can be tuned between MoS_2 to WS_2 monolayers by varying the Mo and W stoichiometric ratio. The slightest red shift of MoS_2 monolayer Raman modes in ternary alloy as compared to pure MoS_2 monolayer is due to the existence of strain. The transition region in the lateral MoS_2/WS_2 heterostructures is a ternary alloy with a bandgap of ~636nm. The minimum width of the transition region found out to be pixel limited 25nm by TERS characterization. In the TERS spectra, at non resonant excitation, only out-of-plane modes are noticed, but at resonant excitation, in-plane modes are also observed. Thus, in WS_2 monolayer, Raman modes

between 140-230cm^{-1} only existed when excited at resonant (638nm) wavelength, however, these modes were absent at non resonant 785nm excitation. It illustrates that these modes are in-plane modes of vibration, while the other mode at 433cm^{-1} is the out-of-plane Raman mode. The position of Raman mode at 433cm^{-1} in WS_2, 444cm^{-1} in junction and at 455cm^{-1} in MoS_2 conclude that this mode is a function of Mo and W atoms and labelled it as an IR active A_2''.

In vertically stacked $MoS_2/Mo_{1-x}W_xS_2$ heterostructure, a significant decrease in the PL intensity had been observed at the stacked bilayer region. This decrease of PL cannot be attributed to the formation of indirect bandgap at hetero-bilayer region because otherwise MoS_2 A_{1g} Raman peak should be blue shifted from 404.5cm^{-1} to 406cm^{-1}. This decrease of PL happens only because of the formation of interlayer excitons with electrons accumulated in the MoS_2 conduction band and holes accumulated in the WS_2 valance band. A PL mapping image was collected at 636nm emission wavelength and clearly shows the stacked layer is ternary monolayer alloy.

REFERENCES

[1] Z. Q. Wang, T. Y Lü, H. Q. Wang, Y. P. Feng, J. C. Zheng. Review of borophene and its potential applications. Front. Phys. (2019), 14, 3, 33403.

[2] A. J. Mannix, Z. Zhang, N. P. Guisinger, B. I. Yakobson and M. C. Hersam. Borophene as a prototype for synthetic 2D materials development. Nature Nanotechnology (2018), 13, 444–450.

[3] N. Liu, G. Bo, Y. Liu, X. Xu, Y. Du and S. X. Dou. Recent Progress on Germanene and Functionalized Germanene: Preparation, Characterizations, Applications, and Challenges. Small (2019), 15, 1805147.

[4] A. Acun, L. Zhang, P. Bampoulis, M. Farmanbar, A. V. Houselt, A. N. Rudenko, M. Lingenfelder, G. Brocks, B Poelsema, M. I. Katsnelson and H. J. W. Zandvliet. Germanene: the germanium analogue of graphene. J. Phys.: Condens. Matter (2015), 27, 443002.

[5] M. E. Dávila and G. L. Lay. Few layer epitaxial germanene: a novel two-dimensional Dirac material. Scientific Reports (2016), 6, 20714.

[6] M. Akhtar, G. Anderson, R. Zhao, A. Alruqi, J. E. Mroczkowska, G. Sumanasekera and J. B. Jasinski. Recent advances in synthesis, properties, and applications of phosphorene. npj 2D Materials and Applications (2017), 5.

[7] L. Kou, C. Chen and S. C. Smith. Phosphorene: Fabrication, Properties, and Applications. J. Phys. Chem. Lett. (2015), 6, 2794−2805.

[8] C. Grazianetti, E. Cinquanta and A. Molle. Two-dimensional silicon: the advent of silicone. 2D Mater. (2016), 3, 012001.

[9] Y. An, Y. Tian, C. Wei, Y. Zhang, S. Xiong, J. Feng and Y. Qian. Recent advances and perspectives of 2D silicon: Synthesis and applicationfor energy storage and conversion. Energy Storage Materials (2020), 32, 115–150116.

[10] M. Khazaeia, A. Mishra, N. S.Venkataramanan, A. K.Singh, S.Yunoki. Recent advances in MXenes: From fundamentals to applications. Current Opinion in Solid State & Materials Science (2019), 23, 164–178.

[11] Y. Gogotsi and B. Anasori. The Rise of MXenes. ACS Nano (2019), 13, 8, 8491–8494.

[12] H. Kwon, S. Garg, J. H. Park, Y. Jeong, S. Yu, S. M. Kim, P. Kung and S. Im. Monolayer MoS2 field-effect transistors patterned by photolithography for active matrix pixels in organic light-emitting diodes. npj 2D Materials and Applications (2019), 9.

[13] L. E. Strange, J. Yadav, S. Garg, P. S. Shinde, J. W. Hill, C. M. Hill, P. Kung and S. Pan. Investigating the Redox Properties of Two-Dimensional MoS2 Using Photoluminescence Spectroelectrochemistry and Scanning Electrochemical Cell Microscopy. Phys. Chem. Lett. (2020), 11, 3488−3494.

[14] H. Y. Chang , M. N. Yogeesh, R. Ghosh , A. Rai, A. Sanne, S. Yang, N. Lu, S. K. Banerjee and D. Akinwande. Large-Area Monolayer MoS2 for Flexible Low-Power RF Nanoelectronics in the GHz Regime. Adv. Mater. (2016), 28, 1818–1823.

[15] M. L. Tsai, S. H. Su, J. K. Chang, D. S. Tsai, C. H. Chen, C. I. Wu, L. J. Li, L. J. Chen and J. H. He. Monolayer MoS2 Heterojunction Solar Cells. ACS Nano (2014), 8, 8, 8317-8322.

[16] H. R. Gutierrez, N. P. Lopez, A. L. Elías, A. Berkdemir, B. Wang, R. Lv, F. L. Urías, V. H. Crespi, H. Terrones and M. Terrones. Extraordinary Room-Temperature Photo-luminescence in Triangular WS2 Monolayers. Nano Lett. (2013), 13, 3447−3454.

[17] B. Zhu, X. Chen and X. Cui. Exciton Binding Energy of Monolayer WS2. Scientific Reports (2015), 5, 9218.

[18] A. Splendiani, L. Sun, Y. Zhang, T. Li, J. Kim, C. Y. Chim, G. Galli and F. Wang. Emerging Photoluminescence in Monolayer MoS2. Nano Lett. (2010), 10, 1271–1275.

[19] M. Chhowalla, H. S. Shin, G. Eda, L. J. Li, K. P. Loh and H. Zhang. The chemistry of two-dimensional layered transition metal dichalcogenide nanosheets. Nature Chemistry (2013), 5.

[20] J. Kim, C. Jin, B. Chen, H. Cai, T. Zhao, P. Lee, S. Kahn, K. Watanabe, T. Taniguchi, S. Tongay, M. F. Crommie, F. Wang. Observation of ultralong valley lifetime in WSe2/MoS2 heterostructures. Sci. Adv. (2017), 3, e1700518.

[21] A. D. Franklin. Nanomaterials in transistors: From high-performance to thin-film applications. Science (2015), 349, 6249.

[22] K. S. Novoselov, A. Mishchenko, A. Carvalho, A. H. C. Neto. 2D materials and van der Waals heterostructures. Science (2016), 353, 6298.

[23] K. F. Mak and J. Shan. Photonics and optoelectronics of 2D semiconductor transition metal dichalcogenides. Nature Photonics (2016), 10, 216-226.

[24] X. Liu and M. C. Hersam. Interface Characterization and Control of 2D Materials and Heterostructures. Adv. Mater. (2018), 30, 1801586.

[25] L. Gao. Flexible Device Applications of 2D Semiconductors. Small (2017), 13, 1603994.

[26] T. Mueller and E. Malic. Exciton physics and device application of two-dimensional transition metal dichalcogenide semiconductors. npj 2D Materials and Applications (2018) 29.

[27] B. Radisavljevic, A. Radenovic, J. Brivio, V. Giacometti and A. Kis. Single-layer MoS2 transistors. Nature Nanotechnology (2011), 6, 147-150.

[28] K. C. Chiu, X. Q. Zhang, X. Liu, V. M. Menon, Y. F. Chen, J. M. Wu and Y. H. Lee. Synthesis and Application of Monolayer Semiconductors. IEEE Journal Of Quantum Electronics (2015), 51, 10.

[29] Z. Hea and W. Que. Molybdenum disulfide nanomaterials: Structures, properties, synthesis and recent progress on hydrogen evolution reaction. Applied Materials Today (2016), 3, 23–56.

[30] W. Zhao, J. Pan, Y. Fang, X. Che, D. Wang, K. Bu and F. Huang. Metastable MoS2: Crystal Structure, Electronic Band Structure, Synthetic Approach and Intriguing Physical Properties. Chem. Eur. J. (2018), 24, 15942 – 15954.

[31] N. Jena, Dimple, S. D. Behere and A. D. Sarkar. Strain-Induced Optimization of Nanoelectromechanical Energy Harvesting and Nanopiezotronic Response in a MoS2 Monolayer Nanosheet. J. Phys. Chem. C (2017), 121, 9181−9190.

[32] Y. C. Lin, H. P. Komsa, C. H. Yeh, T. Bjorkman, Z. Y. Liang, C. H. Ho, Y. S. Huang, P. W. Chiu, A. V. Krasheninnikov and K. Suenaga. Single-Layer ReS2: Two-Dimensional Semiconductor with Tunable In-Plane Anisotropy. ACS Nano (2015), 9, 11, 11249-11257.

[33] M. Rahman, K. Davey and S. Z. Qiao. Advent of 2D Rhenium Disulfide (ReS2): Fundamentals to Applications. Adv. Funct. Mater. (2017), 27, 1606129.

[34] K. Kang, S. Xie, L. Huang, Y. Han, P. Y. Huang, K. F. Mak, C. J. Kim, D. Muller and J. Park. High-mobility three-atom-thick semiconducting films with wafer-scale homogeneity. Nature (2015), 520, 656-660.

[35] X. Zhu, X. Ji, N. Kong, Y. Chen, M. Mahmoudi, X. Xu, L Ding, W. Tao, T. Cai, Y. Li, T. Gan, A. Barrett, Z. Bharwani, H. Chen and O. C. Farokhzad. Intracellular Mechanistic Understanding of 2D MoS2 Nanosheets for Anti-Exocytosis-Enhanced Synergistic Cancer Therapy. ACS Nano (2018), 12, 2922−2938.

[36] A. Splendiani, L. Sun, Y. Zhang, T. Li, J. Kim, C. Y. Chim, G. Galli and F. Wang. Emerging Photoluminescence in Monolayer MoS2. Nano Lett. 2010, 10, 1271–1275.

[37] A. Ramasubramaniam. Tunable band gaps in bilayer transition-metal dichalcogenides. Physical Review B (2011), 84, 205325.

[38] H. R. Gutiérrez, N. P. López, A. L. Elías, A. Berkdemir, B. Wang, R. Lv, F. L. Urías, V. H. Crespi, H. Terrones and M. Terrones. Extraordinary Room-Temperature Photo-luminescence in Triangular WS2 Monolayers. Nano Lett. (2013), 13, 3447−3454.

[39] W. Melitz, J. Shena, A. C. Kummela, S. Lee. Kelvin probe force microscopy and its application. Surface Science Reports (2011), 66, 1–27.

[40] P. Verma. Tip-Enhanced Raman Spectroscopy: Technique and Recent Advances. Chem. Rev. (2017), 117, 6447−6466.

[41] T. Han, H. Liu, S. Wang, W. Li, S. Chen, X. Yang and M. Cai. Research on the Factors Affecting the Growth of Large-Size Monolayer MoS2 by APCVD. Materials (2018), 11, 2562.

[42] Y. Xie, Z. Wang, Y. Zhan, P. Zhang, R. Wu, T. Jiang, S. Wu, H. Wang, Y. Zhao, T. Nan and X. Ma. Controllable growth of monolayer MoS2 by chemical vapor deposition via close MoO2 precursor for electrical and optical applications. Nanotechnology (2017), 28, 084001.

[43] F. Chen and W. Su. The effect of the experimental parameters on the growth of MoS2 flakes. Cryst Eng Comm. (2018), 20, 4823.

[44] J. Y. Chen, L. Liu, C. X. Li and J. P. Xu. Chemical Vapor Deposition Growth of Large-Area Monolayer MoS2 and Fabrication of Relevant Back-Gated Transistor. CHIN. PHYS. LETT. (2019), 36, 3, 037301.

[45] K. F. Mak, C. Lee, J. Hone, J. Shan and T. F. Heinz. Atomically Thin MoS2: A New Direct-Gap Semiconductor. PRL (2010), 105, 136805.

[46] V. Senthilkumar, L. C. Tam, Y. Soo Kim, Y. Sim, M. J. Seong, and J. I. Jang. Direct vapor phase growth process and robust photoluminescence properties of large area MoS2 layers. Nano Research (2014), 7, 12, 1759–1768.

[47] A. M. Zande, P. Y. Huang, D. A. Chenet, T. C. Berkelbach, Y. You, G. H. Lee, T. F. Heinz, D. R. Reichman, D. A. Muller and J. C. Hone. Grains and grain boundaries in highly crystalline monolayer molybdenum disulphide. Nature Materials (2013), 12.

[48] X. Ling, Y. H. Lee, Y. Lin, W. Fang, L. Yu, M. S. Dresselhaus and Jing Kong. Role of the Seeding Promoter in MoS2 Growth by Chemical Vapor Deposition. | Nano Lett. (2014), 14, 464−472 .

[49] A. C. Gomez, R. Roldan, E. Cappelluti, M. Buscema, F. Guinea, H. S. J. Zant and G. A. Steele. Local Strain Engineering in Atomically Thin MoS2. | Nano Lett. 2013, 13, 5361−5366.

[50] L. Yang, X. Cui, J. Zhang, K.Wang, M. Shen, S Zeng, S. A. Dayeh, L. Feng and B. Xiang. Lattice strain effects on the optical properties of MoS2 nanosheets. Scientific Reports (2014), 4, 5649.

[51] Z. Liu, M. Amani, S. Najmaei, Q. Xu, X. Zou, W. Zhou, T. Yu, C. Qiu, A. G. Birdwell, F. J. Crowne, R. Vajtai, B. I. Yakobson, Z. Xia, M. Dubey, P. M. Ajayan and J. Lou. Strain

and structure heterogeneity in MoS2 atomic layers grown by chemical vapour deposition. Nature Communications (2014), 5, 5246.

[52] H. Bergeron, V. K. Sangwan, J. J. McMorrow, G. P. Campbell, I. Balla, X. Liu, M. J. Bedzyk, T. J. Marks and M. C. Hersam. Chemical Vapor Deposition of Monolayer MoS2 Directly on Ultrathin Al2O3 for Low-Power Electronics. Appl. Phys. Lett. (2017), 110, 053101.

[53] K. K. Liu, W. Zhang, Y. H. Lee, Y. C. Lin, M. T. Chang, C. Y. Su, C. S. Chang, H. Li, Y. Shi, H. Zhang, C. S. Lai and L. J. Li. Growth of Large-Area and Highly Crystalline MoS2 Thin Layers on Insulating Substrates. Nano Lett. (2012), 12, 1538−1544.

[54] Y. K. Lin, R. S. Chen, T. C. Chou, Y. H. Lee, Y. F. Chen, K. H. Chen and L. C. Chen. Thickness-Dependent Binding Energy Shift in Few-Layer MoS2 Grown by Chemical Vapor Deposition. ACS Appl. Mater. Interfaces (2016), 8, 22637−22646.

[55] R. G. Dickinson and L. Pauling. The Crystal Structure of Molybdenite. J. Am. Chem. Soc. (1923), 45, 6, 1466-1471.

[56] R. Addou, L. Colombo and R. M. Wallace. Surface Defects on Natural MoS2. ACS Appl. Mater. Interfaces (2015), 7, 11921−11929

[57] S. Wang, Y. Rong, Y. Fan, M. Pacios, H. Bhaskaran, K. He and J. H. Warner. Shape Evolution of Monolayer MoS2 Crystals Grown by Chemical Vapor Deposition. Chem. Mater. (2014), 26, 22, 6371-6379.

[58] P. Chen, W. Xu, Y. Gao, J. H. Warner and M. R. Castell. Epitaxial Growth of Monolayer MoS2 on SrTiO3 Single Crystal Substrates for Applications in Nanoelectronics. ACS Appl. Nano Mater. (2018), 1, 6976−6988.

[59] R. Soklaski, Y. Liang, and L. Yang. Temperature effect on optical spectra of monolayer molybdenum disulfide. Applied Physics Letters (2014), 104, 193110.

[60] G. Plechinger, J. Mann, E. Preciado, D. Barroso, A. Nguyen, J. Eroms, C. Schuller, L. Bartels and T. Korn. A direct comparison of CVD-grown and exfoliated MoS2 using optical spectroscopy. Semicond. Sci. Technol. (2014), 29, 064008.

[61] G. Kioseoglou, A. T. Hanbicki, M. Currie, A. L. Friedman and B. T. Jonker. Optical polarization and intervalley scattering in single layers of MoS2 and MoSe2. Scientific Reports (2016), 6, 25041.

[62] T. Cao, G. Wang, W. Han, H. Ye, C. Zhu, J. Shi, Q. Niu, P. Tan, E. Wang , B. Liu and J. Feng. Valley-selective circular dichroism of monolayer molybdenum disulphide. nature communications (2012), 3, 887.

[63] K. F. Mak, K. He, J. Shan and T. F. Heinz. Control of valley polarization in monolayer MoS2 by optical helicity. Nature Nanotechnology (2012), 7, 494-498.

[64] S. Wu, C. Huang, G. Aivazian, J. S. Ross, D. H Cobden, X. Xu. Vapor-Solid Growth of High Optical Quality MoS2 Monolayers with Near-Unity Valley Polarization. ACS Nano (2013), 7, 3, 2768-2772.

[65] Y. J. Chen, J. D. Cain, T. K. Stanev, V. P. Dravid and N. P. Stern. Valley-polarized exciton–polaritons in a monolayer Semiconductor. Nature Photonics (2017), 11, 431-436.

[66] H. Zeng, J. Dai, W. Yao, D. Xiao and X. Cui. Valley polarization in MoS2 monolayers by optical pumping. Nature Nanotechnology (2012), 7, 490-493.

[67] B. Zhua, H. Zengb, J. Daic, Z. Gonga, and X. Cui. Anomalously robust valley polarization and valley coherence in bilayer WS2. PNAS (2014), 111, 32, 11606–11611.

[68] X. Zhang, X. F. Qiao, W. Shi, J. B. Wu, D. S. Jiang and P. H. Tan. Phonon and Raman scattering of two-dimensional transition metal dichalcogenides from monolayer, multilayer to bulk material. Chem. Soc. Rev. (2015), 44, 2757

[69] J. Jeon, S. K. Jang, S. M. Jeon, Gwangwe Yoo, Yun Hee Jang, Jin-Hong Park and Sungjoo Lee. Layer-controlled CVD growth of large-area two-dimensional MoS2 films. Nanoscale (2015), 7, 1688

[70] M. Chhowalla, H. S. Shin, G. Eda, L. J. Li, K. P. Loh and H. Zhang. The chemistry of two-dimensional layered transition metal dichalcogenide nanosheets. Nature Chemistry (2013), 5, 263-275

[71] T. Cheiwchanchamnangij and W. R. L. Lambrecht. Quasiparticle band structure calculation of monolayer, bilayer, and bulk MoS2. Physical Review B (2012), 85, 205302

[72] A. Splendiani, L. Sun, Y. Zhang, T. Li, J. Kim, C. Y. Chim, G. Galli and F. Wang. Emerging Photoluminescence in Monolayer MoS2. Nano Lett. (2010), 10, 1271–1275

[73] C. Lee, H. Yan, L. E. Brus, T. F. Heinz, J. Hone and S. Ryu. Anomalous Lattice Vibrations of Single and Few-Layer MoS2. ACS Nano (2010), 4, 5, 2695-2700.

[74] H. G. Lee, S. Y. Oh and G. Fuller. A simple and accurate method to measure the threshold voltage of an enhancement-mode MOSFET. IEEE Transactions on Electron Devices (1982), 29, 2, 346-348.

[75] W. Bao, X. Cai, D. Kim, K. Sridhara, and M. S. Fuhrer. High mobility ambipolar MoS2 field-effect transistors: Substrate and dielectric effects. APPLIED Physics Letters (2013), 102, 042104.

[76] J. G. J. Chern, P. Chang, R. F. Motta and N. Godinho. A new method to determine MOSFET channel length. IEEE Electron Device Letters (1980), 1, 9, 170-173.

[77] J. Jeon, S. K. Jang, S. M. Jeon, G. Yoo, Y. H. Jang, J. H. Park and S. Lee. Layer-controlled CVD growth of large-area two-dimensional MoS2 films. Nanoscale (2015), 7, 1688

[78] N. P. Lopez, Z. Lin, N. R. Pradhan, A. I. Rabago, A. L. Elias, A. McCreary, J. Lou, P. M. Ajayan, H. Terrones, L. Balicas and M. Terrones. CVD-grown monolayered MoS2 as an effective photosensor operating at low-voltage. 2D Materials (2014), 1,011004

[79] A. M. V. Zande, P. Y. Huang, D. A. Chenet, T. C. Berkelbach, Y. You, G. H. Lee, T. F. Heinz, D. R. Reichman, D. A. Muller and J. C. Hone. Grains and grain boundaries in highly crystalline monolayer molybdenum disulphide. Nature Materials (2013), 12.

[80] L. Liu, H. Qiu, J. Wang, G. Xu and L. Jiao. Atomic MoS2 Monolayers Synthesized from Metal-Organic Complex by Chemical Vapor Deposition. Communication (2013), 00, 1-3.

[81] H. Kwon, S. Garg, J. H. Park, Y. Jeong, S. Yu, S. M. Kim, P. Kung and S. Im. Monolayer MoS2 field-effect transistors patterned by photolithography for active matrix pixels in organic light-emitting diodes. npj 2D Materials and Applications (2019), 9.

[82] D. Kaplan, Y. Gong, K. Mills, V. Swaminathan, P. M. Ajayan, S. Shirodkar and E. Kaxiras. Excitation intensity dependence of photoluminescence from monolayers of MoS2 and WS2/MoS2 heterostructures. 2D Mater. (2016), 3, 015005.

[83] V. K. Kumar, S. Dhar, T. H. Choudhury, S. A. Shivashankara and S. Raghavan. A predictive approach to CVD of crystalline layers of TMDs: the case of MoS2. Nanoscale, (2015), 7, 7802.

[84] S. Vangelista, E. Cinquanta, C. Martella, M. Alia, M. Longo, A. Lamperti, R. Mantovan, F. B. Basset, F. Pezzoli and A. Molle. Towards a uniform and large-scale deposition of MoS2 nanosheets via sulfurization of ultra-thin Mo-based solid films. Nanotechnology (2016), 27, 175703.

[85] Z. Chen, H. Liu, X. Chen, G. Chu, S. Chu and H. Zhang. Wafer-Size and Single-Crystal MoSe2 Atomically Thin Films Grown on GaN Substrate for Light Emission and Harvesting. ACS Appl. Mater. Interfaces (2016), 8, 20267−20273.

[86] D. Ruzmetov, K. Zhang, G. Stan, B. Kalanyan, G. R. Bhimanapati, S. M. Eichfeld, R. A. Burke, P. B. Shah, T. P. O'Regan, F. J. Crowne, A. Glen Birdwell, J. A. Robinson, A. V. Davydov and T. G. Ivanov. Vertical 2D/3D Semiconductor Heterostructures Based on Epitaxial Molybdenum Disulfide and Gallium Nitride. ACS Nano (2016), 10, 3580−3588.

[87] T. P. O'Regan, D. Ruzmetov, M. R. Neupane, R. A. Burke, A. A. Herzing, K. Zhang, A. G. Birdwell, D. E. Taylor, E. F. C. Byrd, S. D. Walck, A. V. Davydov, J. A. Robinson, and T. G. Ivanov. Structural and electrical analysis of epitaxial 2D/3D vertical heterojunctions of monolayer MoS2 on GaN. Applied Physics Letters (2017), 111, 051602.

[88] M. Moun, M. Kumar, M. Garg, R. Pathak and R. Singh. Understanding of MoS2/GaN Heterojunction Diode and its Photodetection Properties. Scientific Reports (2018), 8, 11799.

[89] Y. Li, Z. Qi, M. Liu , Y. Wanga, X. Cheng, G. Zhanga and L. Sheng. Photoluminescence of Monolayer MoS2 on LaAlO3 and SrTiO3 substrates. *Nanoscale*, (2014), 6, 15248-15254.

[90] Y. Lin, X. Ling, L. Yu, S. Huang, A. L. Hsu, Y. H. Lee, J. Kong, M. S. Dresselhaus and T. Palacios. Dielectric screening of excitons and trions in single-layer MoS2. Nano Lett. (2014), 14, 5569−5576.

[91] Y. Gong, B. Li, G. Ye, S. Yang, X. Zou, S. Lei, Z. Jin, E. Bianco, S. Vinod, B. I. Yakobson, J. Lou, R. Vajtai, W. Zhou and P. M Ajayan. Direct growth of MoS2 single crystals on polyimide substrates. 2D Mater. (2017), 4, 021028.

[92] Y. Yu, S. Y. Huang, Y. Li, S. N. Steinmann, W. Yang and L. Cao. Layer-Dependent Electrocatalysis of MoS2 for Hydrogen Evolution. Nano Lett. (2014), 14, 553−558.

[93] Q. Ji, Y. Zhang, T. Gao, Y. Zhang, D. Ma, M. Liu, Y. Chen, X. Qiao, P. H. Tan, M. Kan, J. Feng, Q. Sun and Z. Liu. Epitaxial Monolayer MoS2 on Mica with Novel Photoluminescence. Nano Lett. (2013), 13, 3870−3877.

[94] B. Radisavljevic, M. B. Whitwick, and A. Kis. Integrated Circuits and Logic Operations Based on Single-Layer MoS2. ACS Nano (2011), 5, 9934–9938.

[95] W. Zheng, Y. Qiu, W. Feng, J. Chen, H. Yang, S. Wu, D. Jia, Y. Zhou and P. Hu. Nanotechnology (2017), 28, 395601.

[96] X. Chen, Y. J. Park, M. Kang, S. K. Kang, J. Koo, S. M. Shinde, J. Shin, S. Jeon, G. Park, Y. Yan, M. R. Macewan, W. Z. Ray, K. M. Lee, J. A. Rogers and J. H. Ahn. Nat. Commun. (2018), 9, 1690.

[97] Z. F, Lu Z, Choi Y, Liu H, Zheng H, Xie L, Park K, Jiao L, Tao C 2018 ACS Appl. Nano Mater. 1 2041−2048

[98] V. Senthilkumar, L. C. Tam, Y. S. Kim, Y. Sim, M. J. Seong, J. I. jang. Direct vapor phase growth process and robust photoluminescence properties of large area MoS2 layers. Nano Res. (2014), 7, 1759.

[99] H. Liu, J. Gu and P. D. Ye. MoS2 Nanoribbon Transistors: Transition from Depletion Mode to Enhancement Mode by Channel-Width Trimming. IEEE Electron Device Letters (2012), 33, 9.

[100] J. Kwon, J. Y. Lee, Y. J. Yu, C. H. Lee, X. Cui, J. Honed and G. H. Lee. Thickness-dependent Schottky barrier height of MoS2 field-effect transistors. Nanoscale (2017), 9, 6151-6157.

[101] A. E. Yore, K. K. H. Smithe, S. Jha, K. Ray, E. Pop and A. K. M. Newaz. Large array fabrication of high performance monolayer MoS2 photodetectors. Applied Physics Letters (2017), 111, 043110.

[102] H. Y. Chang, M. N. Yogeesh, R. Ghosh , A. Rai, A. Sanne, S. Yang, N. Lu, S. K. Banerjee, and D. Akinwande. Large-Area Monolayer MoS2 for Flexible Low-Power RF Nanoelectronics in the GHz Regime. Adv. Mater. (2016), 28, 1818–1823.

[103] D. J. Late, Y. K. Huang, B. Liu, J. Acharya, S. N. Shirodkar, J. Luo, A. Yan, D. Charles, U. V. Waghmare, V. P. Dravid and C. N. R. Rao. Sensing Behavior of Atomically Thin-Layered MoS2 Transistors. ACS Nano (2013), 7, 6, 4879-4891.

[104] F. K. Perkins, A. L. Friedman, E. Cobas, P. M. Campbell, G. G. Jernigan and B. T. Jonker. Chemical Vapor Sensing with Monolayer MoS2. Nano Lett. (2013), 13, 668−673

[105] Y. Yang, N. Huo and J. Li. Sensitized monolayer MoS2 phototransistors with ultrahigh responsivity. J. Mater. Chem. C (2017), 5, 11614.

[106] C. Lan, C. Li, Y. Yin, H. Guo and S. Wang. Synthesis of single crystalline GeS nano ribbons for high sensitivity visible-light photodetectors. J. Mater. Chem. C (2015), 3, 8074.ACS Nano (2013), 7, 5, 3905-3911.

[107] D. S. Tsai, K. K. Liu, D. H. Lien, M. L. Tsai, C. F. Kang, C. A. Lin, L. J. Li and J. H. He. Few-Layer MoS2 with High Broadband Photogain and Fast Optical Switching for Use in Harsh Environments. ACS Nano (2013), 7, 5, 3905-3911.

[108] D. S. Tsai, K. K. Liu, D. H. Lien, M. L. Tsai, C. F. Kang, C. A Lin, L. J. Li and J. H. He. Few-Layer MoS2 with High Broadband Photogain and Fast Optical Switching for Use in Harsh Environments. ACS Nano (2013), 7, 5, 3905-3911.

[109] W. Zhang, M. H. Chiu, C. H. Chen, W. Chen, L. J. Li and A. T. S. Wee. Role of Metal Contacts in HighPerformance Phototransistors Based on WSe2 Monolayers. ACS Nano (2014), 8, 8, 8653-8661.

[110] F. Binet, J. Y. Duboz, E. Rosencher, F. Scholz, and V. Harle. Mechanisms of recombination in GaN photodetectors. Appl. Phys. Lett. (1996), 69, 1202.

[111] F. Guo, B. Yang, Y. Yuan, Z. Xiao, Q. Dong, Y. Bi and J. Huang. A nanocomposite ultraviolet photodetector based on interfacial trap-controlled charge injection. Nature Nanotechnology (2012), 7.

[112] O. L. Sanchez, D. Lembke, M. Kayci, A. Radenovic and A. Kis. Ultrasensitive photo-detectors based on monolayer MoS2. Nature Nanotechnology (2013), 8.

[113] F. K. Perkins, A. L. Friedman, E. Cobas, P. M. Campbell, G. G. Jernigan and B. T. Jonker. Chemical Vapor Sensing with Monolayer MoS2. Nano Lett. (2013), 13, 668−673.

[114] D. Sarkar, Wei Liu, X. Xie, A. C. Anselmo, S. Mitragotri and K. Banerjee. MoS2 Field-Effect Transistor for NextGeneration Label-Free Biosen. ACS Nano (2014), 8, 4, 3992–4003.

[115] H. Nam, B. R. Oh, P. Chen, M. Chen, S. Wi, W. Wan, K. Kurabayashi and X. Liang. Multiple MoS2 Transistors for Sensing Molecule Interaction Kinetics. Scientific Reports (2015), 5, 10546.

[116] D. J. Late, Y. K. Huang, B. Liu, J. Acharya, S. N. Shirodkar, J. Luo, A. Yan, D. Charles, U. V. Waghmare, V. P. Dravid and C. N. R. Rao. Sensing Behavior of Atomically Thin-Layered MoS2 Transistors. ACS Nano (2013), 7, 6, 4879–4891.

[117] D. J. Late, Y. K. Huang, B. Liu, J. Acharya, S. N. Shirodkar, J. Luo, A. Yan, D. Charles, U. V. Waghmare, V. P. Dravid and C. N. R. Rao. Sensing Behavior of Atomically Thin-Layered MoS2 Transistors. ACS Nano (2013), 7, 6,4879 – 4891.

[118] E. A. M. Klumperink, S. L. J. Gierkink, A. P. V. Wel, and B. Nauta. Reducing MOSFET 1/f Noise and Power Consumption by Switched Biasing. IEEE Journal of Solid-State Circuits (2000), 35, 7.

[119] Julius Cohen. Introduction to Noise in Solid State Devices (1982)

[120] Y. Imry. Introduction to Mesoscopic Physics, Oxford University Press, New York, 1997.

[121] R. Ochs, D. Secker, M. Elbing, M. Mayor and H. B. Weber. Fast temporal fluctuations in single-molecule junctions. Faraday Discuss (2006), 131, 281-289.

[122] E. Klumperink, A. vanderWel, J. Kolhatkar, E. Hoekstra, C. Salm, H. Wallinga, B. Nauta. Reduction of 1/f Noise by Switched Biasing: An Overview. In 16th Workshop on Circuits, Systems and Signal Processing, ProRISC (2005), pp. 307-315.

[123] Y. Yang, N. Huoa and J. Li. Sensitized monolayer MoS2 phototransistors with ultrahigh responsivity. J. Mater. Chem. C (2017), 5, 11614.

[124] W. Deng, Y. Chen, C. You, B. An, B. Liu, S. Li, Y. Zhang, H. Yan and L. Sun. Visible-infrared dual-mode MoS2-graphene-MoS2 phototransistor with high ratio of the Iph/Idark. 2D Mater. (2018), 5, 045027.

[125] Y. Chen, D. O. Dumcenco, Y. Zhu, X. Zhang, N. Mao, Q. Feng, M. Zhang, J. Zhang, P. H. Tan, Y. S. Huang and L. Xie. Composition-dependent Raman modes of $Mo_{1-x}W_xS_2$ monolayer alloys. Nanoscale (2014), 6, 2833.

[126] Q. Feng, Y. Zhu, J. Hong, M. Zhang, W. Duan, N. Mao, J. Wu, H. Xu, F. Dong, F. Lin, C. Jin, C. Wang, J. Zhang and L. Xie. Growth of Large-Area 2D $MoS_{2(1-x)}Se_{2x}$ Semiconductor Alloys. Adv.Mater. (2014), 26, 2648–2653.

[127] J. Xi, T. Zhao, D. Wang and Z. Shuai. Tunable Electronic Properties of Two-Dimensional Transition Metal Dichalcogenide Alloys: A First-Principles Prediction. J. Phys. Chem. Lett. (2014), 5, 285−291.

[128] J. G. Song, G. H. Ryu, S. J. Lee, S. Sim, C. W. Lee, T. Choi, H. Jung, Y. Kim, Z. Lee, J. M. Myoung, C. Dussarrat, C. L. Matras, J. Park, H. Choi and H. Kim. Controllable synthesis of molybdenum tungsten disulfide alloy for vertically composition-controlled multilayer. Nature Communications (2015), 6, 7817.

[129] Z. Lin, M. T. Thee, A. L. Elias, S. Feng, C. Zhou, K. Fujisawa, N. P. Lopez, V. Carozo, H. Terrones and M. Terrones. Facile synthesis of MoS2 and MoxW1-xS2 triangular monolayers. APL MATERIALS (2014), 2, 092514.

[130] D. Gerthsen, K. Tillmann and M. Lentzen. Structural Properties of lattice-mismatched Compound Semiconductor Heterostructures. In: Helbig R. (eds) Festkörperprobleme 34. Advances in Solid State Physics, vol 34. Springer, Berlin, Heidelberg.

[131] D. Liu, Sang J. Cho, J. H. Seo, K. Kim, M. Kim, J. Shi, X. Yin, W. Choi, C. Zhang, J. Kim, M. A. Baboli, J. Park, J. Bong, I. K. Lee, J. Gong, S. Mikael, J. H. Ryu, P. K. Mohseni, X. Li, S. Gong, X. Wang and Z. Ma. Lattice-mismatched semiconductor heterostructures. arXiv:1812.10225.

[132] T. Mano, K. Mitsuishi, N. Ha, A. Ohtake, A. Castellano, S. Sanguinetti, T. Noda, Y. Sakuma, T. Kuroda and K. Sakoda. Growth of Metamorphic InGaAs on GaAs (111)A: Counteracting Lattice Mismatch by Inserting a Thin InAs Interlayer. Cryst. Growth Des. 2016, 16, 5412−5417.

[133] S. Tongay, W. Fan, J. Kang, J. Park, U. Koldemir, J. Suh, D. S. Narang, K. Liu, J. Ji, J. Li, R. Sinclair and J. Wu. Tuning Interlayer Coupling in Large-Area Heterostructures with CVDGrown MoS2 and WS2 Monolayer. Nano Lett. 2014, 14, 3185−3190.

[134] P. K. Sahoo, S. Memaran, Y. Xin, L. Balicas and H. R. Gutiérrez. One-pot growth of two-dimensional lateral heterostructures via sequential edge-epitaxy. Nature (2018), 553, 63.

[135] K. Bogaert, S. Liu, J. Chesin, D. Titow, S. Gradecak and S. Garaj. Diffusion-Mediated Synthesis of MoS2/WS2 Lateral Heterostructures. Nano Lett. (2016), 16, 5129−5134.

[136] Y. Gong1, Junhao Lin, X. Wang, G. Shi, S. Lei, Z. Lin, X. Zou, G. Ye, R. Vajtai, B. I. Yakobson, H. Terrones, M. Terrones, B. K. Tay, J. Lou, S. T. Pantelides, Z. Liu, W. Zhou and Pulickel M. Ajayan. Vertical and in-plane heterostructures from WS2/MoS2 monolayers. Nature Materials (2014), 13.

[137] K. Chen , X. Wan , W. Xie , J. Wen , Z. Kang , X. Zeng, H. Chen and J. Xu. Lateral Built-In Potential of Monolayer MoS2 –WS2 In-Plane Heterostructures by a Shortcut Growth Strategy. Adv. Mater. 2015, 27, 6431–6437.

[138] Y. Yu, Shi Hu, L. Su, L. Huang, Y Liu, Z. Jin, A. A. Purezky, D. B. Geohegan, K. W. Kim, Y. Zhang and L. Cao. Equally Efficient Interlayer Exciton Relaxation and Improved Absorption in Epitaxial and Nonepitaxial MoS2/WS2 Heterostructures. Nano Lett. 2015, 15, 486−491.

[139] D. Kaplan, Y. Gong, K. Mills, V. Swaminathan, P. M. Ajayan, S. Shirodkar and E Kaxiras. Excitation intensity dependence of photoluminescence from monolayers of MoS2 and WS2/MoS2 heterostructures. 2D Mater. (2016), 3, 015005.

[140] J. Zhang, J. Wang, P. Chen , Y. Sun , S. Wu, Z. Jia, X. Lu, H. Yu, W. Chen, J. Zhu, G. Xie, R. Yang, D. Shi, X. Xu, J. Xiang, K. Liu and G. Zhang. Observation of Strong Interlayer Coupling in MoS2 /WS2 Heterostructures. Adv. Mater. (2016), 28, 1950–1956.

[141] J. Shi, R. Tong, X. Zhou, Y. Gong, Z. Zhang, Q. Ji, Y. Zhang, Q. Fang, L. Gu, X. Wang, Z. Liu and Y. Zhang. Temperature-Mediated Selective Growth of MoS2/WS2 and WS2/MoS2 Vertical Stacks on Au Foils for Direct Photocatalytic Applications. Adv. Mater. (2016), 28, 10664–10672.

[142] F. Wang, J. Wang, S. Guo, J. Zhang, Z. Hu and J. Chu. Tuning Coupling Behavior of Stacked Heterostructures Based on MoS2, WS2, and WSe2. Scientific Reports (2017), 7, 44712.

[143] H. Chen, X. Wen, J. Zhang, T. Wu, Y. Gong, X. Zhang, J. Yuan, C. Yi, J. Lou, P. M. Ajayan,W. Zhuang, G. Zhang, and J. Zheng. Ultrafast formation of interlayer hot excitons in atomically thin MoS2/WS2 heterostructures. Nature Communications (2016), 7, 12512.

[144] M. R. Molas, K. Nogajewski, M. Potemski and Adam Babiński. Raman scattering excitation spectroscopy of monolayer WS2. Scientific Reports (2017), 7, 5036.

[145] J. H Fan, P. Gao, A. M. Zhang, B. R. Zhu, H. L. Zeng, X. D. Cui, R. He and Q. M. Zhang. Resonance Raman scattering in bulk 2H-MX2 (M 5 Mo, W; X 5 S, Se) and monolayer MoS2. Journal of Applied Physics (2014), 115, 053527.

[146] A. A. Mitioglu, P. Plochocka, G. Deligeorgis, S. Anghel, L. Kulyuk and D. K. Maude. Second-order resonant Raman scattering in single-layer tungsten disulfide WS2. Physical Review B (2014), 89, 245442.

[147] W. Melitz, J. Shen, Andrew C. Kummel, S. Lee. Kelvin probe force microscopy and its application. Surface Science Reports (2011), 66, 1–27.

[148] A. Krayev, Connor S. Bailey, K. Jo, S. Wang, A. Singh, T. Darlington, G. Y. Liu, S. Gradecak, P. J. Schuck, E. Pop, and D. Jariwala. Dry Transfer of van der Waals Crystals to Noble Metal Surfaces to Enable Characterization of Buried Interfaces. ACS Appl. Mater. Interfaces (2019), 11, 38218−38225.

[149] K. Chen, X. Wan, J. Wen, W. Xie, Z. Kang, X. Zeng, H. Chen and J. B. Xu. Electronic Properties of MoS2/WS2 Heterostructures Synthesized with Two-Step Lateral Epitaxial Strategy. ACS Nano (2015), 9, 10, 9868–9876.

[150] P. Verma. Tip-Enhanced Raman Spectroscopy: Technique and Recent Advances. Chem. Rev. (2017), 117, 6447−6466.

[151] W. Zhao, Z. Ghorannevis, K. K. Amara, J. R. Pang, M. Toh, X. Zhang, C. Kloc, P. H. Tane and G. Eda. Lattice dynamics in mono- and few-layer sheets of WS2 and WSe2. Nanoscale (2013), 5, 9677.

[152] H. L. Liu, T. Yang, Y. Tatsumi, Y. Zhang, B. Dong, H. Guo, Z. Zhang, Y. Kumamoto, M. Y. Li, L. J. Li, R. Saito and S. Kawata. Deep-ultraviolet Raman scattering spectroscopy of monolayer WS2. Scientific Reports (2018), 8, 11398.

[153] J. T. Mlack1, P. M. Das, G. Danda, Y. C. Chou, C. H. Naylor, Z. Lin, N. P. López, T. Zhang, M.Terrones, A.T. C. Johnson and M. Drndić. Transfer of monolayer TMD WS2and Raman study of substrate effects. Scientific Reports (2017), 7, 43037.

[154] A. Berkdemir, H. R. Gutierrez, A. R. B. Mendez, N. P. -Lopez, A. L. Elıas, C. I. Chia, B. Wang, V. H. Crespi, F. L. Urıas, J. C. Charlier, H. Terrones and M. Terrones. Identification of individual and few layers of WS2 using Raman Spectroscopy. Scientific Reports (2013), 3, 1755.

[155] A. McCreary, A. Berkdemir, J. Wang, M. A. Nguyen, A. L. Elías, N. P. López, K. Fujisawa, B. Kabius, V. Carozo, D. A. Cullen, T. E. Mallouk, J. Zhu and M. Terrones. Distinct photoluminescence and Raman spectroscopy signatures for identifying highly crystalline WS2 monolayers produced by different growth methods. J. Mater. Res. (2016), 31, 7.

[156] W. Shi, M. L. Lin, Q. H. Tan, X. F. Qiao, J. Zhang and P. H. Tan. Raman and photoluminescence spectra of two-dimensional nanocrystallites of monolayer WS2 and WSe2. 2D Mater. (2016), 3, 025016.

[157] M. R. Molas, K. Nogajewski, M. Potemski and A. Babińsk. Raman scattering excitation spectroscopy of monolayer WS2. Scientific Reports (2017), 7, 5036.

[158] A. M. Sanchez and L. Wirtz. Phonons in single-layer and few-layer MoS2 andWS2. Physical Review B (2011), 84, 155413.

[159] M. H. Chiu, M. Y. Li, W. Zhang, W.T. Hsu, W. H. Chang, M. Terrones, H. Terrones, L.J. Li. Spectroscopic Signatures for Interlayer Coupling in MoS2-WSe2 Van Der Waals Stacking. ACS Nano (2014), 8, 9649−9656.

[160] X. Hong, J. Kim, S. F. Shi, Y. Zhang, C. Jin, Y. Sun, S. Tongay, J. Wu, Y. Zhang, F. Wang. Ultrafast Charge Transfer in Atomically Thin MoS2/WS2 Heterostructures. Nat. Nanotechnol. (2014), 9, 682− 686.

[161] F. Ceballos, M. Z. Bellus, H. Y. Chiu, H. Zhao. Ultrafast Charge Separation and Indirect Exciton Formation in a MoS2-MoSe2 Van Der Waals Heterostructure. ACS Nano (2014), 8, 12717−12724.

[162] H. U. Hassan, J. Mun, B. S. Kang, J. Y. Song, T. Kima and S. W. Kang. Sensor based on chemical vapour deposition grown molybdenum disulphide for gas sensing application. RSC Adv. (2016), 6, 75839.